CONTROLLED FACET GROWTH OF GaN AND THE OVERGROWTH WITH ZnO

ZHOU HAILONG

National University of Singapore

2007

CONTROLLED FACET GROWTH OF GaN AND THE OVERGROWTH WITH ZnO

ZHOU HAILONG

(B.Sc., M.Eng., Shandong Univ.)

A THESIS SUBMITTED

FOR THE DEGREE OF DOCTOR OF PHILOSOPHY

DEPARTMENT OF PHYSICS

NATIONAL UNIVERSITY OF SINGAPORE

2007

To my wife, Jiang Yi

Acknowledgements

I am grateful to my advisor **Prof. Chua Soo Jin** for providing me the opportunity to have an adventure into the world of the compound semiconductor science and technology. He not only taught me nearly everything about the nitride based materials growth, characterization and processing but also shared with me his wisdom, insight and humor throughout these years. It has been a great life experience to study under his guidance. I am greatly amazed by the breath and depth of his knowledge. Given by his flexible educating method, I feel the freedom to concentrate on scientific truth rather than relecant regulations.

I would like to thank my advisor **Prof. Osipowicz Thomas** for his guidance, advice and kindness through my thesis work. He has taught me nearly all the hands-on experimental skills I have on RBS and always encouraged me to think independently. His enthusiasm to science and consistency to work will keep inspiring me in my future career.

I would also like to show my appreciation to **Dr. Liu Wei** teaching me the knowhow in MOCVD growth and for the valuable discussions. His passion for the profession has always an inspiration for me.

Special thanks to **Prof. Feng Yuan Ping, Prof. Lin Jian Yi**, **Prof. SOW Chorng Haur**, **Dr. Wang Lian Shan, Dr. Chen Peng, Dr. Sudhiranjan Tripathy, Dr. Wang Ya Dong, Dr. Zang Ke Yang, Dr. Pan Hui** and **Dr. Zhu Yan Wu**, who are great partners to work with. I have enjoyed all the helpful discussions with them. They make my Ph.D career a happy memory.

I happily acknowledge my interactions with **Prof. David J. Srolovitz** and **Dr. Danxu Du,** their impressive V-plot and Level-Set simulation methods for the

epitaxial lateral overgrown GaN growth, which predict the way to control the crystalline shapes of the lateral overgrown GaN.

Special thanks to the group members in Prof. Chua's group, **Dr. Teng Jing Hua, Dr. Zhang Xin Hai, Dr. Dong Jian Rong**, **Yong Anna Marie** and **Teo Siew Lang,** also the staffs and students in CIBA lab of Physics Department, **Dr. Jeroen van Kan, Dr. Shao Peige, Dr. Piravi Perumal Malar, Mr Choo Theam Fook, Mr Chan Taw Kuei** and **Mr Ho Chee Sheng (Brandon),** for their valuable discussions and experiment support.

Special thanks to **Prof. Xu Ke** and **Prof. Zhang Guo Yi** from Beijing University for the help on the low temperature cathodoluminescence measurement.

Many thanks to my parents for their unselfish love, support and many sacrifices throughout my life made my education possible.

Finally, I would not be able to finish this work without the love and support from my wife **Jiang Yi**. She endured with me through this period, listened to my moaning and complaints and supported me every step of the way. This work is meaningful to me especially because of her. It witnesses our life at NUS. To my son-the best gift from God, the brightness light in the darkest night, **Yi Nan**.

Table of Contents

Abstract

The III-nitrides semiconductors form an interesting class of wide bandgap materials, which are likely to be the basis of a strong development of a novel family of semiconductor devices, for optoelectronics as well as for electronics. For example, the entire spectral region from UV to red can be covered with III-Nitride optical devices, which is not possible with the established III-Arsenides and phosphides materials systems and related alloys. Also, III-Nitrides transistors are expected to be superior to the corresponding ones made from Si and other III-V materials in terms of frequency range, power handling and the temperature region of operation. However, a large dislocation density exists in nitride materials for lack of appropriate substrates. Thus the so-called Facet Control Epitaxial Lateral Overgrowth (FACELO) technology was developed and was able to successfully reduce the dislocation density of nitride materials. Even more, by tuning the growth conditions, FACELO GaN could achieve different facets, e.g. $(1\bar{1}01)$ and $(11\bar{2}2)$, this provides good semi-polar plane template for which quantum well or superlattice structures can grown with a reduced piezoelectric field.

In this study, three activities were carried out on the ELO GaN templates: Firstly, a Level-Set method based on V-plot model tailored for epitaxial lateral overgrowth (ELO) is developed with my collaborators. The application of the V-plot and Level-Set simulation methods to GaN grown by ELO is able to capture all of the major features of growth morphologies observed in a diverse set of experiments. In particular, the simulation results provide an understanding about the stability of fast growing surfaces against perturbations during ELO growth and way to unveil the intrinsic imperfect nature of merging of the epitaxial layers growth front.

Based on the simulation result, a simple residual mismatch strain model is proposed to explain that smaller aspect ratio (window width to island height) which is preferred to produce lower angle grain boundaries on merging and higher quality crystals.

Secondly, we investigated the InGaN/GaN multi-quantum wells (MQWs) and AlGaN/GaN MQWs grown on the FACELO GaN templates. With structural and optical characterization, micro-Raman scattering spectroscopy revealed a significant relaxation of compressive stress in the laterally overgrown GaN. From the low temperature cathodoluminescence (CL) spectra, the FACELO InGaN/GaN MQWs grown on (11$\bar{2}$2) plane emit with a broad spectral width and the optical quality of MQWs on (11$\bar{2}$2) facet is significantly improved compare to that on the (0001) plane. A blue shift was observed with AlGaN/GaN quantum wells grown on the (11$\bar{2}$2) facet compared to the (0001) facet. And the CL intesity of MQWs on the (11$\bar{2}$2) facet is several times larger than that on the (0001) plane. These findings strongly suggest that achievement of stronger oscillator strength can be achieved by suppressing the polar field by growing the quantum wells on a non-polar or semi-polar plane.

Finally, high quality ZnO grown on FACELO GaN/sapphire templates was achieved by the thermal evaporation method. The ZnO/FACELO GaN heterostructures showed a substantial improvement in the crystalline quality with a lower defect density and excellent photoluminescence emission. Different morphological ZnO can be controlled by the variation of growth conditions, such as the temperature and oxygen flow rate. In addition, the lattice matching between the ZnO and GaN, thermal and optical properties, and the perfect interfaces of these ELO ZnO/GaN heterostructures will provide new opportunities for the

fabrication of hybrid ZnO/GaN optoelectronic devices on sapphire.

List of Tables

List of Figures

Publications

1. Al incorporation in AlGaN on (11$\bar{2}$2) and c-plane surface orientation

   Hailong Zhou, Soo Jin Chua and Chen Peng
   Journal of Crystal Growth, 292, pp.5-9 (2006)

2. Improvement of microstructural and optical properties of GaN layer on sapphire by nanoscale lateral epitaxial overgrowth

   Y. D. Wang, K. Y. Zang, and S. J. Chua, S. Tripathy, H. L. Zhou and C. G. Fonstad
   Appl. Phys. Lett., 88, p.211908 (2006)

3. AlGaN/GaN multiple quantum wells grown on facet-controlled epitaxial lateral overgrown GaN/sapphire templates

   H. L. Zhou, S. J. Chua, S. Tripathy, N. L. Yakovlev, L. S. Wang, W. Liu
   Journal of Physics: Condensed Matter, 19, p.056005 (2007)

4. InGaN multiple quantum wells grown on ELO GaN templates and the optical properties characterization

   Hailong Zhou, S. J. Chua, Keyan.Zang, L. S. Wang, S. Tripathy, N. Yakovlev, Osipowicz Thomas
   Journal of Crystal Growth, 298, pp.511–514 (2007)

5. Structural properties of ZnO grown on GaN/sapphire templates: the transition from nanorods to thin films

   H. L. Zhou, S. J. Chua, H. Pan, J. Y. Lin, Y. P. Feng, L. S. Wang, W. Liu, K. Y. Zang, and S. Tripathy
   Electrochemical and Solid-State Letters, **10** (3), H98-H100 (2007)

6. Morphology Controllable ZnO growth on facet-controlled epitaxial lateral overgrown GaN/sapphire templates

   Hailong Zhou, S. J. Chua, H. Pan, Y. W. Zhu, O. Thomas, W. Liu, K.Y. Zang, Y. P. Feng and C. H. Sow
   Journal of Physical Chemistry C 111(17), 6405-6410, (2007)

7. Normal incidence intersubband absorption in GaN/AlN superlattices grown on facet-controlled epitaxial lateral overgrown GaN/sapphire templates

   H. L. Zhou, W. Liu, S. J. Chua

   Japanese Journal of Applied Physics (Brief Communication) **46,** (8A), 5128, (2007)

8. Channeling contrast microscopy of epitaxial lateral overgrowth of ZnO/GaN films

   Hailong Zhou, Hui Pan, Taw Kuei Chan, Chee Sheng Ho, Yanping Feng, Soo-Jin Chua, Osipowicz Thomas

Nucl. Instrum. Meth. Phys. Res. B 260 299–303 (2007)

9. Anneal-induced structural changes of GaIn(N)As/Ga(N)As multiple quantum wells grown by molecular beam epitaxy

   H. F. Liu, N. Xiang, H. L. Zhou, S. J. Chua and S. Y. Chow
   Journal of Crystal Growth 301-302, 548-551, (2007)

10. The Merging Behavior of GaN Islands Grown by Selective Area Growth

    Du, D. X., Srolovitz, D. J., Zhou, H.L & Chua, S. J.

    Appl. Phys. Lett. (Submitted).

11. Growth Front Instability of GaN by Selective Area Growth.

    Du, D. X., Srolovitz, D. J., Zhou, H. L& Chua, S. J.

    Appl. Phys. Lett. (Submitted).

Patent

1. Method of Zinc Oxide Film Growth on Epitaxial Lateral Overgrown Gallium Nitride Templates

   SooJin Chua, Hailong Zhou, Jianyi Lin, Hui Pan

   US 60.794.775 filed on 25th/04/2006

Chapter 1

Introduction

Gallium nitride is a very attractive III-V semiconductor material, having a band gap ideal for emitting blue/UV light [1-3]. The binary (GaN, AlN, InN), ternary (AlGaN, InGaN, InAlN) and quaternary (AlGaInN) nitride materials have been pursued for many years, in the attempt to realize optical emission over the entire visible spectrum using band-gap engineering [4]. In addition, GaN and other III-nitrides have a myriad of possible applications, including full color displays, laser for reading or storing data on high density optical media, signal/automotive lighting, detector and high temperature/high power electronics. [5-6]

GaN is currently grown in the form of epitaxial layers mainly by metal organic chemical vapor deposition (MOCVD), hydride vapor phase epitaxy (HVPE) and molecular beam epitaxy (MBE). Single crystal sapphire (Al_2O_3) wafers are widely used as substrates. Although SiC is a promising substrate material with its 3.5% misfit with GaN, this wafer is still too expensive. Potentially more appropriate substrates like $LiAlO_2$, $MgAl_2O4$, $ScMgAlO_4$, and ZnO have been tested in several laboratories. Even though good quality GaN epilayers were obtained (although not significantly better than GaN/Sapphire), the use of such materials does not solve the problem of the lack of GaN substrates. Therefore, for the time being, GaN layers have to be grown by heteroepitaxy.

Because of the lattice and thermal mismatch between the substrate and GaN, the epitaxial layer generates a large density of dislocations (10^9 to 10^{11} cm^{-2}).

With such a high density of dislocations, it was difficult to believe that high performance optoelectronic devices could be realized. The real breakthrough in the laser technology has been demonstrated by dramatic improvement of the laser lifetime reaching up to 10,000 hours at the end of 1997 by using the epitaxial lateral overgrowth techonolgy (ELO) [7]. This has been made possible with the implementation of the ELO technology, which significantly reduces the dislocations density. Improved device performances were also obtained with the ELO technology in other devices, such as LEDs and UV photodetectors. Soon after, a technique, so called facet-controlled epitaxial lateral overgrowth (FACELO), was developed by starting the epitaxial growth on (0001) plane and tuning the growth conditions to develop other facets, e.g. ($1\bar{1}$ 01), ($11\bar{2}2$) and ($11\bar{2}$ 0), on GaN stripes [2, 3].

When the GaN growth surface is the (0001) plane, planar strain induced by the different lattice constants of the quantum wells (such as InGaN or GaN) and the barrier layers (such as GaN or AlGaN) gives rise to strong internal piezoelectric fields and a spontaneous polarization field. [8] This leads to a local separation of electrons and holes in these quantum wells resulting in a poor overlap of electron and hole wave functions, long radiative lifetimes, [9] low internal quantum efficiencies [10] and recombination through competing non-radiative channels in the devices. Reduction of electrostatic fields is possible by growing the structures on a non-polar plane of sapphire, e.g. on r-plane [11], where GaN grows in the ($10\bar{1}2$) or ($11\bar{2}0$) plane. Other approaches make use of more exotic substrates such as $LiAlO_2$ [12], on which pure m-plane GaN ($1\bar{1}00$) growth was achieved. Even with such a kind of non-polar substrate realized the zero electric field in the quantum well, the as-grown device did not achieve higher

performance than that grown on the traditional c-plane sapphire substrate due to the lower crystal quality on such a non-polar plane.

The FACELO technique can help to overcome both problems, which is the new development of the ELO technology. The FACELO GaN template is realized by starting the epitaxial growth on the (0001) sapphire substrate and tuning the growth conditions to develop other facets, e.g. $(1\bar{1}01)$ and $(11\bar{2}2)$, on the ELO stripes [13-14].

In this Introduction Chapter, a brief review is given by introducing the two main issues to the performance of the nitride materials device, followed by a discussion of the ELO and FACELO techniques. As some theoretical approaches to describe morphological variations in the ELO process were simulated by the Level-Set method [15-17], some important aspects of this method will be introduced.

1.1 Dislocations and polar induced electric field in nitride materials

1.1.1 Dislcations in nitride materials

The lattice parameters and the thermal expansion coefficients of sapphire (10^{-6} K^{-1}) and SiC (5 x10^{-6} K^{-1}) are not well matched to GaN (3.17x10^{-6} K^{-1}). The epitaxial growth therefore generates a large density of dislocations (10^9 to 10^{11} cm^{-2}). The growth begins with the deposition of a low temperature nucleation layer. This nucleation layer is polycrystalline with small columnar micrograins [18, 19]. A reduction of the number of dislocations is observed during the first stages of the epilayer growth at high temperature until a smooth film is obtained. A clear distinction should be made between the growth process with a continuous nucleation layer [20], and the growth process with a nucleation layer formed by

isolated quasi-monocrystalline islands [21, 22]. In the first case, the early stage of the epilayer growth corresponds to an increase of the grain size by the lateral development of some grains. In this situation, defect reduction phenomena occur by the formation of dislocation half-loops [20]. In the second alternative, this early stage corresponds to the lateral expansion of many localized islands to form a film via coalescence. Whatever the mechanisms involved in the initiation of the growth, the resulting growth front is a smooth (0001) surface. The dislocations are then vertically threading. They only encounter free (0001) surfaces and no further reduction of the number of dislocations is observed.

Three types dislocations can occur in wurtzite GaN layers: (i) **b**= [0001] (screw ***c*** -type dislocation), (ii) **b**=1/3 [11$\bar{2}$0] (edge ***a*** -type dislocation), and (iii) **b** =1/3[11$\bar{2}$3] (mixed ***a*** + ***c*** -type dislocation) [23]. The dislocations present in a layer depend on the substrate and on the growth conditions. In high quality GaN, stacking disorder and partial dislocations are located at the interface and originate from the low-temperature nucleation layer. With such a high density of dislocations, it was difficult to believe that high–performance optoelectronic devices could be realized from this type of materials.

Recently, more direct evidence indicates that threading dislocations can be opitcally and electrically active. In particular, atomic force microscopy (AFM) combined with cathodoluminescence (CL) [24] as well as transmission electron microscopy (TEM) combined with [25] CL clearly show threading dislocations to be precisely related to dark spots in the band-edge emission CL images. This effect could be explained as resulting from the deficiency of minority carriers at threading dislocations (TDs). TDs also reduce the photoluminescence intensity. Hino et al.'s work displays the PL intensity as a function of the TDs densities with

a screw component [26]. The work done by Marchand also give pertinent details about the TDs distribution, it also indicates that TDs are directly linked to a given nonradiative center. [27]

1.1.2 Polar field in nitride materials

Noncentrosymmetric compound crystals exhibit two different sequences of the atomic layering in the two opposing directions parallel to certain crystallographic axes, and consequently crystallographic polarity along these axes can be observed. For binary A–B compounds with wurtzite structure, the sequence of the atomic layers of the constituents A and B is reversed along the [0001] and [000$\bar{1}$] directions. The corresponding (0001) and (000$\bar{1}$) faces are the A-face and B-face, respectively. In the case of heteroepitaxial growth of thin films of a noncentrosymmetric compound, the polarity of the material cannot be predicted in a straightforward way, and must be determined by experiments. This is the case for GaN epitaxial layers and GaN-based heterostructures with the most common growth direction normal to the (0001) basal plane, where the atoms are arranged in bilayers. These bilayers consist of two closely spaced hexagonal layers, one formed by cations and the other formed by anions, leading to polar faces. Thus, in the case of GaN, a basal

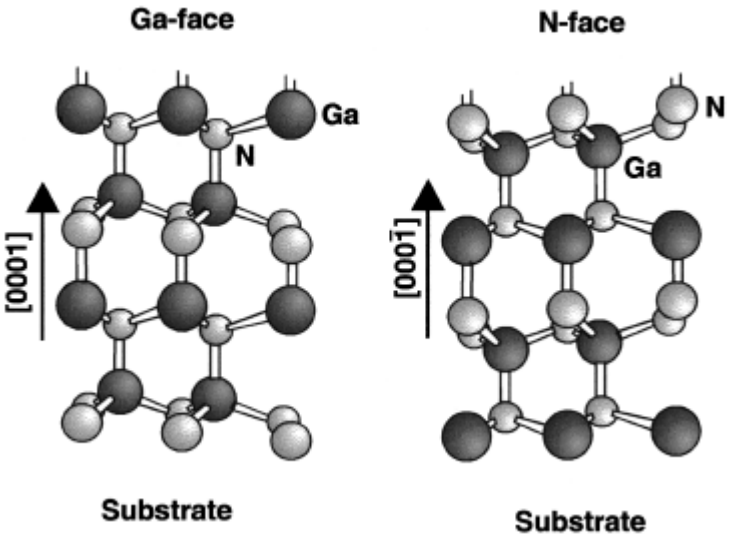

Fig. 1.1. Schematic drawing of the crystal structure of wurtzite Ga-face and N-face GaN.

surface should be either Ga- or N-faced. By Ga-faced we mean Ga atoms on the top position of the {0001} bilayer, corresponding to the [0001] polarity (Fig. 1.1). It is, however, important to note that the (0001) and (000$\bar{1}$) surfaces of GaN are nonequivalent and differ in their chemical and physical properties. [28]

Recently, a series of first principle calculations [29-31] has reopened this issue for the technologically relevant III-nitride semiconductors, whose natural crystal structure is wurtzite. It was shown that the nitrides have a very large spontaneous polarization, as well as large piezoelectric coupling constants. [29] The strong influence of polar fields on optical properties of AlGaN/GaN QWs has been demonstrated in several recent works [32-36]. There is a drastic reduction of the PL peak energy with increase in QW width due to the action of the polar fields. For a 10 nm QW sample, the exciton peak is at about 3.3 eV, i.e. well below the bulk GaN bandgap. This is usually referred to as the Quantum Confined Stark Effect (QCSE). The strongly tilted potential in the QW also drastically reduces the overlap between the electron and hole wave functions, so that the oscillator strength for the excitonic recombination process gets considerably reduced [32]. The corresponding increase in decay time up to 10 nm well width is several orders of magnitude.

The position of the confined levels for electrons and holes in the AlGaN/GaN QW can easily be calculated for a square well potential, as a function of the aluminum mole fraction *x*, assuming reasonable values for the band offsets. The realistic case of a triangular potential introduces a profound difference in the position of the confined levels, however, in particular for electrons in narrow QWs. The bandgap of the quantum wells will be smaller with a strong polarization field.

So the influence of the QCSE is the first order to the recombination process in these QWs, and must not be neglected.

1.2 ELO and FACELO technologies

The ELO technology can be described as follows: first, a few micrometer thick GaN layer is grown on sapphire or 6H-SiC. Next a dielectric (SiO_2 or SiN) mask is deposited using well established technologies such as CVD or PECVD. Using standard photolithographic techniques, a set of parallel stripes separated by window areas is opened in the mask. During the initial regrowth, either in MOCVD [37] or HVPE [38] or even sublimation growth [39, 40], selective area epitaxy

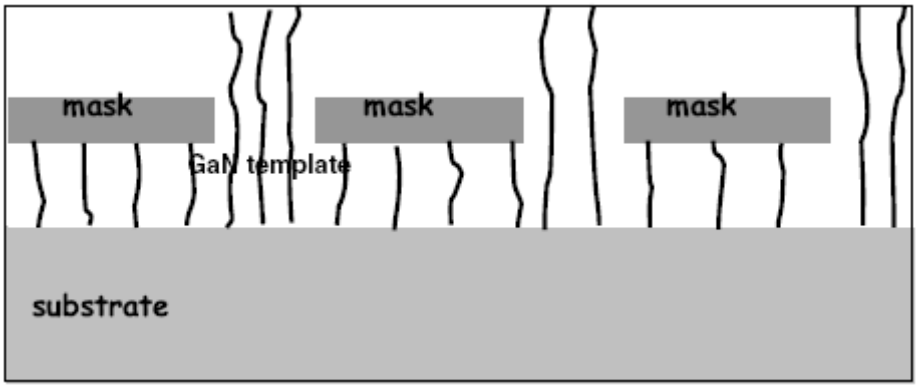

Fig. 1.2 Schematic representation of ELO, black lines represent dislocations

is achieved, which means that the regrowth is initiated in the windows without any nucleation on the dielectric mask. Under proper conditions, once the GaN growing film reaches the top of the stripes, epitaxial lateral growth over the mask starts and finally leads to a full coalescence and to a smooth surface suitable for device fabrication. The basic idea (Fig. 1.2) is that this technique may lead to a filtering of the defects: above the windows, the microstructure of the underlying GaN template is reproduced whereas the laterally grown material (over the mask) is

defect-free. The masked areas stop the propagation of threading dislocations, which arise from the template since lateral growth proceeds from dislocations free vertical facets.

ELO GaN results in material with dislocation density in the range of 10^6 cm^{-2}, and made possible for the fabrication of laser diodes. In a systematic study, Hiramatsu et al. [13] investigated the morphology of ELO GaN starting from either [1$\bar{1}$00] or [11$\bar{2}$0] stripes as a function of the growth pressure (p) or temperature (T), as shown in Fig.1.3. The variation of the morphology is related to the stability of

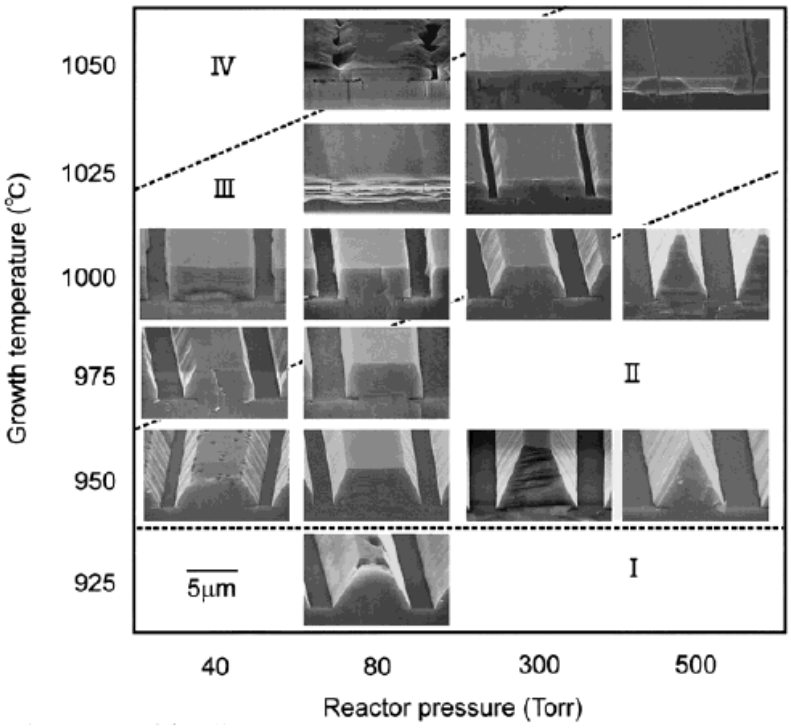

Fig. 1.3 SEM photographs of lateral overgrowth of GaN from <1$\bar{1}$00> stripes at different temperatures or pressures. (From Hiramatsu et al. [23])

each surface, which depends mainly on the "surface energy" and "stability of surface atoms". In order to consider these factors, the density of dangling bonds per unit area (DB) and the surface polarity could be evaluated, for simplicity. Figure 1.4 shows the morphological change from regions II to IV (as shown in Fig.

1.3) and the corresponding atomic configuration with DB and the surface polarity for each facet [52]. The change of the morphology with decreasing P is similar to that with increasing T in the regions II–IV. In region II, at high P or low T, the (0001) surface becomes narrow and the $\{11\bar{2}2\}$ surfaces of the sides become broad. In region III at lower P or higher T, $\{11\bar{2}0\}$ surfaces appear instead of $\{11\bar{2}2\}$ ones in the side walls. The morphological change from $\{11\bar{2}2\}$ to $\{11\bar{2}0\}$ should be considered in terms of the stability of each surface which depends mainly on the "surface energy" and "stability of surface atoms". The $\{11\bar{2}2\}$ facet has two possible polarities: N polarity or Ga polarity, on the surface. The surface with N polarity tends to appear because surface nitrogen atoms are stabilized under growth conditions with high V/III source gas ratios like in MOCVD, especially at high P or low T. Therefore, the atomic configuration of the $\{11\bar{2}2\}$ surface with N polarity is dominant, as shown in figure 1.4. Thus, it is suggested that with increasing T or decreasing P in region II, the growth rate of the $\{11\bar{2}2\}$ surface becomes slow, resulting in narrowing of the $\{11\,\bar{2}\,2\}$ surface and broadening of the (0001) surface. For $[11\bar{2}0]$ stripes, whatever the temperature (<925ºC) and the pressure, triangular stripes with $(1\,\bar{1}\,01)$ facets are formed. Conversely, for $[1\bar{1}\,00]$ stripes, the final shape depends significantly on the growth conditions. The facet morphology varies with growth parameter and hence the so called facet control lateral overgrowth (FACELO). Based on the FACELO methods, the 2 steps ELO and even 3 steps ELO was used to achieve dislocation densities down to about the 10^4 cm^{-2}. At the same time, many different methods were investigated, such as the pendeo-epitaxy, air-bridged lateral growth and patterned substrates. All these methods intended to realize a lower dislocation density with an easy fabrication process. Recently, the HVPE growth method has

emerged as a subject of considerable interest due to its ability to produce very thick high quality GaN film on sapphire substrate. Together with a technique for substrate removal it becomes a promising alternative for producing thick free-standing GaN films to be used as substrates.

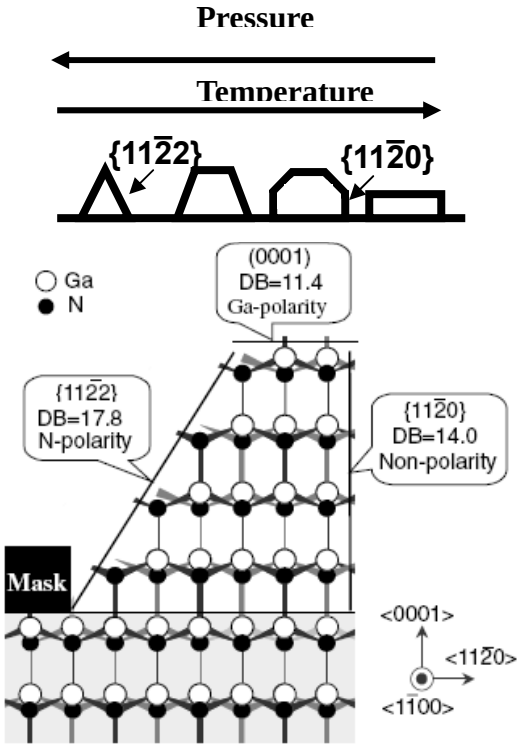

Fig. 1.4 A model of the morphological change in ELO GaN along the [1$\bar{1}$00] stripe for different reactor pressures and growth temperatures, and the corresponding atomic configuration. Here, "DB" stands for the density of dangling bonds [52].

The lateral overgrowth rates and the equilibrium facets developed in the process depend on both the crystallographic orientation of the stripe openings and the growth parameters, temperature, V/III ratio in the vapour phase, pressure, composition of the carrier gas (H_2, N_2), fill factor (ratio of the stripe opening to the pattern period) [41-45]. Growth anistotropy corresponds to the occurrence of different growth rates on different crystallographic planes. As the observation in Fig. 1.3, there are significantly difference between the [1$\bar{1}$00] and [11$\bar{2}$0] direction.These features are strongly supported by the analysis of the orientational dependence of the growth rate associated with surface kinetics. In MOCVD, growth anisotropy occurs because the diffuseing molecular species are preferentially incorporated into different crystallographic sites. The crystallographic relationships of three facet planes are illustrated in Fig. 1.4. It has been demonstrated that the lateral growth is easier

when the stripes are aligned along [1$\bar{1}$00] GaN direction [46]. With stripes aligned along the [1$\bar{1}$00] direction, the morphology gradually changes as the growth temperature increases, from triangular stripes to rectangular cross section with (0001) top facet and (11$\bar{2}$2) sidewalls [43]. Conversely, for stripes along the [11$\bar{2}$0] direction, the lateral overgrowth is limited by slow growing rate {1$\bar{1}$01} facets, which are the most stable faces in GaN. The lateral growth rate for the [1$\bar{1}$00] stripe is much faster than that for the [11$\bar{2}$0] stripe [39, 41].

Hiramatsu *et al*. [13] investigated the morphology of ELO GaN starting from either [1$\bar{1}$00] or [11$\bar{2}$0] stripes as a function of the growth pressure (p) or temperature (T). For [11$\bar{2}$0] stripes, whatever the temperature (<925ºC) and the pressure, triangular stripes with (1$\bar{1}$01) facets are formed. Conversely, for [1$\bar{1}$01] stripes, the final shape depends significantly on the growth conditions.

1.3 The Level-Set method: the continuum simulation of the ELO GaN growth

Crystal morphology determines many material properties and applicability of a material for particular technological applications. For example, control of the size and shape of islands on substrate can be used to manipulate electronic band gaps. The presence of rough, faceted surfaces limits the applicability of materials in multi-layer film applications. While it is possible for surface features to be controlled by brute force (e.g., through lithography), it is also possible to use the thermodynamic properties of materials to self-assemble desired surface features. Modeling and simulation are particularly important for giving insight into and developing the understanding necessary to manipulate the latter class of morphology evolution. It is possible to develop a systematic approach to determine the dominant crystal growth process and also to determine growth

velocities. To use the result to simulate crystal growth, it is necessary to choose a numerical scheme that can easily handle complicated morphologies as mentioned previously. Although several candidate methods exist, the level-set method was chosen due to the ease to describe the sharp interface evolution.

The simulation procedure must satisfy several requirements. First, it should be able to describe morphology evolution, given only the V-plot. Second, the method should be able to naturally handle flat facets and corners, which correspond to singularities, and curved surfaces. Finally, the method should be able to easily account for topology change, such as crystallite impingement and facet/corner/edge nucleation or annihilation. Many different methods have been employed to implement a V-plot model (where the surface normal (growth) velocity depends only upon the local surface orientation) in film growth contexts. These include front tracking methods [47], level-set methods [48, 49], vertex models [50], etc.

Front tracking methods, in which the surface velocity is a continuous function of the surface normal, have difficulties in handling sharp corners and tracking complicated geometries. A special class of front tracking methods, the so-called crystalline method, avoids such difficulties by evolving line segments (2D) or planes (3D). It has the further advantage that it only requires knowledge of the velocity of the surface corresponding to facets. However, such methods cannot readily account for the formation of new facets or describe situations in which there are a combination of flat facets and curved surfaces.

In the vertex method, [50] the three-dimensional crystal surface is projected onto a two-dimensional plane. The numerical method tracks the projected surface in two dimensions, as a two-dimensional version of the crystalline method.

Therefore, it suffers from the same difficulties as the crystalline method mentioned above.

Level-set methods [51] are based upon an implicit description of evolving surfaces and, hence, can easily account for arbitrary topological changes and be applied in any number of dimensions. Peng, et al. [48] described a useful implementation of this approach for crystals with faceted surfaces. Russo and Smereka [49] went a step further by proposing a level-set method which reduces the required velocity information to the velocities of facets only. This approach was shown to lead to flat facets with sharp corners and could describe polycrystalline growth [49]. However, the growth velocity used during the level-set simulation has two critical issues. This method suffers from the fact that it only has very incomplete information on V-plot. In this case, the interpolated V-plot is not continuous, thus leading to numerical difficulties. This approach can not account for cases where features are not in the facet orientations, such as growth from a circular annulus pattern.

Due to the elegant geometric features of the level-set method, we will use this method in our investigation of ELO growth of GaN, which will be discussed in Chapter 3. Furthermore, we were able to derive a V-plot in Chapter 3 for ELO growth of GaN that should be able to capture all of the major growth features. Therefore, there is no essential difficulty in applying level set methods to ELO growth. However, due to the peculiar feature of ELO growth, the level set method has to be tailored to meet our needs. In the following, we describe the level-set method and develop special algorithms to determine the initial level-set based on the geometric features of mask patterns used in ELO.

In the level-set method, the evolution of the surface is described through

the evolution of a function φ(x, t) (where x represents a position in three dimensional spaces). The surface of interest is the contour for which φ(x, t) is zero. This is the zero-level of the level-set function. This is an implicit description of the surface. The level set function is a very convenient tool to study interfaces. It was also applied to determine the position of shrinking cylindrical grain boundaries.

Since the surface is always defined as the same contour (level) of φ(x, t), it follows (by the chain rule) that the level-set function φ(x, t) obeys the following Hamilton-Jacobi evolution equation7, which we write as

$$\frac{\partial \varphi}{\partial t} + V(x,n)|\nabla \varphi| = 0 \tag{1.1}$$

where

$$n = \frac{\nabla \varphi}{|\nabla \varphi|} \tag{1.2}$$

is the surface normal and V(x, n) is the normal velocity.

Alternatively, if the vectorial form of interface migration velocity V is known, then the level set evolution equation can also be written in the following convection type form

$$\frac{\partial \varphi}{\partial t} + V \bullet \nabla \varphi = 0 \tag{1.3}$$

It is convenient to measure normal velocity in practice. Therefore, the Hamilton-Jacobi type equation shown in Eq. (1.1) will be adopted. Examination of Eq. (1.1) shows that the method is purely mathematical except for the choice of the velocity profile V(x, n). Hence, the only place the physics of the problem enters is through the choice of the velocity function. Once the velocity profile is

specified, the remaining task is the numerical integration of Eq. (1.1).

1.4 Objectives and motivation of the study

The objective of this study is mainly three parts: (i) to study the structural and optical property of the AlGaN/GaN MQWs fabricated on the FACELO GaN templates for the UV/blue light LEDs applications; (ii) to investigate the InGaN/GaN MQWs grown on the FACELO GaN templates and the different properties compared to that on the c-plane; (iii) to grow high crystal quality ZnO on the FACELO GaN templates. A combined approach of the study of the structural and optical properties on the epitaxial lateral overgrowth and the MOCVD growth of InGaN/GaN, AlGaN/GaN quantum wells structures and ZnO materials on the FACELO GaN templates will be presented. Characterization studies of the grown sample (RBS, TEM, SEM, XRD and PL) will provide a complete picture of the ELO growth.

In the present study, we will focus with the AlGaN/GaN and InGaN/GaN quantum well structures; both the structural and optical studies here may be of importance in explaining the interesting experimental results of these quantum well structures on the FACELO GaN templates. Furthermore, ZnO material was chosen from the II-VI compound materials as a foucs of this study because of the lower lattice mismatch (~1.9%) between ZnO and GaN. What we are mainly concerned with here is the controllable morphological change of ZnO growth on the FACELO GaN. Knowledge of these changes should provide useful information for application in future electronics and the fabrication of hybrid n-ZnO/p-GaN optoelectronic devices on sapphire.

The following Chapter 2 will briefly describe the MOCVD growth and RBS characterization technique.

Reference:

[1] H.P. Maruska, J.J. Tietjen, "THE PREPARATION AND PROPERTIES OF VAPOR-DEPOSITED SINGLE-CRYSTAL-LINE GaN" Applied Physics Letters **15,** 327 (1967).

[2] R. Dingle, D.D. Sell, S.E. Stokowski, M. Ilegems, "Absorption, Reflectance, and Luminescence of GaN Epitaxial Layers" Physical Review B **4,** 1211 (1971).

[3] J.I. Pankove, J.E. Berkeyheiser, E.A. Miller, "Properties of Zn-doped GaN. I. Photoluminescence" Journal of Applied Physics **45**, 1280 (1974).

[4] B. Monemar, "Fundamental energy gap of GaN from photoluminescence excitation spectra" Physical Review B **10,** 676 (1974).

[5] S. Nakamura, T. Mukai, M. Senoh, "Candela-class high-brightness InGaN/AlGaN double-heterostructure blue-light-emitting diodes" Applied Physics Letters **64,** 1687 (1994).

[6] J.-Y. Duboz, "GaN as Seen by the Industry" Physica Status Solidi (A) **176,** 5 (1999).

[7] Gerhard Fasol, "Long life for blue laser" Science **278**, 1502 (1997)

[8] F. Bernardini, V. Fiorentini, and D. Vanderbilt, "Spontaneous polarization and piezoelectric constants of III-V nitrides" Phys. Rev. B **56**, R10024 (1997).

[9] R. Langer, J. Simon, V. Ortiz, N. T. Pelekanos, A. Barski, R. André and M. Godlewski, "Giant electric fields in unstrained GaN single quantum wells" Appl. Phys. Lett. **74**, 3827 (1999).

[10] T. Nishida and N. Kobayashi, Compound Semiconductor. **5**, 12 (1999).

[11] H. M. Ng, "Molecular-beam epitaxy of GaN/$Al_xGa_{1-x}N$ multiple quantum wells on *R*-plane ($10\bar{1}2$) sapphire substrates" Appl. Phys. Lett. **80**, 4369 (2002).

[12] P. Waltereit, O. Brandt, M. Ramsteiner, R. Uecker, P. Reiche, and K. H. Ploog,

"Growth of M-plane GaN (1 $\bar{1}$ 0 0) on γ-$LiAlO_2$ (1 0 0)" J. Cryst. Growth **218**, 143 (2000).

[13] S. Nakamura, M. Senoh, S. Nagahama, N. Iwasa, T. Yamada, T. Matsushita, H. Kiyoku, Y. Sugimoto, T. Kozaki, H. Umenmoto, M. Sano and K. Chocho, Proceeding of ICNS'97, Tokushima, Japan, K. Hiramatsu (ed.) (1997), "Local strain distribution of hexagonal GaN pyramids" J. Cryst. Growth **189/190**, 820 (1998).

[14] Y. Iyechika, T. Maeda, K. Hiramatsu, K. Nishiyama, M. Onishi, H. Mizutani "Recent Progress in Selective Area Growth and Epitaxial Lateral Overgrowth of III-Nitrides: Effects of Reactor Pressure in MOVPE Growth" Phys. Stat. Sol. (a) **176**, 535 (1999)

[15] Du, D. X., Srolovitz, D. J., Coltrin, M. & Mitchell, C. Physical Review Letters "Systematic Prediction of Kinetically Limited Crystal Growth Morphologies" **95**, 155503 (2005).

[16] Du, D. X., Srolovitz, D. J., Zhou, H. & Chua, S. J. "The Merging Behavior of GaN Islands Grown by Selective Area Growth". (Submitted).

[17] Du, D. X., Srolovitz, D. J., Zhou, H. & Chua, S. J. "Growth Front Instability of GaN by Selective Area Growth". (Submitted).

[18] X.H. Wu, D. Kapolnek, E.J. Tarsa, B. Heying, S. Keller, B.P. Keller, U.K. Mishra, S.P. Den-Baars, and J. S. Speck, "Nucleation layer evolution in metal-organic chemical vapor deposition grown GaN" Appl. Phys. Lett. **68**, 1371 (1996).

[19] P. Vennegues, B. Beaumont, M. Vaille, and P. Gibart, "Microstructure of GaN epitaxial films at different stages of the growth process on sapphire (0 0 0 1)" J. Cryst. Growth **173**, 249 (1997).

[20] S. Amelinck, in: F.R.N. Nabarro (Ed.), Dislocations in Solids, vol. 6, Elsevier,

Amsterdam, 1982, pp. 67–460.

[21] T.S. Zheleva, O.-H. Nam, M.D. Bremser, and R.F. Davis, “Dislocation density reduction via lateral epitaxy in selectively grown GaN structures” Appl. Phys. **71**, 2472 (1997).

[22] S. Kurai, K. Nishino, and S. Sakai, “Nucleation Control in the Growth of Bulk GaN by Sublimation Method” Jpn. J. Appl. Phys. **36**, L184 (1997).

[23] J. Wang, S. Tottori, H. Sato, M.-S. Hao, Y. Ishikawa, T. Sugahara, K. Yamashita, and S.Sakai, “Lateral Overgrowth of Thick GaN on Patterned GaN Substrate by Sublimation Technique” Jpn. J. Appl. Phys. **37**, 4475 (1998).

[24] S.J. Rosner, E.C. Carr, M.J. Ludowise, G. Girlami, and H.I. Erikson, “Correlation of cathodoluminescence inhomogeneity with microstructural defects in epitaxial GaN grown by metalorganic chemical-vapor deposition” Appl. Phys. Lett. **70**, 420 (1997).

[25] T. Sugahara, H. Sato, M.S. Hao, Y. Naoi, S. Kurai, S. Tottori, K. Yamashita, K. Nishino, L.T. Romano, and S. Sakai, “Direct Evidence that Dislocations are Non-Radiative Recombination Centers in GaN” Jpn. J. Appl. Phys. **37**, L398 (1998).

[26] T. Hino, S. Tomiya, T. Miyajima, K. Yanashima, S. Hashimoto, and M. Ikeda, “Characterization of threading dislocations in GaN epitaxial layers” Appl. Phys. Lett. **76**, 3421 (2000).

[27] H. Marchand, J.P. Ibbetson, P.T. Fini, P. Kozodoy, S. Keller, S. DenBaars, J.S. Speck, and U.K. Mishra, “Atomic force microscopy observation of threading dislocation density reduction in lateral epitaxial overgrowth of gallium nitride by MOCVD” MRS Internet J. Nitride Semicond. Res. **3**, 3 (1998).

[28] E. S. Hellman, MRS Internet “The Polarity of GaN: a Critical Review” J.

Nitride Semicond. Res. **3**, 11 (1998).

[29] F. Bernardini, V. Fiorentini, and D. Vanderbilt, "Spontaneous polarization and piezoelectric constants of III-V nitrides" Phys. Rev. B **56**, R10 024 (1997).

[30] F. Bernardini, V. Fiorentini, and D. Vanderbilt, "Polarization-Based Calculation of the Dielectric Tensor of Polar Crystals" Phys. Rev. Lett. **79**, 3958 (1997); F. Bernardini and V. Fiorentini, "Electronic dielectric constants of insulators calculated by the polarization method" Phys. Rev. B **58**, 15 292 (1998).

[31] F. Bernardini and V. Fiorentini, "Macroscopic polarization and band offsets at nitride heterojunctions" Phys. Rev. B **57**, R9427 (1998).

[32] C.G. Van de Walle, R.M. Martin, "Theoretical calculations of heterojunction discontinuities in the Si/Ge system" Physical Review B **34,** 5621 (1986).

[33] J.S. Im, H. Kollmer, J. O, A. Sohmer, F. Scholz, A. Hangleiter, "Reduction of oscillator strength due to piezoelectric fields in GaN/AlxGa1-xN quantum wells" Physical Review B **57,** R9435 (1998).

[34] M. Leroux, N. Grandjean, M. Laugt, J. Massies, B. Gil, P. Lefebvre, P. Bigenwald, "Quantum confined Stark effect due to built-in internal polarization fields in (Al,Ga)N/GaN quantum wells" Physical Review B **58,** R13371,(1999).

[35] N. Grandjean, J. Massies, M. Leroux, "Self-limitation of AlGaN/GaN quantum well energy by built-in polarization field" Applied Physics Letters **74,** 2361, (1999).

[36] R. Langer, J. Simon, V. Ortiz, N.T. Pelekanos, A. Barski, R. Andre, M. Godlewski, "Giant electric fields in unstrained GaN single quantum wells" Applied Physics Letters **74**, 3827(1999).

[37] T.S. Zheleva, O.-H. Nam, M.D. Bremser, and R.F. Davis, "Dislocation

density reduction via lateral epitaxy in selectively grown GaN structures" Appl. Phys.Letters **71**, 2472 (1997).

[38] A. Sakai, H. Sunakawa, and A. Usui, "Defect structure in selectively grown GaN films with low threading dislocation density" Appl. Phys. Lett. **71**, 2259 (1997).

[39] S. Kurai, K. Nishino, and S. Sakai, Nucleation "Control in the Growth of Bulk GaN by Sublimation Method" Jpn. J. Appl. Phys. **36**, L184 (1997).

[40] J. Wang, S. Tottori, H. Sato, M.-S. Hao, Y. Ishikawa, T. Sugahara, K. Yamashita, and S. Sakai, "Lateral Overgrowth of Thick GaN on Patterned GaN Substrate by Sublimation Technique" Jpn. J. Appl. Phys. **37**, 4475 (1998).

[41] J. Park, P.A. Grudowski, C.J. Eiting, and R.D. Dupuis, "Selective-area and lateral epitaxial overgrowth of III–N materials by metal organic chemical vapor deposition" Appl. Phys. Lett. **73**, 333 (1998).

[42] O.-H. Nam, T.S. Zheleva, M.D. Bremser, and R.F. Davis, "Lateral epitaxial overgrowth of GaN films on SiO_2 areas via metalorganic vapor phase epitaxy" J. Electron. Mater. **27**, 233 (1998).

[43] K. Tadatomo, Y. Ohuchi, H. Okagawa, H. Itoh, H. Miyake, and K. Hiramatsu, "Hydrogen and Nitrogen Ambient Effects on Epitaxial Lateral Overgrowth (ELO) of GaN Via MOVPE" MRS Internet J. Nitride Semicond. Res. **4S1**, G3.1 (1999).

[44] H. Marchand, J.P. Ibbetson, P.T. Fini, X.H. Wu, S. Keller, S.P. DenBaars, J.S Speck, and U.K. Mishra, "Fast Lateral Epitaxial Overgrowth of Gallium Nitride by Metalorganic Chemical Vapor Deposition Using a Two-Step Process" MRS Internet J. Nitride Semicond. Res. **4S1**, G4.5 (1999).

[45] K. Hiramatsu, K. Nishiyama, A. Motogaito, H. Miyake, Y. Iyechika, and T. Maeda, "Recent Progress in Selective Area Growth and Epitaxial Lateral

Overgrowth of III-Nitrides: Effects of Reactor Pressure in MOVPE Growth" phys. stat. sol. (a) **176**, 535 (1999).

[46] D. Kapolnek, S. Keller, R. Vetury, R.D. Underwood, P. Kozodoy, S.P. Denbaars, and U.K.Mishra, "Anisotropic epitaxial lateral growth in GaN selective area epitaxy" Appl. Phys. Lett. **71**, 1204 (1997).

[47] J. E. Taylor, J. W. Cahn, and C. A. Handwerker, "Overview No. 98 I—Geometric models of crystal growth" Acta Metallurgica Et Materialia **40**, 1443 (1992).

[48] D. P. Peng, S. Osher, B. Merriman, et al., in UCLA CAM Report 98-51, 1998).

[49] G. Russo and P. Smereka, "A Level-Set Method for the Evolution of Faceted Crystals" Siam J Sci Comput **21**, 2073 (2000).

[50] S. J. Watson and S. A. Norris, "Scaling Theory and Morphometrics for a Coarsening Multiscale Surface, via a Principle of Maximal Dissipation" Phys Rev Lett **96**,176103, (2006).

[51] S. Osher and R. P. Fedkiw, "Level set methods and dynamic implicit surfaces" (Springer, New York, 2003).

[52] X. Zhang, R. R. Li, P. D. Dapkus, and D. H. Rich, "Direct lateral epitaxy overgrowth of GaN on sapphire substrates based on a sparse GaN nucleation technique" Appl. Phys. Lett. **77**, 2213 (2000).

Chapter 2

MOCVD growth and Rutherford Backscattering Spectrometry (RBS) characterization

2.1 Introduction

The III-nitrides materials require epitaxial process for growth with the better singular crystal qualities for higher performance devices. The growth of compound semiconductor superlattice structure with thickness on the order of ten to several hundred angstroms will certainly require epitaxial growth processes with precise control, including the ability to change composition within a period of a few angstrom in at least one dimension, and ultimately in two or three dimension. Other requirements imposed on current epitaxial growth processes include the ability to grow high-purity layers as well as to intentionally introduce impurities for n-type, p-type doping and for obtaining semi-insulating behavior. Several epitaxial techniques are currently available for the growth of semiconductor materials. In general, devices produced by Molecular Beam Epitaxy (MBE), Chemical-Beam Epitaxy (CBE) and MOCVD have very similar performance characteristics. The major attractions of MOCVD relative to the other techniques are the versatility and the demonstrated capacity for large-scale production. MOCVD is unquestionably the most versatile technique, suitable for the production of virtually all III/V and II/VI semiconductor compounds and alloys. It has also proven to be the most economical technique, particularly for the

production of devices requiring large areas, such as LEDs, photocathodes, and solar cells. In general, favorable economics require large-scale, high growth rates, and high yield of suitable material (i.e. uniformity and reproducibility). For this reasons, MOCVD research, development and production efforts have grown very fast during the last two decades. This Chapter will simply introduce the MOCVD system and the growth process.

Rutherford backscattering (RBS) is a powerful technique to characterize the composition, thickness, and interface of films directly and nondestructively. [7] It can determine the composition of the AlGaN and InGaN layers more reliably. RBS combined with channeling can provide useful information such as the crystalline quality and the defect density. Moreover, the angular scan around an off-normal axis can determine the tetragonal distortion induced by the elastic strain in the epilayer. Due to the depth sensitivity of this technique, RBS channeling can determine the strain in the epilayer as a function of depth.

2.2 MOCVD growth

The MOCVD growth of compound semiconductors is achieved by introducing source materials into a reactor chamber, which can be either a quartz tube or a stainless steel chamber, which contains a substrate placed on a heated carrier. A typical MOCVD system consists of four major parts (as shown in Fig 2.1): (1) gas handling system; (2) reactor chamber; (3) heating system and (4) exhaust system and safety apparatus. [1] The gas handing system includes the sources of alkyls and hydrides, and all of the valves, pumps and instruments necessary to control the gas flows and mixtures. Metalorganic sources are stored in stainless steel cylinders. The partial pressure of the source vapor is regulated by precisely controlling the temperature of the metalorgianc source bubbler. In order

to control the reaction precisely, mass flow controllers (MFC) is specifically designed to accurately and reliably measure and control the mass rate of gas flow. With the development of the solid state lighting industry, MOCVD has become a production tool for device structures in the III-nitrides. [2]

The reactants that are responsible for the deposition on a substrate can diffuse through a boundary layer - the region over the substrate with the laminar

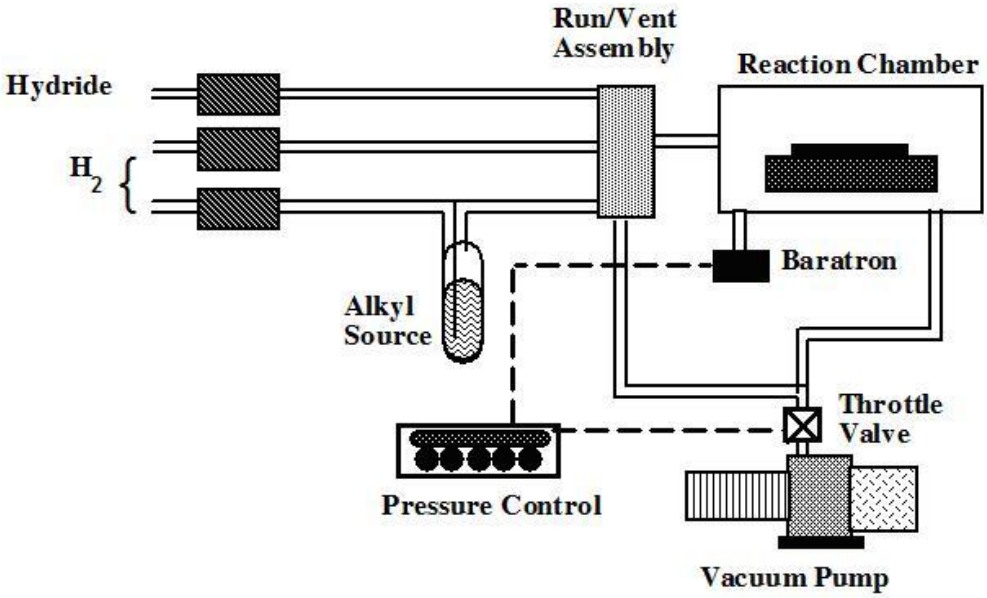

Fig. 2.1 The typical diagram of MOCVD system.

gas flow approaches zero velocity. As the reactants diffuse to the substrate, they traverse the region in which there exist strong temperature gradients. Depending on the thermal chemistry of the reactant, it may decompose partially or completely in this region. Most of the convenient metalorganics used in the MOCVD process decompose readily at relatively low temperatures. Similarly, the hydrides may decompose in the boundary layer. [3]

In the mass transport limited region the growth rate will be relatively independent of temperature owing to the small temperature dependence of the diffusivity of most gas species. In this region, the growth rate of GaN, for example, is faster than the transport of the reactants through the boundary layer and the

growth rate was found to be linearly dependent upon the input concentration of the reactant on. [4] This is the case for most of the MOCVD process. Outside of the mass transport region, the growth rate will not only be a sub-linear function of the partial pressure of the metalorganic, but also the substrate orientation, and/or the temperature. [5, 6]

All the nitride semiconductor samples discussed in this thesis were grown with an EMCORE D180 vertical geometry rotating-disk reactor MOCVD system. The reactor of D180 is based on EMCORE's proprietary TurboDisk technology, which uses a unique high speed rotating disc in a stainless steel growth chamber with integrated vacuum compatible loading chambers. To produce an epitaxial wafer, a bare substrate, such as sapphire or SiC, is placed on a wafer carrier in the TurboDisk growth chamber and heated to a high temperature. Based on a pre-determined mixture, metalorganic materials and hydride gases are introduced into the growth chamber together with a push gas. These gases decomposed on the hot, rapidly spinning wafer, depositing semiconductor materials such as GaN, InGaN and AlGaN to form a device structure.

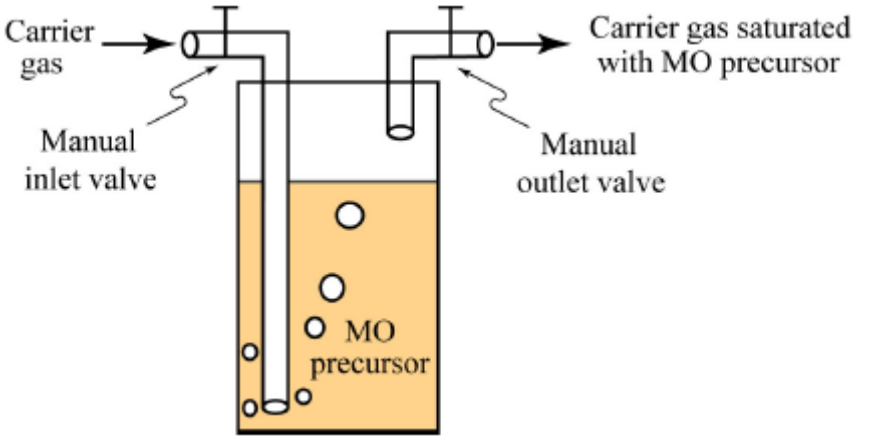

Fig. 2.2 Schematic diagram of a bubbler.

Trimethlgallium (TMGa), trimethylindium (TMIn) are used as the group-III precursors of gallium (Ga) and indium (In), respectively. As shown in Fig. 2.2, the metalorgnic (MO) precursor is contained in the bubbler. The carrier gas (N2 or H2)

flows into the bubbler, dissolves the MO precursor to form a saturated gas solution, and flows out of the bubbler. The vapor pressure of a MO precursor depends on the temperature. In order to keep a constant vapor pressure inside the bubbler, the bubbler is placed in a bath whose temperature is precisely controlled by a thermostat. The accuracy of the temperature control is usually 0.1°C. High-purified ammonia (NH_3) is used as the group V precursor of nitrogen (N). Highly purified hydrogen and nitrogen are used as the carrier gases. Table 2.1 lists the growth conditions for the undoped GaN epilayer used in this thesis. The typical growth rate for high temperature GaN is around 2μm/hour.

Table 2.1 Growth details for undoped GaN layer

Layer	Thickness	Growth Temperature (ºC)	NH3 flow rate (slm)	H2 flow rate (slm)	TMGa flow rate (sccm)
GaN layer	2 μm	1010	30	10	120
GaN buffer	10 nm	560	30	10	20

The desire for the maximum usage of reactor time and materials and a high yield for very complex structures virtually require that the process be monitored in situ during the growth process. Fortunately, a number of techniques for in situ monitoring of the MOCVD growth process have been developed in recent years. Ellipsometry is a tool long used for the characterization of thin films. It yields the film thickness and the refractive index, which can be used to obtain the composition of a ternary alloy. Early attempts to use this technique for monitoring

the MOCVD growth process were only partially successful, because of the complexities of implementing and interpreting the results. More recent studies using normal incidence reflectivity at single wavelength, from an external laser source, to monitor the growth have proven useful, the complex pattern (fingerprint) produced during the growth of a multilayered structure can be used to detect abnormalities in the growth process. A pattern is established for a successful growth run, and departures give an indication if problems in the growth process. This is a robust technique that is widely applicable for quality control. Application of sophisticated models allows the reflectance patterns to be interpreted in terms of the real-time growth rate and solid alloy compositions.

2.3 RBS characterization

Rutherford backscattering (or RBS, for Rutherford Backscattering Spectrometry) is an analytical technique in materials science. It is named after Ernest Rutherford who in 1911 first explained Geiger and Marsden's experimental results for alpha particle scattering from a very thin gold foil in a backward direction by using the Coulomb electrostatic force between the positively charged nucleus and the positively charged alpha particle. Rutherford first correctly described the atom as a tiny positive nucleus surrounded by negatively charged electrons (essentially the Bohr atom) on the basis of this experiment. This contradicted J.J. Thomson's "plum pudding model," the popularly accepted model of the atom at that time. Rutherford famously expressed his surprise at this experiment: "It was as though one fired a bullet at a piece of paper, and it bounced back at you!"

2.3.1 Ion channeling

The phenomenon of ion channeling was first reported in the early 1960's by Robinson and Oen. Detailed descriptions of ion channeling process, which can be found in Ref. 8 and Ref. 9, are summarized here.

When an incident ion beam is aligned with a major crystal direction (an

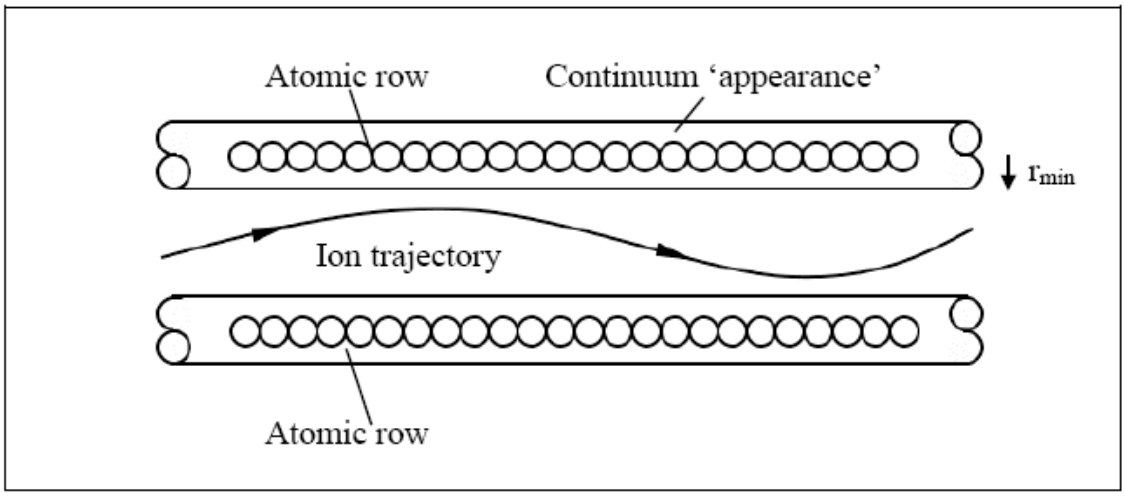

Fig. 2. 3. Schematic showing the trajectory of a channeled ion near atomic rows. The ion is gently steered by the row as long as it does not approach the row closer than r_{min}.

axial or a planar direction), the regular arrangement of atoms in a crystalline material has a very great effect on the passage of ions through the material. Ions traveling in the crystal are steered by Coulomb forces of the lattice atoms along crystal rows or planes. As long as the ions do not closely approach the lattice atoms, they are gently steered by a series of glancing collisions with these atoms. Fig. 2.3 schematically shows the steering effect of atomic rows on a channeled ion. The row is considered to be a continuous string of charge, found by averaging the contributions of the individual row atoms. The atomic nuclei and inner-shell electrons are shielded from the ion, resulting in reductions in yields of backscattered ions, X-ray and nuclear reaction products. This effect is described as 'channeling' and centers of the 'channels' are regions of lower electron density,

which leads to channeled ions suffering a lower energy loss rate than non-channeled ions.

2.3.2 RBS Instruments in CIBA

The Centre for Ion Beam Applications (CIBA) is equipped with a 3.5MV high brightness High Voltage Engineering Europa (HVEE) Singletron accelerator and three advanced beam lines. This facility can produce and focus the high-

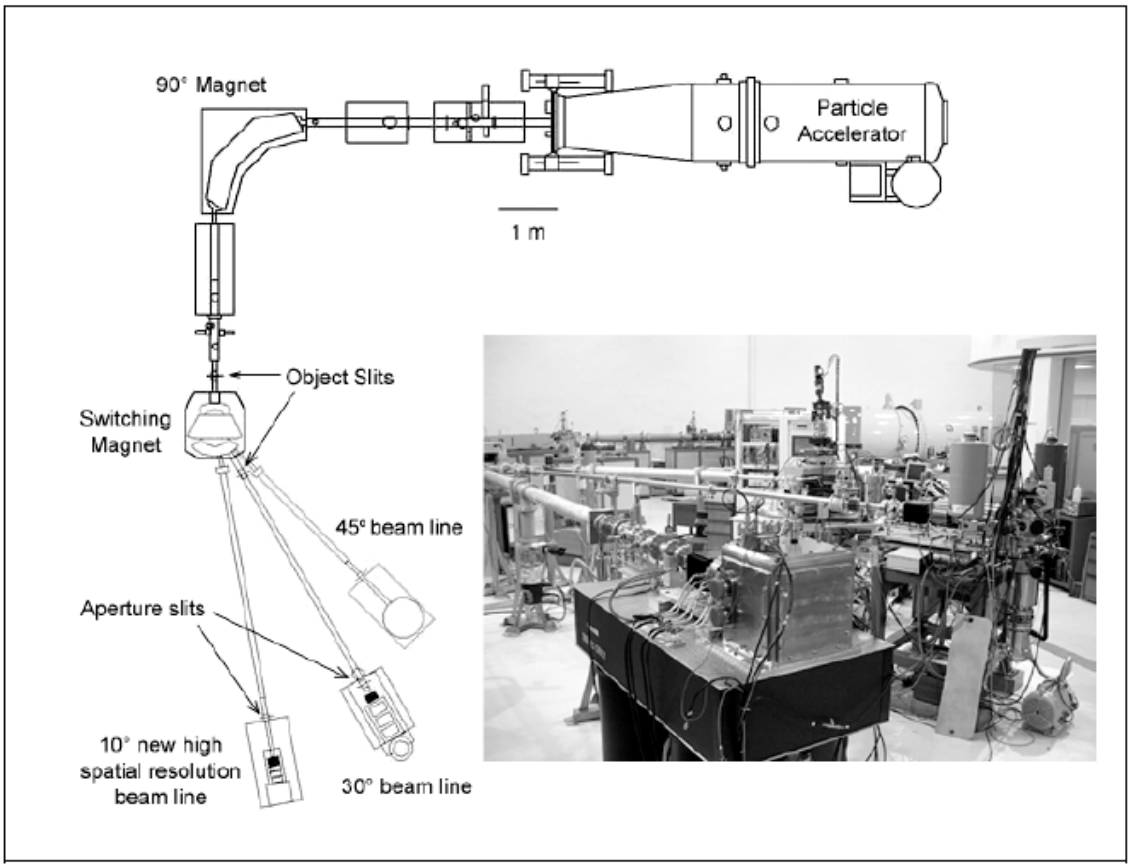

Fig. 2.4. Schematic diagram of the beam line facilities at the Center of Ion Beam Applications. Inset photograph shows the Singletron accelerator in the background and the foreground is the 10º beam line, the 30º beam line and the 45º beam line.

energy hydrogen beam down to 35×75 nm^2 [10]. It is worth noting that the 3.5MV accelerator is only one of three such high brightness accelerators worldwide.

A schematic overview of the Singletron accelerator facility is shown in Fig. 2.4. The main features of the Singletron accelerator are its high energy-stability of 6eV per hour and high beam-brightness. The accelerator uses a RF (Radio Frequency) ion source to generate hydrogen and helium ions. The source output is optimized by control of the source gas pressure and oscillator loading. The ions are accelerated in a tube constructed by sandwiching titanium electrodes between glass insulation rings.

The high voltage is generated by a series of solid-state rectifiers based on Cockcroft-Walton principle. The generating voltmeter (GVM) and voltage regulator are used to maintain voltage stability. This is important for limiting chromatic aberrations in the focusing system [11, 12], which is proportional to the energy spread of the ion beam from a high-energy accelerator and can deteriorate beam resolution of the nuclear microprobes. The accelerated ions are energy analyzed using a 90° analyzing magnet, where the species of ions are selected based on their charge to mass ratio. Using a switching magnet the high-energy ions can be directed into three different beam lines and associated target chambers. A set of beam defining object slits are positioned some distance away from the quadrupole lenses to define a rectangular object aperture. The transmitted beam through the aperture is de-magnified using a set of magnetic quadrupole lenses located directly in front of the target chamber. The de-magnified image of the object slits is transmitted into the target chamber. Separate object slits are used for the helium and hydrogen beams so that the hydrogen object slits do not get eroded easily by the heavier and more damaging helium beams.

The ion beam is focused with three Oxford Microbeams quadrupole lenses [12]. A quadrupole lens consists of four magnetic poles arranged N-S-N-S in a plane

perpendicular to the beam axis as shown in Fig. 2.3. Each quadrupole lens focuses the ion beam into a line. Therefore, at least two lenses arranged with alternating polarity are needed to focus the ion beam to a spot. In the CIBA nuclear microscope facility, three precisely constructed magnetic quadrupole lenses for optimal beam focus are used. They are arranged in converging-diverging-converging configuration in the horizontal plane with the excitations of the first two quadrupoles coupled. In this setup, they form a de-magnified image of the small object aperture on the sample surface under investigation. Since ion channeling imaging is a low-beam-current technique, particularly when a large acceptance angle detector is mounted behind the sample near the beam axis, the incident ion beam current may be less than 1fA [12]. This is achieved by significantly reducing the size of the object slits and aperture slits. Moreover, by limiting the energy spread and beam divergence with the object slits and aperture slits, it is possible to reduce the chromatic and spherical aberrations suffered by the ion beam passing through the quadrupole lenses [12, 14]. These result in a fine spatial resolution of a nuclear microscope for ion channeling analysis.

2.3.3 RBS channeling contrast microscopy (CCM)

The high-resolution nuclear microscope is a relatively new analytical instrument,

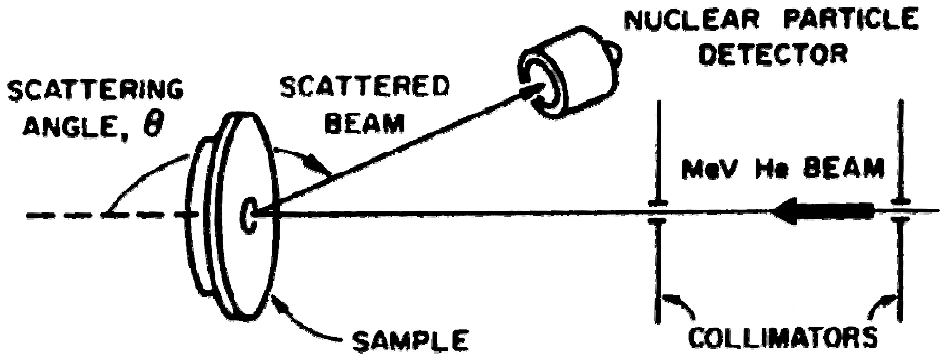

Fig. 2.5. The diagram of the setup structures of the RBS

which uses a focused MeV ion beam to scan samples and provide compositional and structural information on materials [12].

A high energy beam (2 to 4 MeV) of low mass ions (e.g. He++) is directed at a sample. A detector is placed such that particles which scatter from the sample at close to a 180 degree angle will be collected. (Fig. 2.5) Surface barrier silicon detectors are used in RBS. Since these devices are essentially diodes, they are often called semiconductor diode detectors. The high energy charged particles produce electron-hole pairs in the semiconducting material.

The detector is operated with an electrical potential (typically 4 kV) between the front and back surfaces. In the resulting electric field, the electron-hole pairs produce a current proportional to the energy of the charged particle. The average energy expended by He++ to produce one electron-hole pair is approximately 3.7 eV. This is sometimes called the ionization energy of the detector. Each 1 MeV particle produces about 2700 electron-hole pairs. The fluctuation or variance in the number of charge carriers affects the spectroscopic resolution. The theoretical minimum variance (which follows Poisson statistics) is equal to the number of charge carriers. The standard deviation equals the square root of the variance. The Fano factor is the ratio of the observed to this theoretical minimum variance. The Fano factor implicates other sources of peak broadening, typically incomplete charge collection and variations in dead layer loss.

Incomplete charge collection is minimized by high purity semiconductors which provide relatively few sites for electron-hole pair recombination. The energy lost before the charged particle reaches the active volume of the detector (dead layer loss) is minimal because this layer is thin (about 100 nanometer) in surface barrier detectors. Since this thickness corresponds to only about 0.4% energy loss for 1

MeV He++, small variations in the energy loss are insignificant for typical RBS experiments. High quality silicon surface barrier detectors are thus nearly ideal for alpha particle spectroscopy.

Particle arrival times at the detector are randomly spaced in time, leading to the possibility of interference between measurements when particles arrive at nearly the same time. This phenomenon, called pulse pile-up, becomes a serious problem at high particle arrival rates. There are two types of pile-up. Tail pile-up involves the superposition of pulses on the long duration tail or undershoots from a preceding pulse, leading to reduced spectral resolution. High quality electronic circuits minimize tail pile-up. Two pulses sufficiently close together to be treated as a single pulse undergo peak pile-up, the second type. Detector dead time is the minimum time between successive ion arrivals if they are to be measured separately. Peak pile-up ultimately limits the rate at which RBS data collection can occur.

The energy of these ions will depend on their incident energy and on the mass of the sample atom which they hit, because the amount of energy transferred to the sample atom in the collision depends on the ratio of masses between the ion and the sample atom. Thus, measuring the energy of scattered ions indicates the chemical composition of the sample.

Additionally, in the case that the incident ion doesn't hit any of the atoms near the surface of the sample, but instead hits an atom deeper in, the incident ion loses energy gradually as it passes through the solid, and again as it leaves the solid. This means that RBS can be used as a means to perform a depth profile of the composition of a sample. This is especially useful in analysis of thin-film materials. For example, films about half a micrometre in thickness can be profiled

using a 2 MeV He beam, or films up to about 10 micrometres thick can be profiled with a 2 MeV H beam.

For channeling analysis, when a focused ion beam is incident to a thin crystal along a channeling direction, channeled ions travel within regions of lower electron density and suffer a reduced energy loss rate (Fig. 2.6). These ions are back scattering by the crystal. All the back scattered ions are detected by a semiconductor detector directly placed on the beam axis, their energy is measured and an energy spectrum built up calibrated by the WSi. Local variations in the mean energy at each image pixel within the scanned area can be used to produce images showing the crystal property. This is the basis of the RBS ion channeling contrast microscopy (CCM) technique. For example, the back-scattering signal from a single crystal Si sample which is in channeling alignment along the <100> axis will be approximately 3% of the backscattering signal from a non-aligned crystal, or amorphous or poly-crystalline Si. By measuring the reduction in backscattering when a sample is channeled, it is possible to quantitatively measure and profile the crystal perfection of a sample, and to determine its crystal orientation.

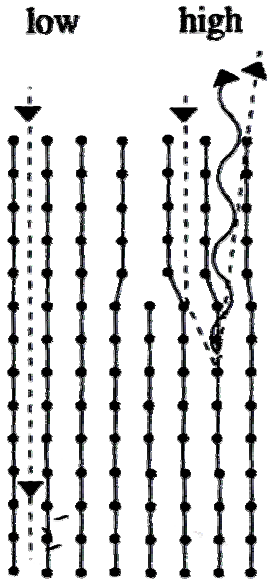

Fig. 2.6 Diagram of RBS CCM contrasts produced by the defects in the crystal locally raise the RBS and PIXE yield

There are many techniques available for the direct observation of crystal film property, such as X-ray topography, Optical Microscopy, and Transmission Electron Microscopy (TEM). For comparison, RBS ion channeling is able to investigate crystal property deeper into the surface than TEM and requires much

easier sample preparation than TEM, although presently with much poor spatial resolution. X-ray topography can use bulk samples and map crystal defects throughout their depth, but RBS ion channeling has a better spatial resolution than this technique.

2.4 Summary

In this chapter, some fundamental understanding of the MOCVD process is developed and the beam line facilities of the Center of Ion Beam Applications (CIBA), the interperation of the RBS, and the CCM technology are discussed. The epitaxial lateral overgrowth (ELO) of GaN and some simulation work will describe in the following chapter.

Reference:

[1] J. Ludowise, "Metalorganic chemical vapor deposition of III-V semiconductors" J. Appl. Phys. **58,** R31 (1985)

[2] D. Dupuis, "Epitaxial growth of III–V nitride semiconductors by metalorganic chemical vapor deposition" J. Cryst. Growth **178**, 56 (1997)

[3] G. B. Stringfellow, "A critical appraisal of growth mechanisms in MOVPE" J. Cryst. Growth **68**,111 (1984)

[4] P. D. Dapkus, J.J.Coleman, Chapter 4 in "III-V Semiconductor Materials and Devices" Edited by R.J. Malik, Elesevier Science Publisher. B.V., 1989

[5] D. H. Reep, and S. K. Ghaudi, "Deposition of GaAs Epitaxial Layers by Organometallic CVD" J. Electrochem. Soc. **130**, 675 (1983)

[6] P. Duchemin, M. Honnet, F. Koelsch, and D.Huyghe, "A New Method for Growing GaAs Epilayers by Low Pressure Organometallics" J. Electrochem. Soc. **126**, 1134 (1979)

[7] H. H. Andersen, J. Bottiger and H. Knudsen, *Ion Beam Analysis*, North-Holland, Amsterdam, 1980.

[8] W. K. Chu, J. W. Mayer and M. A. Nicolet, *Backscattering Spectrometry*, Academica Press, 1978.

[9] *Handbook of Modern Ion Beam Materials Analysis*, Materials Research Society, Pittsburgh, 1995.

[10] Doolittle, L.R. Conference proceedings, Heavy Ions, MRS. (1990)

[11] E. J. Teo, T. Osipowicz, A. A. Bettiol, F. Watt, Hao MS and Chua S.J., "Channeling contrast microscopy on lateral epitaxial overgrown GaN" Nucl. Instrum. Meth. Phys. Res. B, **181**, 231 (2001).

[12] T. Osipowicz, H.L. Seng, T.K. Chan and B. Ho "The CIBA high resolution RBS facility" Nucl. Instr. Meth. B, **249**, 915 (2006).

[13] Doolittle, L.R. Conference proceedings, Heavy Ions, MRS. (1990)

[14] M.B.H. Breese, E.J. Teo, M.A. Rana, L. Huang, J.A. van Kan, F. Watt and P.J.C. King, "Observation of Many Coherent Oscillations for MeV Protons Transmitted through Stacking Faults" Phys. Rev. Lett. **92**, 045503-1 (2004).

Chapter 3

Gallium nitride epitixial lateral growth:

Morphologies and simulations

3.1 Introduction

The lateral overgrowth rates and the equilibrium facets developed in the process depend on both the crystallographic orientation of the stripe openings and the growth parameters, such as temperature, V/III ratio in the vapour phase, pressure, composition of the carrier gas (H_2, N_2), fill factor (ratio of the stripe opening to the pattern period) [1–5]. It has been demonstrated that the lateral expansion is easier when the stripes are aligned along $<1\bar{1}00>_{GaN}$ direction [6]. With stripes

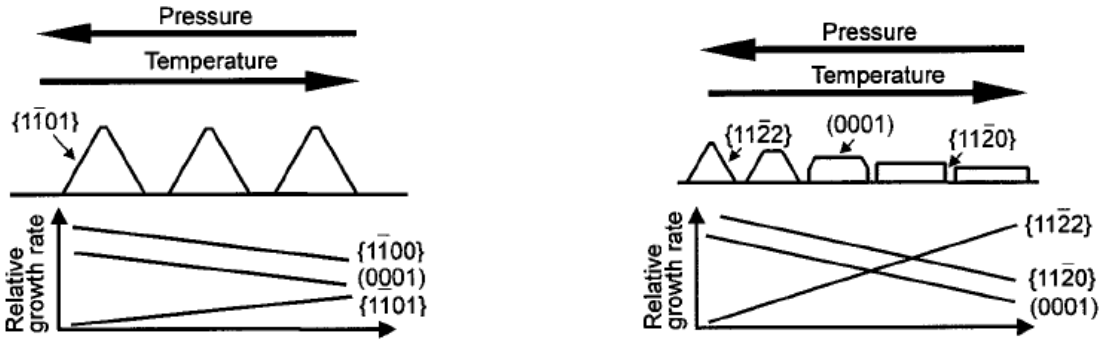

Fig. 3.1. Schematic evolution of the morphology of ELO GaN for $<11\bar{2}0>$ stripes (left) and $<1\bar{1}00>$ stripes (right) as a function of temperature and pressure (from Hiramatsu et al. [5])

aligned along the <1$\bar{1}$00> direction, the morphology gradually changes as the growth temperature increases, from triangular stripes to rectangular cross section with (0001) top facet and {11$\bar{2}$0} sidewalls [2]. These general trends are schematically shown in Fig. 3.1. Conversely, for stripes along the <11$\bar{2}$0> direction, the lateral overgrowth is limited by slow growing rate {1$\bar{1}$01} facets, which are the more stable faces in GaN. The lateral growth rate along the <1$\bar{1}$00> stripe is much faster than that one along <11$\bar{2}$0> [4, 7, 8]. We have found that these ELO GaN growth observations give us more undersatnading in the ELO epitaxy. A simple model of ELO growth [9] is further developed in this chpater. In addition, according to the development of the V-plot model described in section 1.3, some simulation work on the ELO GaN will also be introduced. Thus, a better fundamental understanding of the GaN crystal-facet-dependent growth kinetics is attractive which enable a better control and manipulation of ELO growth.

3.2.1 GaN lateral overgrowth with the stripe line pattern opening along <1$\bar{1}$00> and <11$\bar{2}$0>

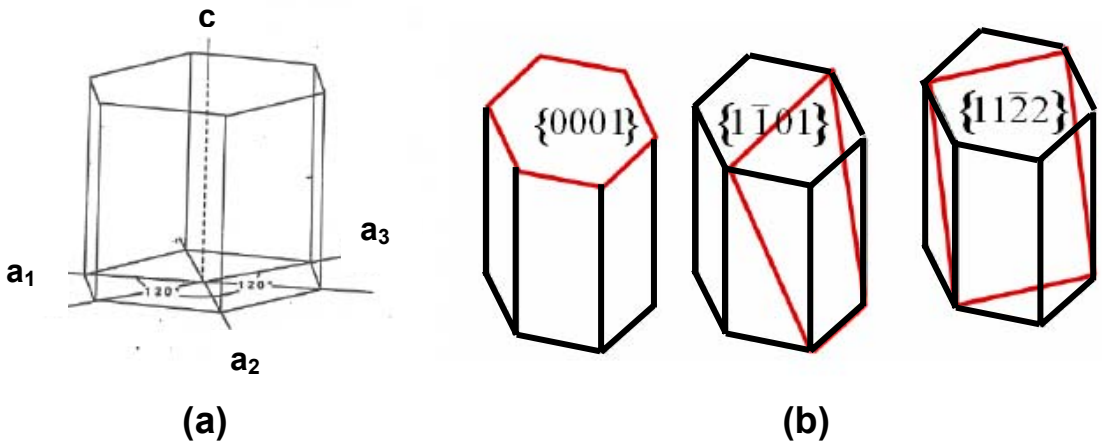

Fig. 3.2 Sketch of the crystallographic relationship of three facet planes. (a) The hexagonal unit cell. (b) The basal plane {0001}, {1$\bar{1}$01} facet and {11$\bar{2}$2} facet.

The crystallographic relationships of three facet planes are illustrated in Fig. 3.2. The lattice parameters of GaN are $a = 3.189\,\text{Å}$ and $c = 5.185\,\text{Å}$.

The angle between $\{1\bar{1}01\}$ plane and (0001) plane is

$$\theta_{(1\bar{1}01)} = \arctan\frac{c}{\frac{\sqrt{3}}{2}a} = 61.96° \tag{3.1}$$

The angle between $\{11\bar{2}2\}$ plane and (0001) plane is

$$\theta_{(11\bar{2}2)} = \arctan\frac{c}{a} = 58.41° \tag{3.2}$$

Note, the lattice parameters will vary with temperature. However, the influence of the temperature on the angles is small.

In the ELO process, growth does not occur on the dielectric mask. Therefore, the Gallium molecular species brought to the growing interface are not depleted over the mask, thus creating an additional supply of active species that can be transported via diffusion to the open areas. This leads to a growth rate enhancement in the open regions, which will drop-off between the openings. A model based on the steady state gas-phase diffusive transport and growth rate enhancement has been proposed by Coltrin et al. [9]. Neglecting most of the details of the reaction chemistry, one can usually calculate reasonably accurate growth rates by treating the growth as a first-order reaction of the limiting species that reacts at the surface with an empirical ‘‘sticking coefficient”. Indeed, it was shown that the growth rate g can be empirically linked to the fill factor Θ defined as w/ (w + m) by a simple power-law:

$$g = g_0\,\Theta^{-0.862}, \tag{3.3}$$

where g is the growth rate with various fill factor Θ and g_0 is the growth rate without masking, w is the width of the opening and m is the masked width.

During the overgrowth, the dimension m of masked regions decreases, thus Θ increases continuously. Therefore, as the calculations show that g should drop continuously as the overgrowth proceeds to finally reach g_0. From Eq. (3.3), a simple integration gives the growth front as a function of time. Thus, a better fundamental understanding of the GaN crystal-facet-dependent growth kinetics is important for the better control and manipulation of growth conditions.

A simple model of ELO growth will be discussed later. That also shows how the progress of feature growth can be understood in terms of a dimensionless quantity. This new analysis provides the basis for extracting the kinetic behavior of the growing crystal features.

3.2.2 Experimental results and discussion of epitaxial lateral overgrowth GaN with stripe line pattern

For the study of the ELO GaN growth, a 2 μm layer of GaN was grown on a sapphire substrate and then coated with a 0.1 μm SiO_2 layer. A series of stripe patterns were etched through the SiO_2 mask layer along the $<1\bar{1}00>$ and $<11\bar{2}0>$ directions, exposing the underlying GaN. The dimensions in each pattern are denoted as *w*: *m*, where *w* is the width of the GaN unmasked area, which was constant with 2 μm, and *m* is the width of the masked area, which was varied from 5 to 358 μm. A pattern fill factor α is defined as $\alpha = w/(w + m)$, and the period is defined as $w + m$; i.e., the repeat length of the pattern. The complete set of patterns on the mask includes: 2:5, 2:20, 2:38, 2:69, 2:125, 2:222 and 2:358, oriented in the $<1\bar{1}00>$ direction and in the $<11\bar{2}0>$ direction (referenced to the GaN crystal, i.e. for the miller index). Upon further MOCVD growth, GaN growth proceeds first through the stripe window area. The GaN was grown in the EMCORE D180

MOCVD system. Trimethyl-gallium and ammonia (NH_3) were used as precursors of Ga and N, respectively, with H_2 as carrier gas. The selective GaN layers were grown via controlling the growth temperature and the reactor pressure (950ºC, and 1000ºC with pressure 500 Torr). All the growth duriation was 30minutes.

Fig.3.3 and Fig 3.4 show the cross sectional SEM of ELO features grown at the temperature of 950ºC, and 1000ºC, with pattern dimensions 2:20, 2:38, 2:69, and 2:125 oriented in the <1$\bar{1}$00> direction. The first number refers to the window

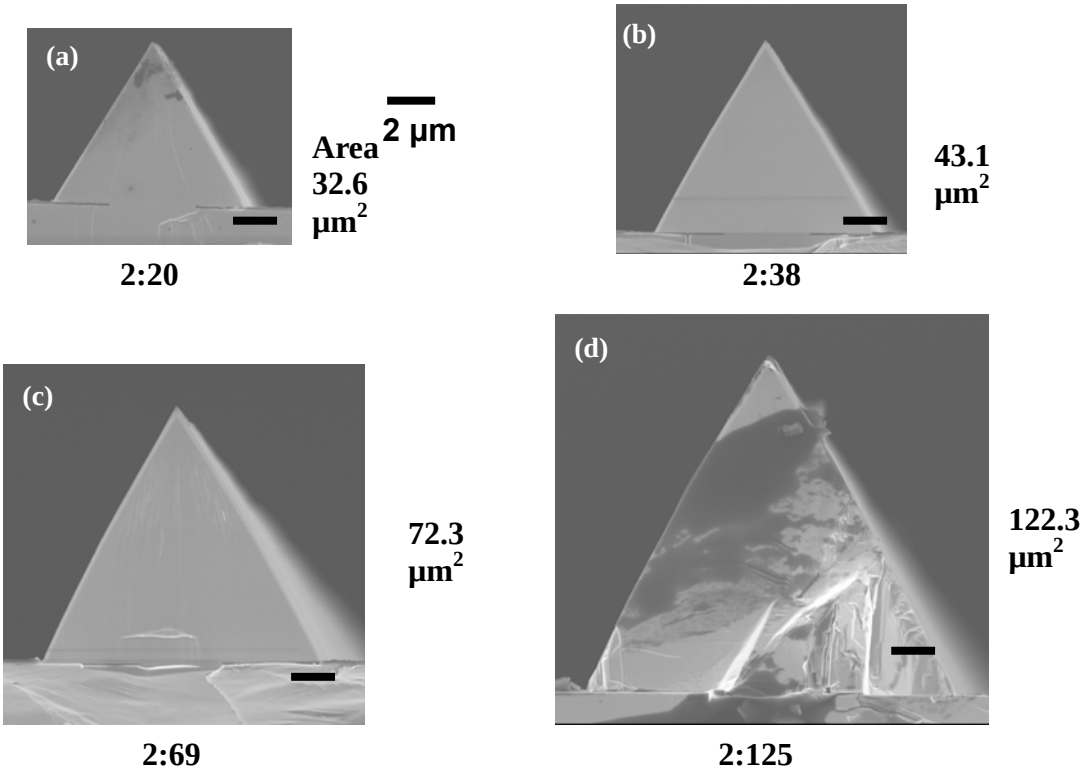

Fig. 3.3. Cross-sectional SEM images for a series of ELO GaN grown with 2 µm window openings and mask widths ranging from 20 to 125 µm. The growth temperature is 950 ºC. Measured cross-sectional areas are listed next to each feature. Magnification scale is the same in each image.

opening *w* in µm, and the second to the width of the masked region (i.e. the distance between the openings) between lines *m* in µm. The images are all displayed at the same magnification scale to illustrate the increase in growth rate

on the exposed features as the fraction of the surface covered by the mask width is increased. Listed next to each feature's image is its cross sectional area of the triangle in μm^2.

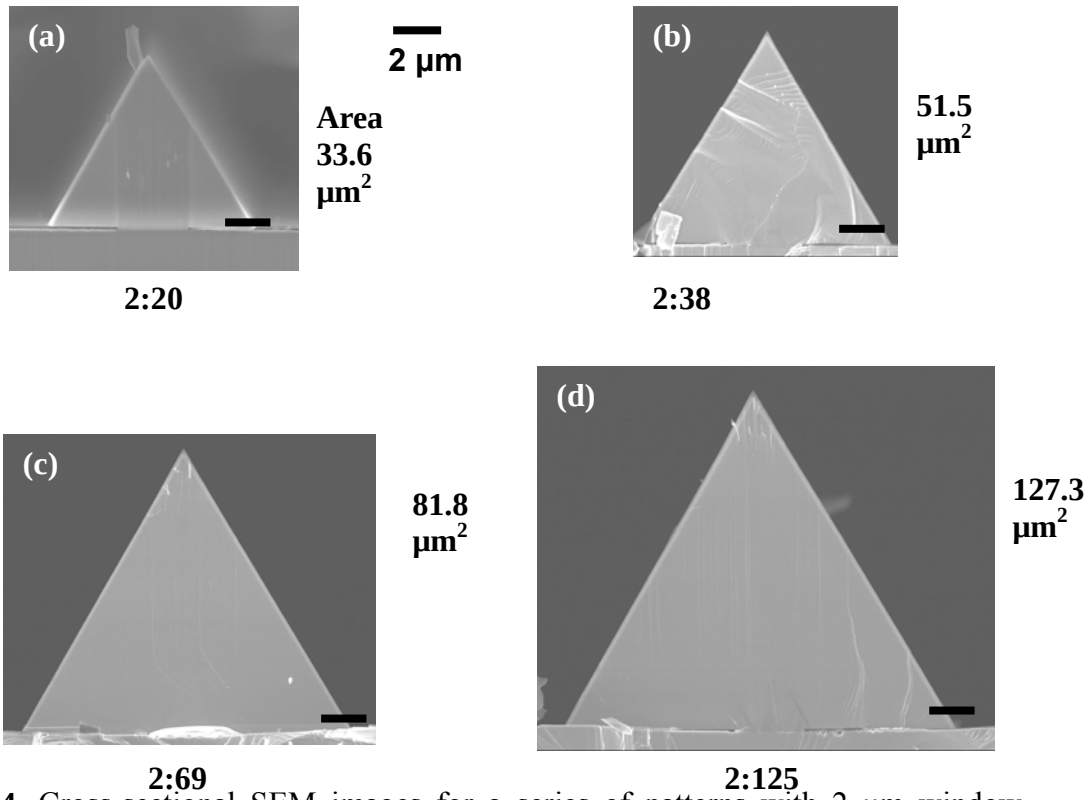

Fig. 3.4. Cross-sectional SEM images for a series of patterns with 2 μm window openings and mask widths ranging from 20 to 125 μm. The growth temperature is 1000 ºC. Measured cross-sectional areas are listed next to each feature. Magnification scale is the same in each image.

The rotating-disk reactor is often used in MOCVD for compound semiconductors; background on the behavior and operation of the rotating disk reactor can be found in Refs. [10–18]. In this type of reactor, dilute reactants accompanied by a carrier gas, typically in great excess, are introduced through the top of the reactor at near room temperature. The drag caused by the rotational motion of the heated disk draws the gas down toward the surface. The incoming gas flow picks-up circumferential and radial velocity components and the axial velocity drops from its free stream value to zero at the surface as the nearby

effects of the disk begin to dominate. The gas heats due to convective heat transfer from the disk. Depending on the chemical system, gas-phase chemistry may take place either in the relatively cool incoming gas stream, or in the heated region near the disk. Deposition of material at the solid surface removes reactant species from the gas, setting up a concentration gradient between the incoming gas stream and the disk surface, causing diffusive transport of reactant species toward the surface. The changes in velocity, temperature, and concentration fields described above all take place within a thin region just above the disk denoted as the ‘‘boundary layer.’’ However, each of these three fields has a different boundary layer thickness, but in practice they are very similar in extent [16]. In this work, we are primarily concerned with transport of species across the concentration boundary layer.

In the MOCVD growth of compound semiconductors, the growth rate is limited by the supply of one of the reactant materials, any other reactants are available in much greater excess [17]. Neglecting most of the details of the reaction chemistry, one can usually calculate reasonably accurate growth rates by treating the growth as a first-order reaction of the limiting species that reacts at the surface with an empirical ‘‘sticking coefficient’’ (probability), γ [16].

The boundary condition of the reactant species concentration at the surface is given by [16]

$$kN_S = D\frac{\partial N}{\partial z} \tag{3.4}$$

where k is the rate constant for the first-order heterogeneous surface reaction, Ns is the gas-phase concentration of the (limiting) reactant species at the interface with the surface, D is the reactant gas diffusion constant, N is the gas-phase concentration of the reactant species, and z is height above the surface. The molar

growth rate V equals to the left-hand (or right-hand) side of Eq. (3.4). The rate constant k is simply related to the reaction probability γ by [16]

$$k = \gamma \sqrt{\frac{RT}{2\pi M}} \tag{3.5}$$

where R is the gas constant, T is the temperature (K), and M is the reactant species molecular weight. If a reaction probability is 1, then Eq. (3.5) gives a heterogeneous first-order rate constant of k = 15,850 cm/s for M=69.72 g/mol (Ga atom) at T =1223 K.

The consumption of growth species at the interface leads to a lower concentrations at the interface than in the boundary layer region. Such a concentration gradient leads to a flux of growth species onto the interface, as described by the Fick's first law [16]. It is not surprising that the concentration gradient of the growth species will depend on how fast the sources are consumed at the interface. Based on exact fluid and diffusion models, we could assume that there is a thin boundary layer near the interface, in which the concentration varies linearly. Then Eq. (3.4) can be rewritten as

$$kN_S = D\frac{N_i - N_s}{\delta} \tag{3.6}$$

where Ni is the inlet concentration. Eq (3.6) can be rearranged to give

$$\frac{N_s}{N_i} = \frac{1}{1 + D_a} \tag{3.7}$$

where Da is the surface Damkohler number, defined to be

$$D_a = \frac{k\delta}{D} \tag{3.8}$$

The (dimensionless) Damkohler number is a measure of the relative speeds of chemical reaction versus diffusive transport.

If we let V be the growth rate of material deposited on the exposed ELO feature, and V_0 be the blanket growth rate that would have occurred over the entire width without SiO_2 mask, then we define the ELO efficiency κ as V/V_0. So we can derive an analytical expression for the ELO efficiency:

$$\kappa \equiv \frac{V}{V_0} = \frac{\alpha(1+D_a)}{1+\alpha \cdot D_a} \tag{3.9}$$

where α is the fill factor. For without mask growth, then kinetic processes are much faster than mass transport; the growth effiency can be noted by 100 %. This is typically the case for GaN MOCVD growth. It is easily seen from Eq. (3.9) that essentially unit efficiency should be observed when D*a*>>1. It is also seen that the unit efficiency should yield a straight line if we plot the growth feature cross sectional area versus the period distance and the slope of the line should depend on the growth rate. Due to higher temperature will lower the blanket growth rate of c-direction, the 100% efficiency line of 1000 ºC has smaller slop than the 950 ºC, as shown in Fig. 3.5. A plot of ELO feature cross-sectional area versus the pattern repeat distance ($w + m$) is shown in Fig. 3.5. Fig. 3.5 plots the feature cross-sectional area versus period distance ($w + m$) from the SEM data of

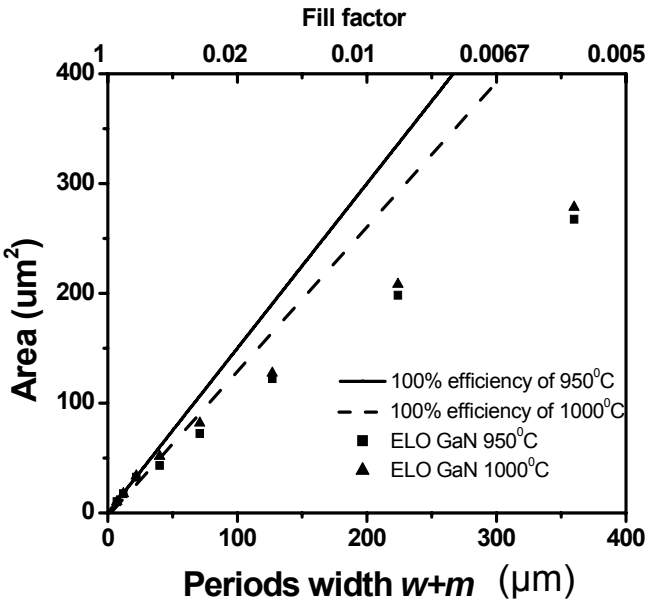

Fig. 3.5 Cross-sectional areas of the ELO features showed in the Fig. 3.3 and Fig. 3.4 versus pattern period width for the strip opening in the <1 $\bar{1}$ 00> direction.

Fig.3.3 and Fig 3.4, showing liner dependence at the larger fill factor ($0.05<\alpha<1$, or $0< w + m<10$) but nonlinear with the smaller fill factor (i.e., $\alpha<0.03$ or $w + m>33$). This can be explained by the Eq. (3.9), because the growth efficiency will decrease when the fill factor decreased, so the samller fill factor will be far away to the 100 % effiency line. So it is why Fig. 3.5 showing liner dependence at the small pitch width ($0.05<\alpha<1$, or $0< w + m<10$) but yields the drop in the efficiency seen in the plot with the larger pitch width (i.e. $\alpha<0.03$ or $w + m>33$). With the mask area width m increased, the active species diffusion from the mask area will reach kinetic equilibrium after m beyond the active species diffusion length. It will restrain the ELO growth efficiency, so the larger pitch width will lead to the lower ELO efficiency. From the Fig. 3.5, it also can be seen that the higher growth temperature gives higher ELO growth efficiency. With Eq. (3.9), the efficiency will increase with larger Damkohler number Da and with constant fill factor α. Based on the definition Eq. (3.8), Da will increase due to higher

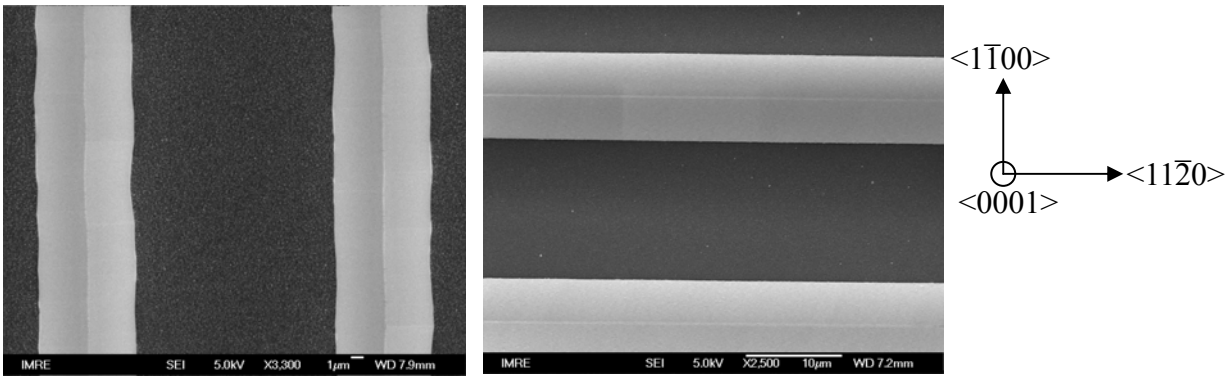

Fig. 3.6. The top view SEM of the ELO GaN grown on the two different strip line patterns.

temperature which induced the higher ELO growth efficiency as predicted from the Eq. (3.9). This is shown to be the case in Fig 3.5 where the areas grown at the higher temperature at 1000 ºC compare to that at the lower temperature 950 ºC.

Two different patterned line directions <1$\bar{1}$00> and <11$\bar{2}$0> were also

studied, the ELO feature sidewalls are {11$\bar{2}$2} faces along the <1$\bar{1}$00> direction compare with the {1$\bar{1}$01} facets along the <11$\bar{2}$0> direction. Figure 3.6 shows the two different stripe direction pattern with ELO GaN grown at 1000 ºC. Fig.3.7 plots the feature cross-sectional area versus period distance ($w + m$) from the SEM data of Fig.3.6. It is clearly shown that the {11$\bar{2}$2} facets is a faster growth facets compare to the {1$\bar{1}$01} facet. This result is consistant with the conclusion of the reported in publish literature [4, 7, 8].

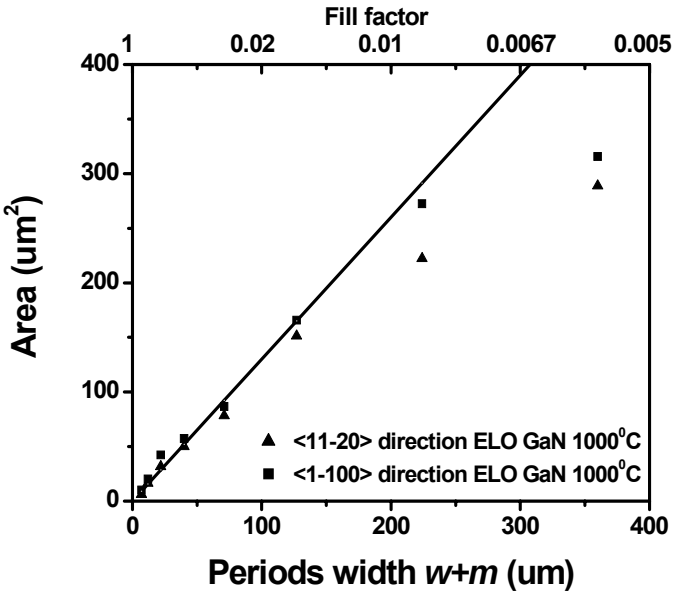

Fig. 3.7 Cross-sectional areas of the ELO features showed in the Fig. 3.6 versus pattern period width.

In summary, the ELO growth efficiency can be described by the growth parameters like growth temperature or fill factor. With the simple model that developed by using the boundary layers, the cross section area of the ELO GaN is understoodable. Such results will be useful for the future design of the ELO GaN material growth.

3.3 Growth front instability and the merging behavior of ELO GaN

3.3.1 Growth front instability of GaN by ELO

During thin film semiconductor growth, flat semiconductor crystal surfaces are usually preferred. However, the surface roughness during thin film growth is common. There are two major sources of the waviness of a flat surface. On one hand, a flat surface is roughened by thermodynamic forces due to either internal fields (e.g., mismatch strain [19, 20] or external fields (e.g., electric field[21,22]). On the other hand, a supposedly flat surface can also be roughened by geometric factors due to imperfect growth conditions (e.g., miscut of substrate surface or mis-etching of the mask patterns used in selective area growth). Although the mechanism of the first type of roughening is well understood, the consequence of the second type of roughening and its difference corporated with the first type of roughening is not fully appreciated. The understanding is further hindered by the fact that thin film crystals are usually faceted. Recently, we use epitaxial lateral overgrowth of GaN as an example and study the stability of the $\{11\bar{2}2\}$ facets. It is shown (through both analysis and simulation) that, unlike the thermodynamic driven instability, the wavy feature on the fast growing front is only transient.

The experiment was carried with GaN grown by MOCVD growth. An initial 2 μm layer of GaN was grown on a sapphire substrate and coated with a 100 nm SiO_2 layer. The patterns were etched through the mask layer with two different directions $<1\bar{1}00>$ and $<11\bar{2}0>$, exposing the underlying GaN. Upon

further MOCVD growth, GaN growth proceeds first through the window area etched into the mask and then both vertically and laterally across the surface of the SiO_2 mask layer. Trimethyl-metals and ammonia (NH_3) were used as precursors of Ga and N, respectively, with H_2 as carrier gas. The selective GaN layers were grown via controlling the growth temperature and the reactor pressure (preferably 950 ºC and 500 Torr).

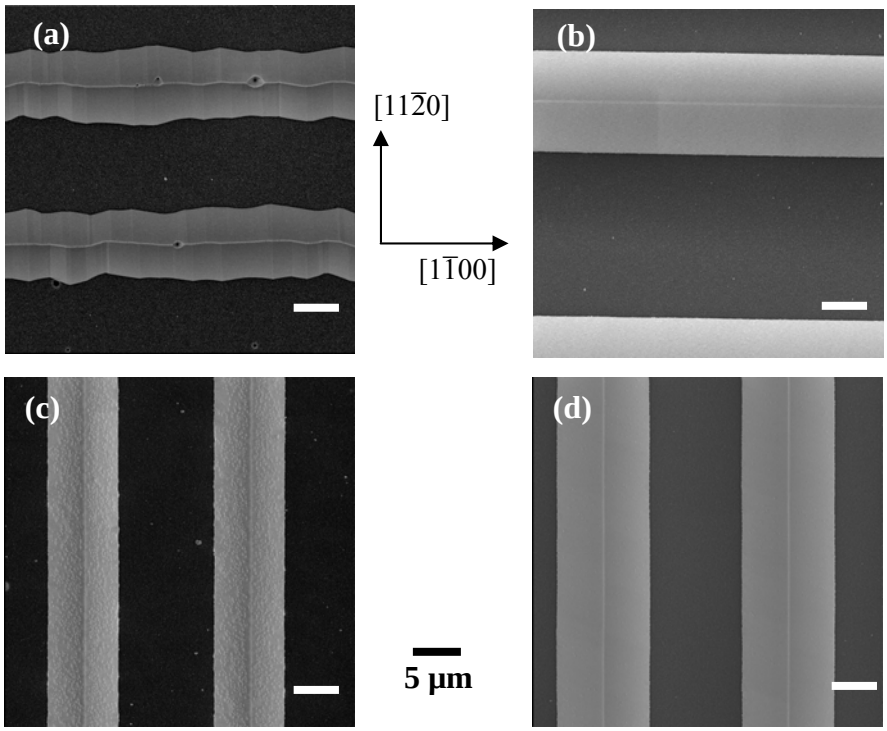

Fig. 3.8 ELO growth of GaN using stripe pattern aligned along <1$\bar{1}$00> direction with growth time 30 mins (a), 40 mins (b); and stripe pattern aligned along <11$\bar{2}$0> direction with growth time 30 mins (c) and 40 mins (d). Magnification scale is the same in each image.

Fig. 3.8 shows the experimental results of surface roughness on stripe line type patterns during ELO growth of GaN. Fig. 3.8(a) and 3.8(b) show the ELO GaN using stripe line pattern aligned along [1$\bar{1}$00] direction with growth time is 30 mins and 40 mins respectively. The facets {11$\bar{2}$2} of 30 mins growth sample shows obvious perturbations with the rough surfaces. There are curved regions, {11$\bar{2}$2} facets, and small facets with orientations close to (10$\bar{1}$1) or (01$\bar{1}$1). The

perturbations on the {11$\bar{2}$2} facets clearly are undesirable for various application of GaN, e.g. quantum well structures growth. Fig. 3.8(b) shows the ELO growth

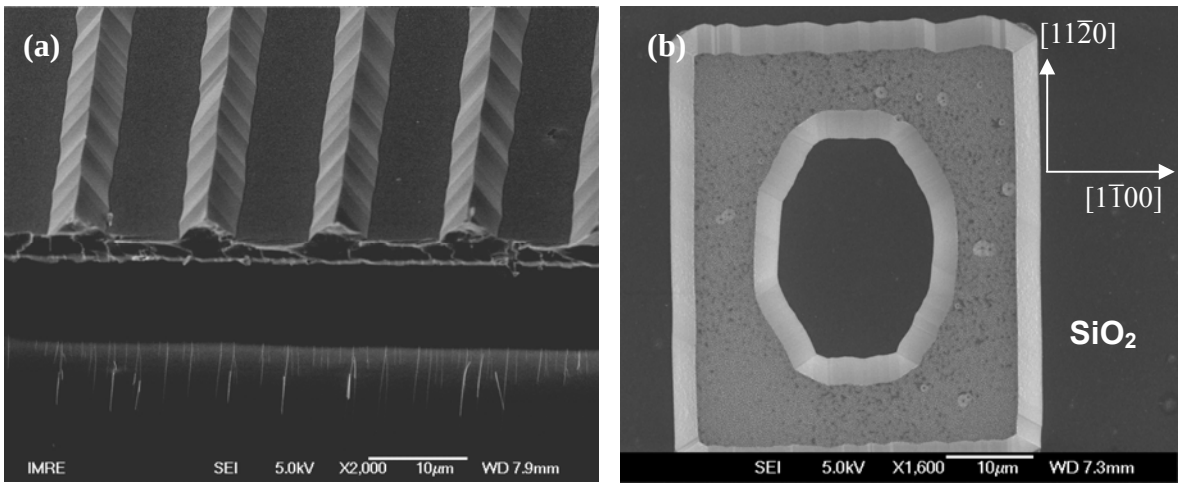

Fig. 3.9 (a) bird view of the SEM of ELO GaN using stripe pattern aligned along <1$\bar{1}$00> direction with growth time 30mins. (b) ELO growth of GaN using polygonal ring pattern. Along the retangular boundary of the pattern, the fast facets {11$\bar{2}$2} show perturbation and the slow facets {1$\bar{1}$01} are smooth.

of GaN from stripes aligned along [1$\bar{1}$00] direction for a growth time of 40 mins (rather than 30 mins as shown in Fig. 3.8(a). It can be observed that in this case, the surfaces are much smoother, flatter facets than in the 30 mins growth. Fig. 3.8 (c) and (d) shows the ELO growth of GaN along the <11$\bar{2}$0> direction with growth time 30 mins and 40 mins, respectively. Both of these two samples with smooth {1$\bar{1}$01} facet were observed. This different morphology between these two different directions also can be seen from the Fig. 3.9 (b), which is the ELO growth of GaN using a polygonal ring pattern. So the {1$\bar{1}$01} growth front is invariably smooth and the {11$\bar{2}$2} growth front is rough.

To explain these growth results, our collabrators Dr. DanXu Du and Prof. David Srolovitz carried out the simulation work of our ELO GaN growth. According to the development of the V-plot model and level-set simulation method [23, 24], the crystal growth features should be dominated by slow facets.

Therefore, a slow growing front should be stable against perturbations, i.e., perturbations will quickly disappear resulting in flat facets (stresses within the islands should be too small to induce an Asaro-Tiller instability [25] at these length scales). This conclusion is based on the fact that there are no strong internal fields or external fields which cause a flat surface to be thermodynamically unstable. Based on the relative velocities for the facets, we can interpolate to find the V-plot. The V-plot must be consistent with the features of the cusps, crystal symmetry and lower bound obtained in previous steps. Furthermore, this V-plot must be able to reproduce the kinetic Wulff shape (the asymptotic crystal shape).

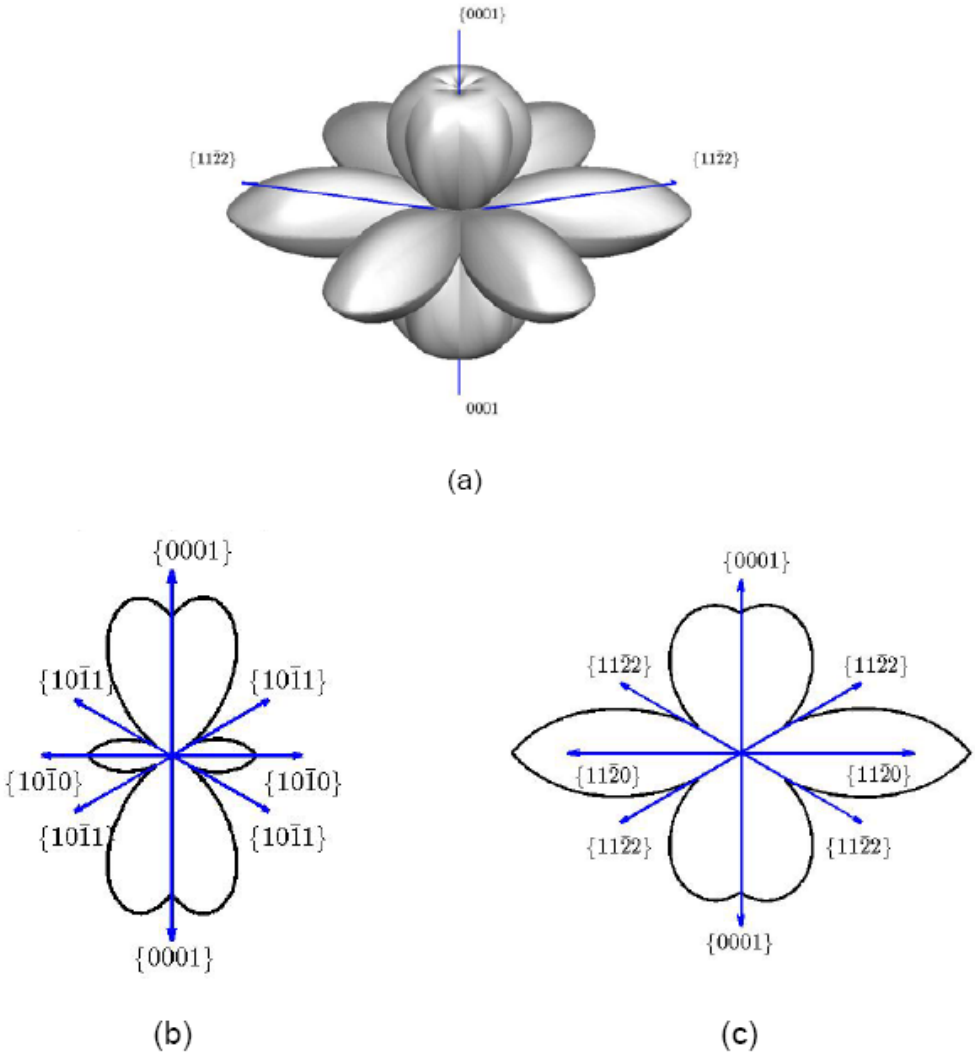

Fig. 3.10 The v-plot: (a) a 3-d view, (b) a $\{11\bar{2}0\}$ cross-section, and (c) a $\{1\bar{1}00\}$ cross-section. (Ref. 24)

A working V-plot obtained is shown in Fig. 3.10. Each surface of the V-plot was represented by a trigonometric function chosen such that it is smooth and satisfies the correct properties. Hence, the V-plot is a piece wise continuous closed surface. While not unique, this V-plot is compatible with all of the constraints mentioned above. Figure 3.10 (a) shows the 6-fold rotational symmetry. Two cross-sections of the V-plot are shown in Fig. 3.10 (b) and 3.10 (c) for $(11\bar{2}0)$ and $(1\bar{1}00)$ cross-sections, respectively. And the $(11\bar{2}2)$ facets are defined as the fast growth face compared to the $(1\bar{1}01)$ facets which are the slow growth face, meanwhile the growth speed along $<11\bar{2}0>$ direction is faster than the $<1\bar{1}00>$ direction. These two crosssections illustrate that this behave as constrained by the experimental results. At the same time, for ring patterns or for free standing growth, a fast growing front will quickly disappear during crystal growth and the growth will be quickly dominated by surfaces with slow growth velocities[23, 24].

The level set simulation and V-plot model developed previously (detailed level set method and related simulation can be found in reference [24, 25]) to

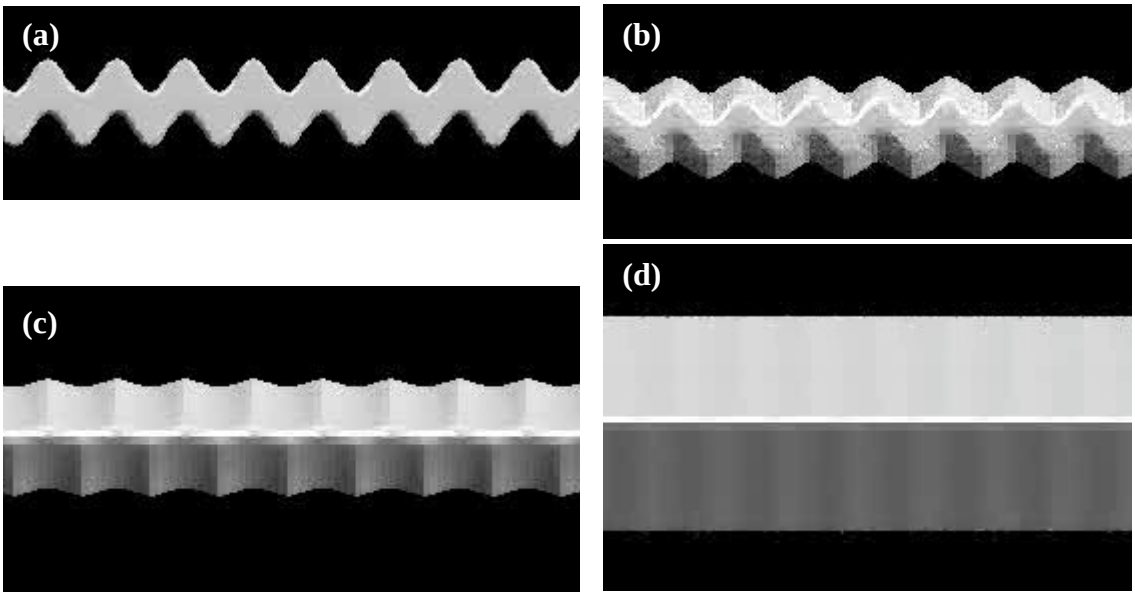

Fig.3.11 Simulated time evolution of a stripe pattern aligned along $[1\bar{1}00]$ direction that is initially strongly perturbed at times of (a) 0, (b) 34, (c) 74 and (d) 205. The growth fronts asymptotically approach flat surfaces.

simulate the growth on stripe opening mask patterns. To verify this conclusion, we perform level set simulations of the growth of the stripe island morphology, assuming only that the surface growth rates are as described as per the experimentally determined V-plot. For more details of the simulation method and the deduced V-plot, the reader is referred to Ref. 25. Figure 3.11 shows several images during the simulation of the evolution of a stripe to which a relatively large amplitude surface perturbation is added. That is, the initial mask pattern is of the form $h(y) = b[\pm 1 + a\sin(ky)]$, where y is the coordinate along the $[1\bar{1}00]$ direction, the nominal line thickness is $2b$ and the perturbation amplitude (dimensionless) and wavelength are a and $2\pi/k$. The initial pattern is shown in Fig. 3.11(a). The amplitude of the perturbation is exaggerated to demonstrate the stability against strong perturbation. An image, taken at an intermediate time step (t = 34) is shown in Fig. 3.11(b). It can be seen that slow $(10\bar{1}1)$ and $(01\bar{1}1)$ facets develop on both side of the GaN stripe. Also, sharp edges develop at the corners (trough) due to coalesce of two fast growth surfaces on both sides of the trough. Fig. 3.11(c) shows an image corresponding to time t = 74. It can be observed that the sharp edge, as shown in Fig. 3.11(b), becomes rounded at later times. This is due to the fact that there is only one fast facet orientation between the two bounding orientations (the two slowing facets around the tips). Furthermore, the curved regions spread from the trough towards crest. The asymptotic shape at time t = 205 is shown in Fig. 3.11(d). It can be observed that the surface is almost flat. Numerically determined surface direction indicate that the flat surfaces have the $\{11\bar{2}2\}$ orientations. This result clearly contradicts the experimental observation of lines with rough surfaces.

Since the simulations clearly show that at long times the surface roughness

must decay, we must conclude that the pronounced surface roughness observed in Fig. 3.8 and 3.9 is an artifact of an initially rough surface and a limited growth time. Therefore, if the lines in Fig. 3.8(a) and 3.9(a) are grown to much greater thicknesses, we should expect the surface roughness to be much smaller than that observed at short growth times. Figure 3.8(b) shows the result of the ELO growth of GaN from stripes aligned along [1$\bar{1}$00] direction for a growth time of 40 minutes (i.e., 33% longer growth times than that used to produce the islands shown in Fig. 3.8(a)). The resultant growth surfaces are clearly much smoother, with much flatter facets that those produced during the 30 minute growth experiment. This confirms the simulation results – rough growth surfaces are produced by initial surface roughness and short growth times.

One important mystery remains. What is the origin of the large initial line

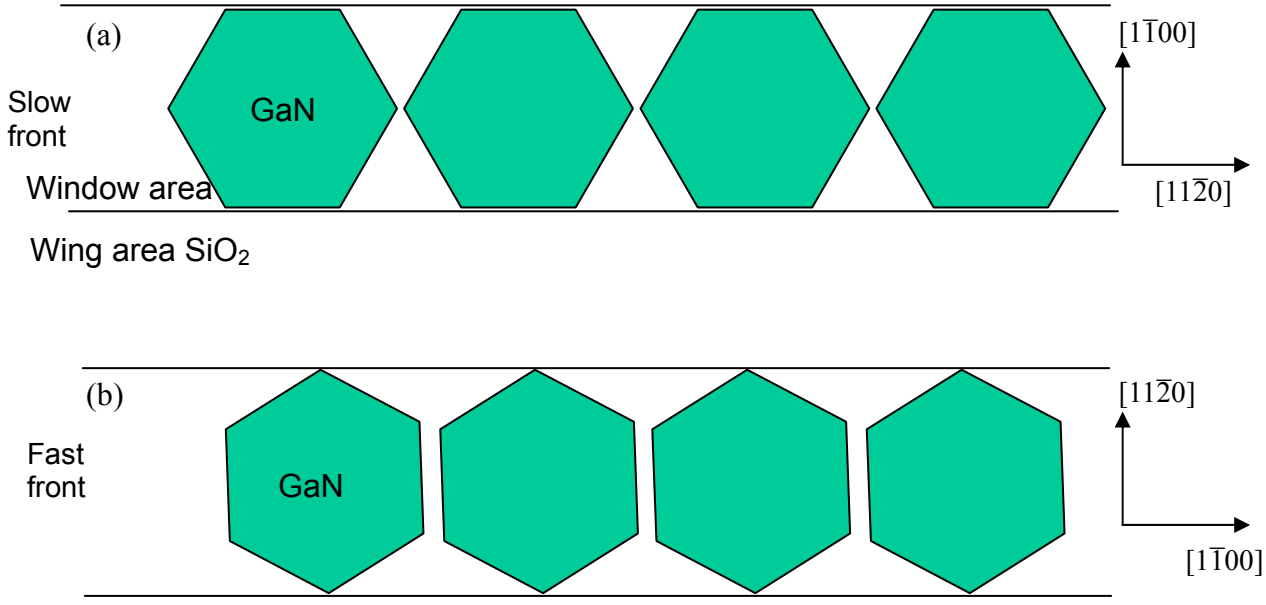

Fig.3.12 Illustration of the effect of the alignment of the stripe pattern and discrete island nucleation on the smoothness of the growth front. (a) Nucleation of GaN islands inside the stripe pattern aligned along the [11$\bar{2}$0] direction. The merging of these islands resulting in the formation of a slow growth front. (b) Nucleation of GaN islands inside the stripe pattern aligned along the [1$\bar{1}$00] direction. The merging of these islands results in the formation of a fast growth front. Black lines indicate the trench boundaries of the mask patterns. Hexagons indicate 2D projections of discretely nucleated GaN islands inside the window region. The normal of the edges of hexagons correspond to {1$\bar{1}$00} directions.

roughness that must have been present, but not directly observed? Scanning electron microscopy examination of the etched surfaces of the line patterns shows only a relatively small surface roughness. Therefore, the roughness observed at later times is not inherited from the etching process for the mask line pattern. In order to explain the relatively large initial roughness of the GaN line, we invoke an island nucleation model. When GaN deposition is resumed, GaN first grow within the etching-exposed window region. Observations of ELO in other systems suggest that when growth is resumed, it occurs through discrete island nucleation inside the window. Such GaN islands formed on the GaN substrate should be in the form of pyramidal polyhedra with $\{1\bar{1}01\}$ facets (for the present growth conditions). When these islands initially impinge on each other and grow into a continuous stripe, the stripe will have rough edges, as shown in Fig. 3.12.

Examination of the polygonal ring pattern in Figure 3.8(a) shows that the horizontal $\{11\bar{2}2\}$ (fast) exterior surfaces are much rougher than the vertical $\{1\bar{1}01\}$ (slow) exterior surfaces. What is the origin of this anisotropy in the surface roughness? Consider first the growth of a line with slow $\{1\bar{1}01\}$ exterior surfaces (i.e., the $[11\bar{2}0]$ oriented line – Fig. 3.12(a)). After a finite time, the corners will meet, as shown schematically in Fig. 3.13(a). Therefore, after a finite time, this surface will be flat. On the other hand, the tip corners of a line with fast $\{11\bar{2}2\}$ exterior surfaces (i.e., the $[1\bar{1}00]$ oriented line – Fig. 3.13(b)) move parallel to the growth direction and, hence, will never meet. This line should remain rough forever. This is not quite true, however, since the anisotropy in growth rates, discussed above, will eventually smooth any surface, no matter how rough it starts. However, such surfaces are only asymptotically smooth – i.e., it takes infinite time for such surfaces to become perfectly flat.

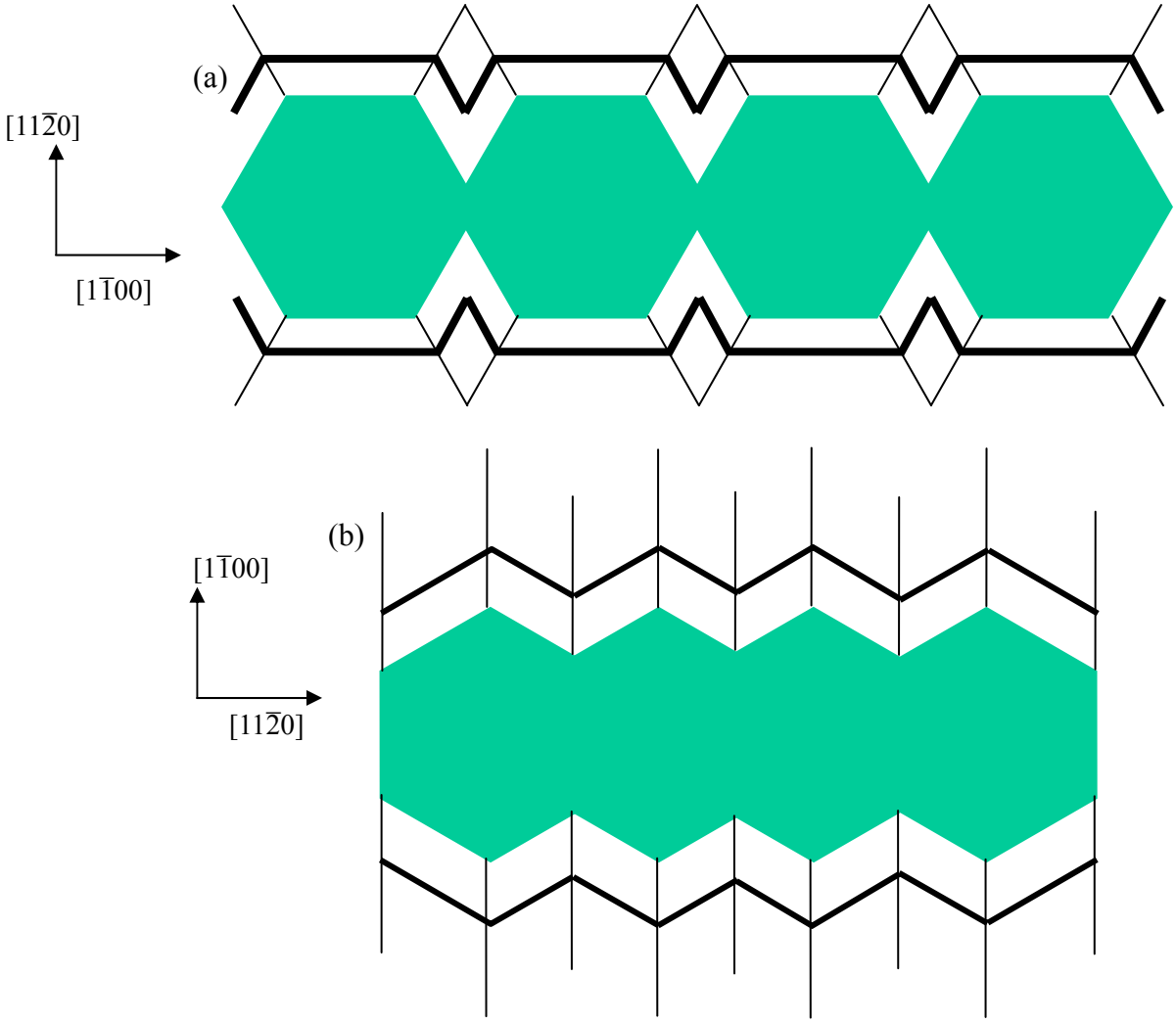

Fig. 3.13 Illustration of how the roughness evolves as the islands in the (a) [11$\bar{2}$0] and (b) [1$\bar{1}$00] oriented stripe pattern merge. The thick black lines represent the growth front at a later time and the thin black lines illustrate the paths followed by the convex corners.

The present analysis demonstrates, both experimentally and theoretically, that rough surfaces will become smoother with time during selected area growth at the begging of the ELO growth. The origin of the roughness in ELO is likely associated with island nucleation, growth and merging within the window region. The fact that some surface orientations are much rougher than others depends upon whether external corners meet during growth. This is determined by the orientation of the line relative to that of the crystal.

3.3.2 The merging behavior of GaN islands grown by ELO

In the ELO process, GaN layer will grow laterally on the mask layer. Eventually, these separated GaN layers will merge with each other and form a uniform thin film. Thus the merging behavior of GaN growth front is a key issue for the ELO technology which is used to achieve better crystal property. It is commonly observed that when ELO GaN crystals merge, additional defects are nucleated which are attributed to crystal tilt[28-30]. In this section, we study the merging of two crystals grown from two neighboring patterns and examine how the eventual shape develops.

In our experiments, an initial 2 μm thickness GaN layer was grown on a sapphire substrate and then coated with a 0.1 μm SiO_2 layer. The patterns were etched, exposing the underlying GaN. Upon further MOCVD growth, GaN growth proceeds first through the holes etched into the mask and then both vertically and laterally across the surface of the SiO_2 mask layer. The GaN was grown in the

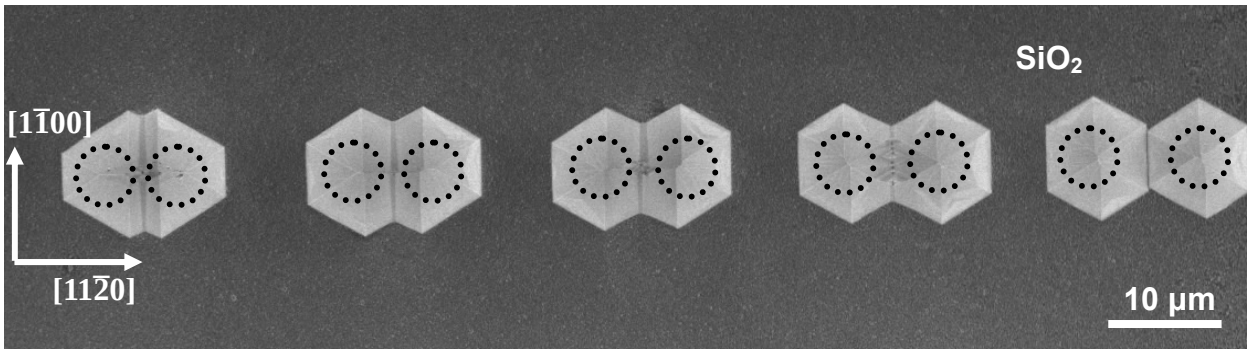

Fig. 3.14 The Experimental images of ELO GaN crystal growth morphologies of two merging crystals grown from two neighboring circular mask patterns with separations of 4 μm, 6 μm, 8 μm, 10 μm and 12 μm. The islands are pyramidal before merging and merge along a sharp edge. The dash line circle is the opening pattern wendow area.

EMCORE D180 MOCVD system. Trimethyl-metals and ammonia (NH_3) were used as precursors of Ga and N, respectively, with H_2 as carrier gas. The selective GaN layers were grown via controlling the growth temperature and the reactor pressure (preferably 950ºC and 500 Torr).

The growth takes place inside two 4 μm diameter circles (the different distance between two centers as 4 μm, 6 μm, 8 μm, 10 μm and 12 μm, as shown in Fig.3.14). This image shows that the islands growing from these circular windows form hexagonal pyramids prior to merging. The two islands form sharp edges when they merge, and there is no trend towards rounding at these edges. Eventually, two ELO GaN island merge and the fast growth facet between the two islands vanish, as shown with Fig. 3.14.

The individual morphology of each crystal island is consistent with the analysis based on Wulff construction [23, 24]. The ELO GaN island shape is dominated by the slow facets and constrained by the boundary conditions. However, the crystal merging behavior observed in Fig. 3.14 is a little surprising. According to the

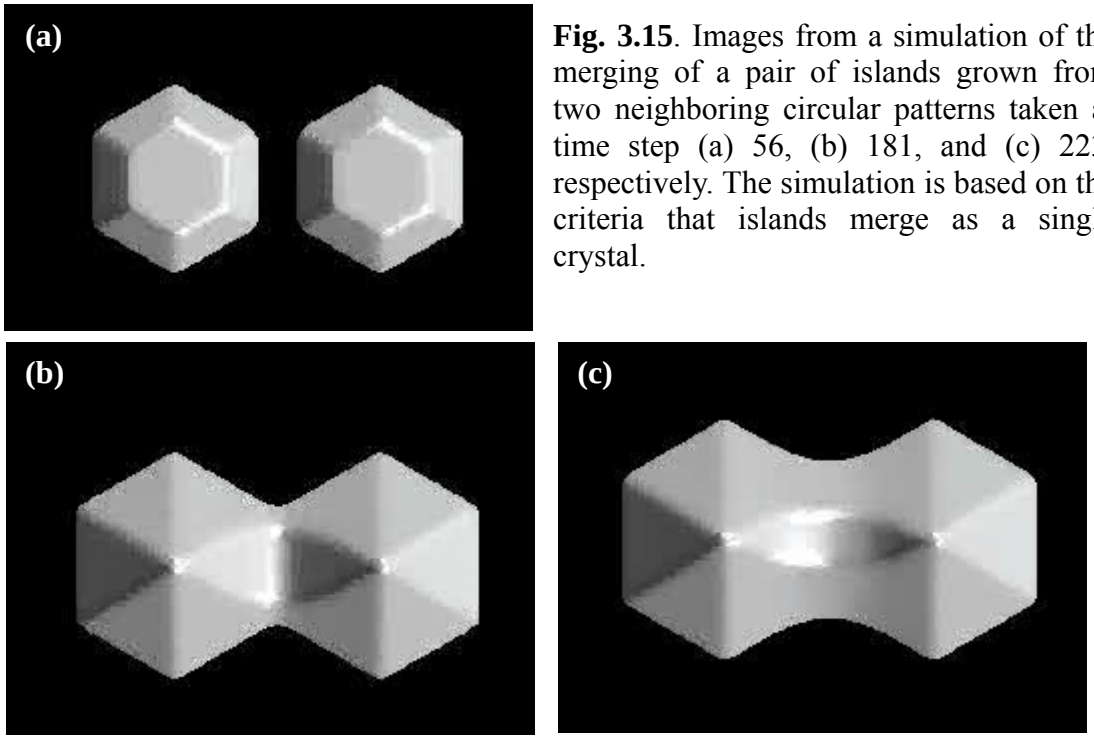

Fig. 3.15. Images from a simulation of the merging of a pair of islands grown from two neighboring circular patterns taken at time step (a) 56, (b) 181, and (c) 223, respectively. The simulation is based on the criteria that islands merge as a single crystal.

description of ELO GaN growth, although the islands are grown from different window region, they have the same crystallographic orientation (they grow from the same single crystal under the mask). Hence, ideally, these islands should merge like a single crystal.

According to the development of V-plot model [24], the level set simulations based on the circular mask patterns was carried out, as shown in Fig. 3.14. Note, the assumption that the two crystals merge as a single crystal is used. The simulation result, as shown in Fig. 3.15, shows two isolated islands before merging. The two islands have the same orientations and external facets. Fig. 3.15(b) and 3.15(c) show two islands merging. The region where the two islands merge is rounded, obviously, this conclusion contradicts with the experiments shown in Fig 3.15.

The discrepancy between the morphologies shown in Fig. 3.15 and those shown in Fig. 3.14 is due to the assumption that the two islands merge as if they were part of the same single crystal is not valid. This conclusion is also supported from the other groups' research works. For example Yoshiaki Honda *et.al.* found a big void formed when two separate ELO GaN stripe line emerge with each other [30]. X-ray diffraction further demonstrates that the crystal planes in the 'wings' (overgrown GaN) exhibit tilts away from those in the 'window' (seed) regions, in directions perpendicular to the stripe [1$\bar{1}$00] direction [28]. The tilt angle commonly range from 1 to 6 degrees depending on the mask pattern geometry.

In the following, we propose that the residual lattice mismatch strain could be the cause of the two islands starting with the same oritentations not to mergerge as single crystals and thus resulting in a tilt resperct to the (0001) direction. First, we re-examine the mismatch strain for GaN grown by ELO. The lattice mismatch between the GaN layer and underlying sapphire substrate leads to compressive

strains within the GaN layer [31-33]. The lattice mismatch can be understood through the epitaxial relationship [31]: $(0001)_{\text{Sapphire}}||(0001)_{\text{GaN}}$ and $[11\bar{2}0]_{\text{Sapphire}}||[1\bar{1}00]_{\text{GaN}}$. The lattice parameters are[32] $a_{\text{GaN}} = 3.189$ Å and $c_{\text{GaN}} = 5.185$ Å for GaN and $a_{\text{Sapphire}} = 4.758$ Å and $c_{\text{Sapphire}} = 12.991$ Å, respectively. Therefore, the GaN is rotated by 30° with respect to the substrate along the [0001] axis. Based on the epitaxial relationship, the biaxial mismatch strain inside the GaN thin film layer is $\varepsilon_0 = \dfrac{a_{\text{Sapphire}} - \sqrt{3}a_{\text{GaN}}}{\sqrt{3}a_{\text{GaN}}} = -0.14$. Such a large mismatch will cause interface dislocation nucleation to form to relax the mismatch strain. The magnitude of the critical thickness h_c can be approximated by [35, 36]

$$h_c = \frac{b}{|\varepsilon_0|}. \tag{3.10}$$

where $b = |\mathbf{b}|$, and the burgers vector **b** in our case is

$$\mathbf{b} = \frac{a_{\text{GaN}}}{3}\langle 11\bar{2}0\rangle. \tag{3.11}$$

Thus, the estimated critical thickness is $h_c = 2$ nm. The initial GaN thin film layer is about 2 μm thick, which is much larger than the critical thickness. Therefore, due to the nucleation and propagation of interface dislocations, the initial mismatch strain will be relaxed [35]. The amount of relaxation depends upon the interface dislocation spacing (or density). In the present case, the interface dislocations form a triangular network due to the three equivalent burgers vectors given in Eq. (3.11). Assuming the interface dislocation spacing is d, and then dislocations with the same burgers vector will result in a strain tensor $\dfrac{b}{d}\mathbf{n}_b \otimes \mathbf{n}_b$, where $\mathbf{n}_b$ is the unit vector parallel to the burgers vector. There are 3 equivalent types of dislocations as shown in Eq. (3.11). The sum of three equivalent arrays of

interface dislocations gives that

$$\Sigma_{i=1}^{3} \frac{b}{d} \mathbf{n}_b^{(i)} \otimes \mathbf{n}_b^{(i)} = \frac{3}{2} \frac{b}{d} \mathbf{1}_c \tag{3.12}$$

where $\mathbf{1}_c$ is the 2D identity tensor in the c-plane (basal plane). Hence, the interface dislocations result in an isotropic biaxial strain. Therefore the residual biaxial mismatch strain is

$$\varepsilon_r = \varepsilon_0 + \frac{3}{2} \frac{b}{d}. \tag{3.13}$$

Therefore, interface dislocations will reduce the compressive mismatch strain in the film layer. An accurate estimate of the dislocation spacing is rather difficult and requires the knowledge of dislocation kinetics (e.g., dislocation gliding activation energy, mobility, etc.) [35, 36]. Furthermore, due to the nature of the misfit dislocation and the mismatch strain, there were arguments that the misfit dislocations can only be nucleated and can not glide [37]. Qualitatively, the dislocation nucleation and propagation rate will slow down as the driving force is reduced due to the relaxation given in Eq. (3.13). Consequently, the relaxation rate will be very small as the film thickness approaches micron-scales. Therefore, in order to relax 95% of the mismatch strain, the thickness of the thin film layer has to be on the order of several hundred microns [32, 37]. Based on the experiments for other III-V semiconductor thin film growth [32, 37], it is reasonable to assume that the amount of unrelaxed mismatch

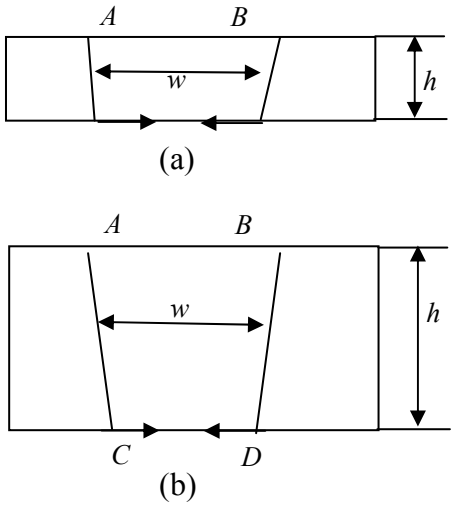

Fig. 3.16 Illustration of the residual strain induced bending of GaN grown by ELO above the windows region for a (a) large aspect ratio *w*/*h* and (b) small aspect ratio *w*/*h*.

strain at a thickness of several micrometers is on the order of 10%. The resulting residual strain is

$$\varepsilon_r = 0.1\varepsilon_0 = -0.016 . \qquad (3.14)$$

Now, we estimate the effect of the above residual mismatch strain on the wing tilt. In the windows region, the GaN crystal sustains almost the same residual strain as the underlying GaN layer beneath the mask layer. However, the surface of the overgrown crystal is traction free. Therefore the residual strain is relaxed for GaN crystal overgrown on the top of the mask region. This relaxation depends on the shape and size of the mask pattern. To be specific, we consider the stripe mask pattern. The effect of the residual strain on the wing tilt can be analyzed by studying the portion of GaN above the windows region as shown in Fig. 3.16.

There are two limiting cases. First, we consider the case that the height of the GaN crystal h above the mask layer is much smaller than the width w of the stripe pattern as shown in Fig. 3.16(a). The left and right boundary of the stripe pattern is labeled by 'A' and 'B', respectively. Due to the compressive residual strain indicated by the arrows at the bottom of the GaN above the window region, this part of GaN will bend such that the center of curvature is below the GaN. Since the aspect ratio is large, we assume that a major portion of the segment AB is under pure bending [38], i.e., the AB segment bends with a constant curvature κ.. Furthermore, the curvature and the residual strain are related by the following

$$\varepsilon_r = -\frac{\kappa h}{2} . \qquad (3.15)$$

On the other hand, due to the pure bending, the local crystallographic orientation will be tilted. If we define the tilt angle as the angle between the local [0001] direction and [0001] direction of the substrate, then due to symmetry with respect

to the center of AB segment, the center of the AB segment has tilt angle 0. Therefore, it follows that the tilt angles for both the left and right wings of the overgrown GaN is

$$\theta_u = \frac{\kappa w}{2}. \tag{3.16}$$

Combing Eq. (3.15) and (3.16), it follows that

$$\theta_u = -\frac{w}{h}\varepsilon_r. \tag{3.17}$$

If the aspect ratio of the AB segment is small, as shown in Fig. 3.16(b), then the AB segment is more rigid than a simple beam. The top surface of the AB segment will be almost strain free, due to the traction free boundary condition of the overgrown layer. On the other hand, the bottom of the AB segment is compressed.

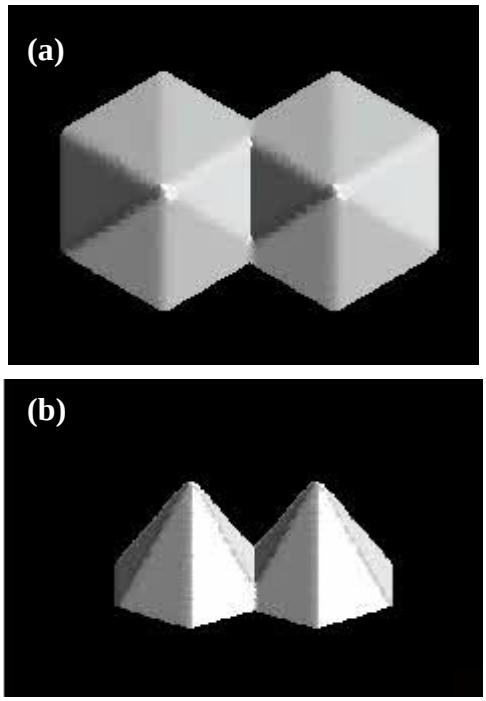

Fig. 3.17 Simulation of GaN grown by ELO using a circular pattern assuming the islands has slightly tilted in the c-direction. (a) shows a plan view, while (b) shows an oblique view.

Due to symmetry with respect to the center of the AB segment, the right end of the stripe pattern D is displaced to the left by

$$u = -\frac{w}{2}\varepsilon_r \quad . \tag{3.18}$$

Therefore, it follows that the tilt angles for both left and right wings of the overgrown GaN is

$$\theta_l = \frac{u}{h} = -\frac{w}{2h}\varepsilon_r. \tag{3.19}$$

Note, Eq. (3.17) gives an estimate for the upper bound of the tilt angle, while Eq.

(3.19) gives a lower bound estimate. The real tilt angle value is between these two bounds. The lower and the upper bound estimates only differ by a factor of 2.

The above analysis can be applied to estimate the wing tilt. An example, where large $\frac{w}{h} = 5.33$, is taken from Ref. [4]. In this case, the tilt angle will be close to the upper bound value given by Eq. (3.17). Using the value of residual strain in Eq. (3.14), we predict that the tilt angle is around $\theta = 4.8^{\circ}$. This is quite close to the measured value $\theta = 4.2^{\circ}$ measured by X-ray rocking curves [28] obtained for the sample reported in the Ref. [4]. A major source of error comes from the estimate of the residual strain. Actually, based on the measured tilt angle, we can estimate the interface dislocation density/spacing using Eq. (3.13) and Eq. (3.17) for the above large aspect ratio case. The estimated dislocation spacing is $d = 33\,\mathring{\mathrm{A}}$, which the burgers vector is about 10 times. The estimated residual strain based on Eq. (3.17) is $\varepsilon_r = -0.0137$.

It is noteworthy that, although the tilt angle is induced by elastic rotation, both bounds are independent of the elastic properties of GaN, they only depend on the residual strain and the aspect ratio. Therefore, the conclusions are applicable to other materials and other growth conditions. In the experiments shown in Fig. 3.14, the growth condition is different. Therefore, we do not observe vertical side facets. Furthermore, the mask pattern is different from the stripe pattern. Therefore, the crystallographic tilt will be smaller, and will be close to the lower bound given by Eq. (3.19) as a result of the small aspect ratio. However, a slight tilt is enough to cause imperfect growth. As a consequence of the crystallographic tilt, when two islands meet, there will be a slight misorientation. This results in a low angle grain boundary. Hence, we expect a low angle grain boundary to form where the

islands merge.

The simulation result is shown in Fig. 3.17. Comparing this with Fig. 3.14(a), it can be observed that the simulation correctly captures the sharp merging interface. The simulation, therefore, also supports the idea that crystal merging is almost always imperfect due to slight misorientations. The results also further demonstrate the power of our systematic approach to predict crystal growth morphology.

Finally, our analysis provides possible improvements to growth strategies. Based on the estimation of the tilt angle given in Eq. (3.17) and (3.19) and our estimate of the residual strain, shown in Eq. (3.13), we can see that in order to reduce the difference in orientations upon merging, a thicker film is preferred with the lower residual strain. Furthermore, window patterns and growth conditions which result in smaller island aspect ratios above the window region will be preferred. Therefore, for fixed growth condition, the preferred strategy is to use narrow windows pattern and thicker buffer layers.

3.4 Chapter Summary

In this chapter, the epitaxial lateral overgrowth by MOCVD of GaN was performed on the window stripe in the SiO_2 patterned mask. The ELO growth efficiency can be described by the growth parameters like growth temperature or fill factor. With the simple model that developed by using the boundary layers, the cross section area of the ELO GaN is understoodable. Such results will be useful for the future design of the ELO GaN material growth.

For a strip along the $<1\bar{1}00>$ direction, the ELO GaN edge is not straight when growth time is shorter, but smooth with longer growth time. This phenomenon can

be explained using simuation method developed by Dr. DanXu Du and Prof. David Srolovitz. It is demonstrated that the kinetic perturbations on the crystal islands are transient in nature. The conclusion guides future experiments to verify the transient nature of the perturbations by prolong the growth time.

We also study the merging behavior of GaN micro islands grown on the same substrate during epitaxial lateral overgrowth. The 3D crystal growth simulation model developed showed that islands with the same epitaxial relationship do not merge to form a single crystal due to the strain in them. Furthermore, a mismatch relaxation strain was used to explain the wing tilt which causes the non-ideal merging behavior. These results suggest that large aspect ratio (width to height) of the crystal above windows region in ELO is preferred to obtain high quality crystals.

The InGaN/GaN and AlGaN/GaN quantum well structures grown on the ELO GaN templates will be describe in the following chapter.

Reference:

[1] J. Park, P.A. Grudowski, C.J. Eiting, and R.D. Dupuis, "Selective-area and lateral epitaxial overgrowth of III–N materials by metal organic chemical vapor deposition" Appl. Phys. Lett. **73**, 333 (1998).

[2] O.-H. Nam, T.S. Zheleva, M.D. Bremser, and R.F. Davis, "Lateral epitaxial overgrowth of GaN films on SiO_2 areas via metalorganic vapor phase epitaxy" J. Electron. Mater. **27**, 233 (1998).

[3] K. Tadatomo, Y. Ohuchi, H. Okagawa, H. Itoh, H. Miyake, and K. Hiramatsu, "Hydrogen and Nitrogen Ambient Effects on Epitaxial Lateral Overgrowth (ELO) of GaN Via MOVPE" MRS Internet J. Nitride Semicond. Res. **4S1**, G3.1 (1999).

[4] H. Marchand, J.P. Ibbetson, P.T. Fini, X.H. Wu, S. Keller, S.P. DenBaars, J.S. Speck, and U.K. Mishra, "Fast Lateral Epitaxial Overgrowth of Gallium Nitride by Metalorganic Chemical Vapor Deposition Using a Two-Step Process" MRS Internet J. Nitride Semicond. Res. **4S1**, G4.5 (1999).

[5] K. Hiramatsu, K. Nishiyama, A. Motogaito, H. Miyake, Y. Iyechika, and T. Maeda, "Recent Progress in Selective Area Growth and Epitaxial Lateral Overgrowth of III-Nitrides: Effects of Reactor Pressure in MOVPE Growth" Phys. Stat. Sol. (a) **176**, 535 (1999).

[6] D. Kapolnek, S. Keller, R. Vetury, R.D. Underwood, P. Kozodoy, S.P. Denbaars, and U.K. Mishra, "Anisotropic epitaxial lateral growth in GaN selective area epitaxy" Appl. Phys. Lett. **71**, 1204 (1997).

[7] O.-H. Nam, M.D. Bremser, B.L. Ward, R.J. Nemanich, and R.F. Davis, "Growth of GaN and Al0.2Ga0.8N on Patterened Substrates via Organometallic Vapor Phase Epitaxy" Jpn. J. Appl. Phys. **36**, L532 (1997).

[8] Zhonghai Yu, M.A.L. Johnson, J.D. Brown, N.A. El-Masry, J.F. Muth, J.W. Cook, Jr., J.F. Schetzina, K.W. Haberern, H.S. Kong, and J.A. Edmond, MRS "Epitaxial Lateral Overgrowth of GaN on SiC and Sapphire Substrates" Internet J. Nitride Semicond. Res. **4S1**, G4.3 (1999).

[9] M.E. Coltrin, Ch.C. Willan, M.E. Bartram, Jung Han, N. Missert, M.H. Crawford, and A.G.Baca, "Transport, Growth Mechanisms, and Material Quality in GaN Epitaxial Lateral Overgrowth" MRS Internet J. Nitride Semicond. Res. **4S1**, G6.9 (1999).

[10] T. von Karman, "Uber laminare und turbulente Reibung" Math. Mech. **1,** 233 (1921).

[11] E.M. Sparrow, J.L. Gregg, "Nearly Quasi-Steady Free Convection Heat Transfer in Gases" J. Heat Transfer. Trans ASME **82**, 185 (1960).

[12] D.R. Olander, "Heat transfer" J. Heat Transfer. Trans. ASME **84**, 185 (1962).

[13] D.R. Olander, "Surface Chemical Kinetics and Gas-Phase Diffusion in Germanium-Iodine Reaction" Ind. Eng. Chem. Fundam. **6**, 178 (1967).

[14] R. Pollard, J. Newman, "Silicon Deposition on a Rotating Disk" J. Electrochem. Soc. **127**, 744 (1980).

[15] W.G. Breiland, G.H. Evans, "Design and Verification of Nearly Ideal Flow and Heat Transfer in a Rotating Disk Chemical Vapor Deposition Reactor" J. Electrochem. Soc. **138**, 1806 (1991).

[16] W. Breiland, M. Coltrin, J. Creighton, et al., "Organometallic vapor phase epitaxy (OMVPE)" Mat. Sci. Eng. **R 24**, 241 (1999).

[17] G.H. Evans, R. Greif, "Effects of boundary conditions on the flow and heat transfer in a rotating disk chemical vapor deposition reactor" Numer. Heat Transfer **12**, 243 (1987).

[18] G.H. Evans, R. Greif, "Second-law-based thermoeconomic optimization of two-phase heat exchangers" J. Heat Transfer **109**, 928 (1987).

[19] D. J. Srolovitz, "On the stability of surfaces of stressed solids" Acta Metall. Mater. **37**, 621 (1989).

[21] R. J. Asaro and W. A. Tiller, "Interface morphology development during stress corrosion cracking PT.1. Via surface diffusion" Metall. Trans. **3**, 1789 (1972).

[22] Z. Suo and J. Liang, "Theory of lithographically-induced self-assembly" Appl. Phys. Lett. **78**, 3971 (2001).

[22] D. X. Du and D. Srolovitz, "Electrostatic field-induced surface instability" Appl. Phys. Lett. **85**, 4917 (2004).

[23] D. X. Du, D. J. Srolovitz, M. E. Coltrin, and C. C. Mitchell, "Systematic Prediction of Kinetically Limited Crystal Growth Morphologies" Phys. Rev. Lett. **95**, 155503 (2005).

[24] D. X. Du and D. J. Srolovitz, J. Cryst. Growth (In Press).

[25] D. X. Du, Ph.D Thesis "Modeling and Simulation of Faceted Thin Film Crystal Growth", Princeton University (2006)

[26] A. P. Sutton and R. W. Balluffi, *Interfaces in crystalline materials* (Clarendon Press; Oxford University, Oxford, New York, 1995).

[27] P. Fini, H. Marchand, J. Ibbetson, et al., "Determination of tilt in the lateral epitaxial overgrowth of GaN using X-ray diffraction" J. Cryst. Growth **209**, 581 (2000).

[28] Z. Zytkiewicz, J. Domagala, and D. Dobosz, "Control of adhesion to the mask of epitaxial laterally overgrown GaAs layers" J. Appl. Phys. **90**, 6140 (2001).

[29] A. E. Romanov, P. Fini, and J. S. Speck, "Modeling the extended defect

evolution in lateral epitaxial overgrowth of GaN: Subgrain stability" J. Appl. Phys. **93**, 106 (2003).

[30] Y. Honda, Y. Iyechika, T. Maeda, H. Miyake and K. Hiramatsu. "Transmission Electron Microscopy Investigation of Dislocations in GaN Layer Grown by Facet-Controlled Epitaxial Lateral Overgrowth" Jpn. J. Appl. Phys. Part 2, **40,** L309 (2001).

[31] P. Ruterana and G. Nouet, "Atomic Structure of Extended Defects in Wurtzite GaN Epitaxial Layers" Phys. Status Solidi (b) **227**, 177 (2001).

[32] B. Skromme, H. Zhao, D. Wang, et al., "Strain determination in heteroepitaxial GaN" Appl. Phys. Lett. **71**, 829 (1997).

[33] M. Leszczynski, H. Teisseyre, T. Suski, et al., "Lattice parameters of gallium nitride" Appl. Phys. Lett. **69**, 73 (1996).

[34] L. B. Freund, "The driving force for glide of a threading dislocation in a strained epitaxial layer on a substrate" J. Mech. Phys. Solids **38**, 657 (1990).

[35] L. Freund, "Ion-Assisted Surface Processing of Electronic Materials" MRS BULL **17**, 52 (1992).

[36] R. Beresford, C. Lynch, and E. Chason, "Kinetics of dislocation-mediated strain relaxation in InGaAs/GaAs heteroepitaxy" J. Cryst. Growth **251**, 106 (2003).

[37] A. Bourret, C. Adelmann, B. Daudin, et al., "Strain relaxation in (0001) AlN/GaN heterostructures" Phys. Rev. B **63,** 245307 (2001).

[38] S. Timoshenko and S. Woinowsky-Krieger, *Theory of plates and shells* (McGraw-Hill, New York, 1959).

Chapter 4

Structure and optical characterization of nitride materials grown on the FACELO GaN templates

4.1 Introduction

In Chapter 3, the ELO GaN growth kinetics and the crystal morphologies were investigated. All these studies are aimed at obtaining nitride materials for using in the lighting emitting diodes (LEDs), laser diodes (LDs), detectors, solar cells, etc. Higher performance optical electronic device is required with higher crystal property and lower dislocation density. The ELO technology can be used to significantly reduce the dislocation density of the GaN thin films. At the same time, the ELO GaN morphology can be changed from the $\{11\bar{2}2\}$ facets to the $\{11\,\bar{2}\,0\}$ facets with variation of the growth parameteris [1-3] (i.e. growth temperature and pressure). The $\{11\bar{2}2\}$ semi-polar surface or the $\{11\bar{2}0\}$ non-polar surface provide a new templates for making new device structures.

The performance of nitride based optical devices can be improved, if their designs overcome two main issues. First, there is a high dislocation density of about 10^9 to 10^{10} cm^{-2} in GaN grown on traditional substrates like Al_2O_3 (sapphire) because of the large lattice mismatch. Possible solutions are to use better matching substrates like GaN, SiC or AlN, [4] which are usually more expensive. Second, when GaN growth surface is the (0001) plane, planar strain induced by the different lattice constants of the GaN quantum wells and the AlGaN barrier layers gives rise to

strong internal piezoelectric fields and spontaneous polarization field. [4] This leads to a local separation of electrons and holes in these quantum wells, poor overlap of electron and hole wave functions, long radiative lifetimes [5] resulting in a low internal quantum efficiencies [6]. Reduction of electrostatic fields is possible by growing the structures on non-polar or semi-polar plane of sapphire, e.g. on *r*-plane [7], where GaN grows on the $(11\bar{2}0)$ direction. Other approaches make use of more exotic substrates such as $LiAlO_2$ [8], on which pure *m*-plane GaN $(1\bar{1}00)$ growth was achieved. A technique, which can help to overcome both problems, is FACELO. It is realized by starting the epitaxial growth on (0001) plane and tuning the growth conditions to develop other facets, e.g. $(1\bar{1}01)$ and $(11\bar{2}2)$, on ELO stripes [9, 10]. Recently, K. Nishizuka *et.al* [11], F. A. Ponce *et.al* [12] and Barbara Neubert *et.al* [13] used FACELO GaN as a substrate successfully grown InGaN/GaN MQWs with a reduced piezoelectric field.

In this chapter, we mainly investigate the structural and optical property of AlGaN/GaN and InGaN/GaN quantum well structures grown on the FACELO GaN templates. In the following part, all the experiment were carried out on the stripe line patterned templates along the $<1\bar{1}00>$ direction.

4.2 AlGaN layer grown on FACELO GaN templates

AlGaN alloys have a wide band gap that ranges between 3.4eV and 6.2eV, thus they are of much interest for the development of ultraviolet light-emitting and detecting devices.[14, 15] But no suitable substrate available for growth of high quality AlGaN remains a issue for obtaining high performance device. With the FACELO GaN templates, we studied the structural and aluminum incorporation of

AlGaN layers grown on FACELO GaN/sapphire substrate. The ELO GaN structures were first grown on SiO_2-patterned GaN/sapphire (0001) templates by MOCVD. Then the $Al_xGa_{1-x}N$ alloy was grown simultaneously on the $(11\bar{2}2)$ facet ELO GaN and on (0001) facet GaN. Scanning electron microscopy (SEM), and secondary ion mass spectroscopy (SIMS) were used to characterize these structures. The comparision of the optical properties between the $(11\bar{2}2)$ and (0001)-faceted layers was characterized by the micro-photoluminescence (PL) measurements.

To prepare ELO GaN, a 2.0 μm thick GaN layer was first deposited on a *c*-plane sapphire substrate by MOCVD. Trimethyl-metals and ammonia (NH_3) were respectively used as precursors for group III and N, and H_2 was used as carrier gas. About 100 nm thick SiO_2 mask was patterned into stripes oriented in the $<1\bar{1}00>$ direction of GaN, defining a 4 μm wide opening with a period of 13 μm. After 30 mins of regrowth on these templates, ELO GaN with a triangular ridges crossection of $\{11\bar{2}2\}$ facets formed. The growth temperature was 950°C and reactor pressure was 500 Torr. Then the AlGaN layer was deposited simultaneously on the two different templates at 1000 ºC. Sample A was grown on the ELO GaN template while sample B was grown on the reference c-plane GaN template. The target aluminum composition in the reference sample was 10%.

The morphology and cross-sections of the as grown layers were studied with a JEOL 6700 SEM. Aluminum composition of the epitaxial layers was measured using secondary ion mass spectrometry (SIMS) in ToF-SIMS-IV instrument. The depth profiles were obtained using 3 keV Ar^+ beam for sputtering and 25 keV $^{69}Ga^+$ beam for mass analysis, both at 45 º incidences. Focusing of the analysis beam provided lateral resolution better than 1 μm. The PL spectra were recorded

at room temperature using a 325 nm excitation line with a lateral resolution of 2 μm (Renishaw 2000 set up).

The original serrated ELO GaN stripe has a height of 5 μm and a width of 6 μm is shown in Fig. 4.1 and the {11$\bar{2}$2} sidewall facets are clearly displayed. It is known that the morphology of ELO GaN varies with the different growth conditions and result obtained is similar to those reported by K.Hiramatsu *et.al.* [16].

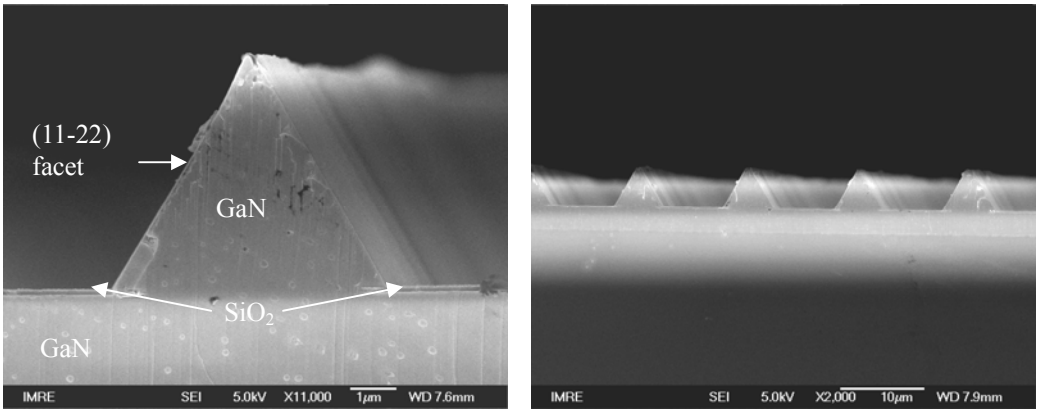

Fig. 4.1. Cross-sectional SEM images of the ELO GaN sample grown for 30 mins along the $<1\bar{1}01>_{GaN}$ direction.

4.2.1 AlGaN layer growth on two different templates

Fig. 4.2 (a) and (b) show the cross-sectional SEM images of AlGaN layer grown simultaneously on the two different templates. Fig. 4.2(a) is the ELO GaN with the (11$\bar{2}$2) facet and Fig. 4.2(b) is the c-plane GaN with the (0001) facet. In Fig. 4.2, about 300 nm AlGaN layer is grown on the 5 μm high and 6 μm wide triangular shaped ELO GaN surface. Under the same growth condition, about 300 nm AlGaN layer was grown on the c-plane GaN surface. On the SiO_2 mask, it was found that the polycrystalline AlGaN layer was deposited because of the strong cohesive force between Al and SiO_2. [17, 26] Otherwise GaN can't be deposited on the SiO_2 mask. Fig. 4.2(c) and 4.2(d) show the cross-sectional and top view of

SEM images of about 100 nm polycrystalline AlGaN deposited on the SiO_2.

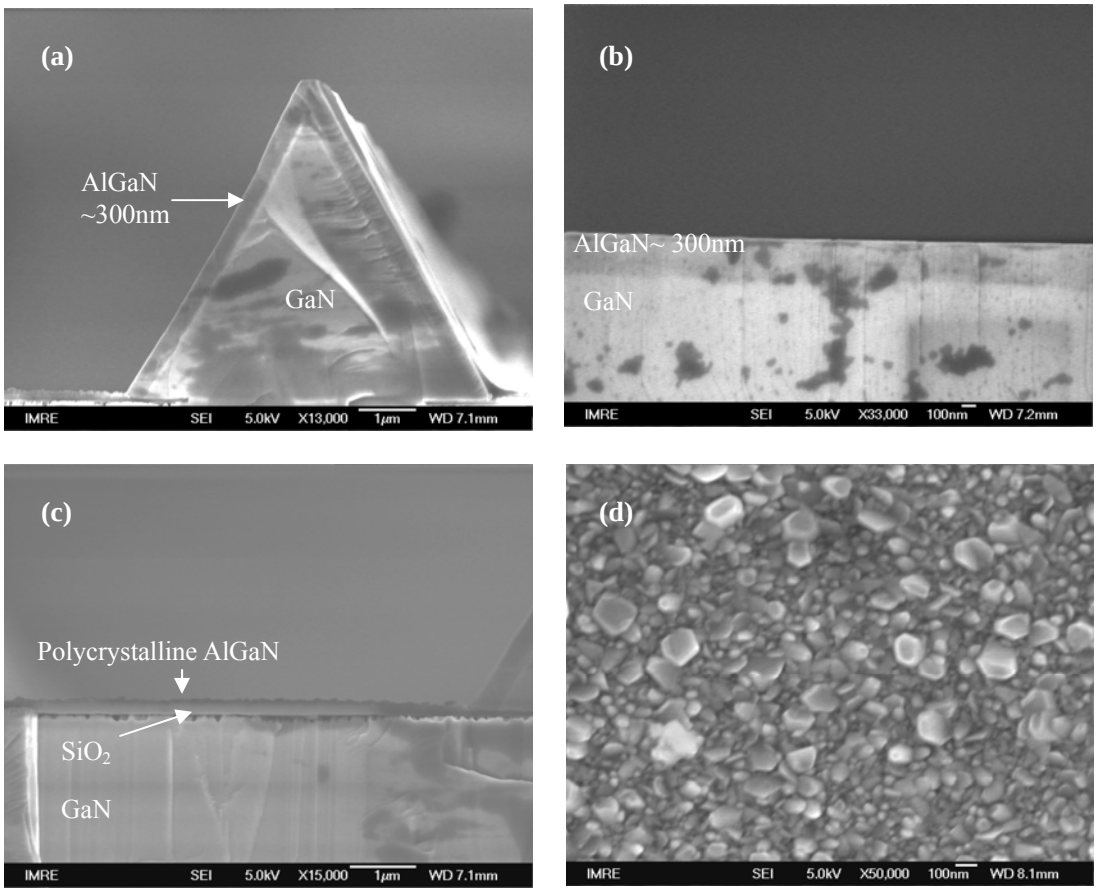

Fig. 4.2. Cross-sectional SEM images of AlGaN deposited on the ELO GaN template (a); GaN grown on the c-plane GaN template, simultaneously (b); the cross-sectional (c) and top view SEM images (d) of polycrystalline AlGaN deposited on the SiO_2 mask, respectively.

4.2.2 Al content variation analysis by the μ-PL, SIMS.

A cross-section diagram of the AlGaN grown on ELO GaN microstructure is shown in the Fig. 4.3(a). The triangular ELO AlGaN base is about 6.4 μm wide, and the SiO_2 surface width between two ridges is about 6.6 μm. The micro-PL spectrum was taken at three different positions, A, B, C as shown in the Fig. 4.3(a). The micro-PL spectra taken at point A to C shows that the aluminum incorporation dependence on the orientation of the growth plane. At the ELO AlGaN point A,

the micro-PL spectrum shows a peak wavelength of 352.8 nm corresponding to the aluminum compositions of 6%. The content of Al was calculated from the compositional dependence of the energy band gap of the ternary alloys:

$$E_{gAlGaN}(x) = E_{gGaN} \cdot (1-x) + E_{gAlN} \cdot (x) - b \cdot x \cdot (1-x) \quad (4.1)$$

In this equation, E_g, x and b are the band gap, AlN molar fraction and bowing

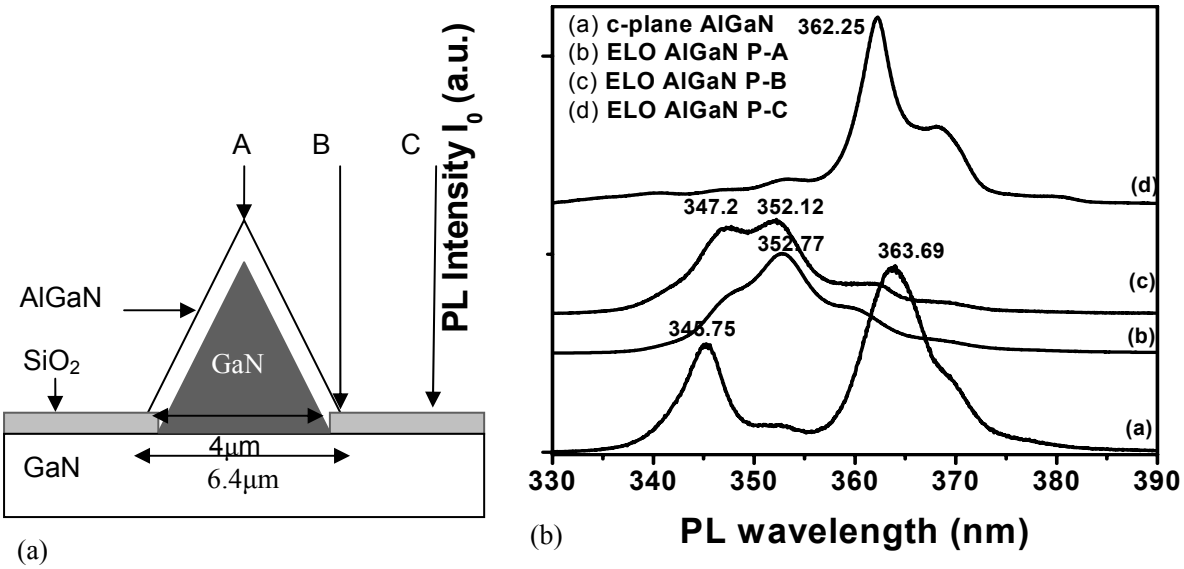

Fig. 4.3. (a) Cross-sectional structure of ELO AlGaN and (b) the μ-PL spectrum taken on the ELO AlGaN and taken on the c-plane AlGaN at the wavelengths ranging from 330nm to 390nm. Three different positions (P-A, P-B, P-C) that are chosen for the measurement of PL as indicated in Fig. (a).

parameter, respectively. The value of E_{gGaN}, E_{gAlN} and b used were 3.4 eV, 6.2 eV and 1 eV [17]. At the edge (point B) between the ELO AlGaN base and polycrystalline AlGaN grain on the SiO_2 mask, two peaks with the wavelengths 347.2 nm and 352.1 nm are observed corresponding to aluminum compositions of 9% and 6%, respectively. On the SiO_2 mask, the PL signal comes from the underlying GaN, giving a peak at the 362.3 nm, a weak shoulder at about 347 nm is observed which should be induced by the polycrystalline AlGaN. For the reference planar epitaxy, the μ-PL spectrum gives an AlGaN peak wavelength of 345.8 nm. So the *c*-plane AlGaN layer grown simultaneously could result in a

nominal aluminum composition about 9.5%. The PL light emission from the center of these triangular-shaped regions (A) observed at longer wavelength (352.8 nm) compared to that excited from the c-plane AlGaN (345.8 nm), indicating a decrease in aluminum incorporation. The PL peak intensity from the point A is half that from the C. This is mainly attributed to the laser reflection on the $(11\bar{2}2)$ facet.

To determine the Al composition in the AlGaN layers, SIMS depth profiling was carried out. During the acquisition of SIMS data, each secondary ion reaching the

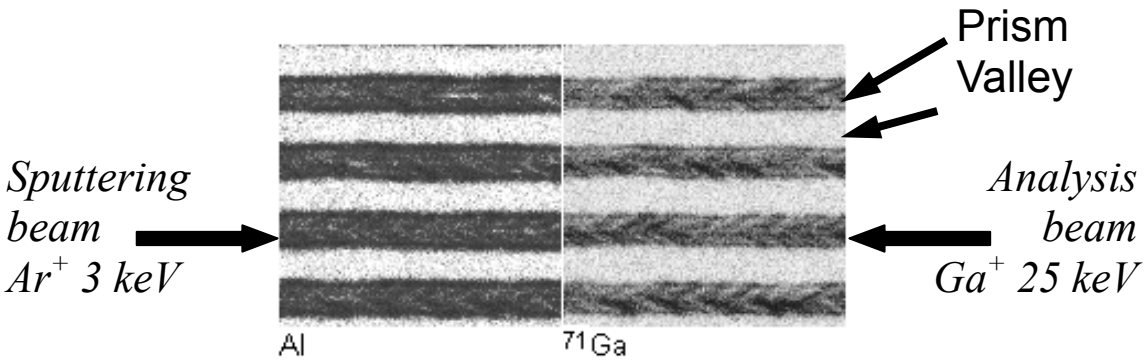

Fig. 4.4. Mass-resolved images of Al and Ga in ELO AlGaN sample and beam directions is along the $<1\bar{1}00>_{GaN}$ direction; scan size 50 μm, lateral resolution 0.5 μm.

detector is stored in a raw data file. From this file, it is possible to reconstruct the mass spectra, depth profiles, or mass-resolved images (chemical maps) as shown in Fig. 4.4. The chemical maps show ions of particular mass originating from the scanned pixels, where white region corresponds to higher and dark region to lower intensity. On the maps of both Al and Ga, shown in Fig. 4.4, the *c*-plane facets appear as bright and ELO prisms as dark. This is due to the decrease of sputtering yield at glancing angles and curvature of electric field accelerating secondary ions from the inclined surfaces. From converting the ratio of Al to ^{71}Ga SIMS

intensities to the concentration of aliuminum, then the depth profile of the Al incorporation was ploted, as shown in Fig. 4.5, the AlGaN grown on *c*-GaN/sapphire (0001) was used as a reference sample. The depth profiles shown in Fig. 4.5 were reconstructed on selected areas of the scan corresponding to the valley (dashed line) and prism regions (solid line). The average content of Al around 6% on $(11\bar{2}2)$ facets can be found in the Fig. 4.5. It also shows that the polycrystalline AlGaN on the SiO_2 layer has higher Al composition (about 12%) than the $(11\bar{2}2)$ facet AlGaN layers. From Fig. 4.5, it is also seen that the higher Al content polycrystalline AlGaN will grown on the SiO_2 first, then the Al concentration will decrease with increasing of the thickness of the AlGaN layers.

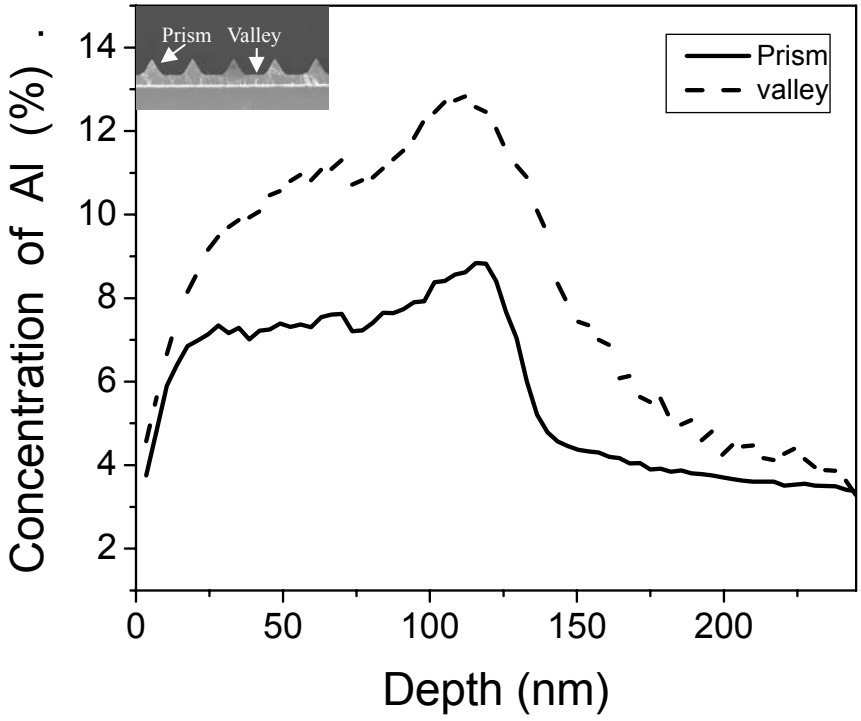

Fig. 4.5. Aluminum concentration of the ELO AlGaN sample with different locations (prism, valley) indicated by the SEM image.

From the PL and SIMS results, it is concluded that in the growth of AlGaN the aluminum concentration shows a strong dependence of the growth plane

orientation. The (11$\bar{2}$2) surface has a lower number of coordinated surface atom bonds than those on (0001) surface [18]. For traditional semiconductors, surface atoms always prefer to attach at positions with the highest possible coordination number since they are positions of minimum energy. Thus the sticking coefficient of aluminum adatoms on the (0001) surface is higher resulting in a higher Al incorporation. On the other hand, the (11$\bar{2}$2) facet is at least partially relaxed, [12] whereas the AlGaN grown on the c-plane GaN will be under tensile strain. This strain factor if exists alone should result in lower Al incorporation on the c-plane GaN since the c-plane GaN has a higher a-lattice parameter than AlN, (3.189 Å versus 3.111 Å, respectively). Therefore, the larger Al incorporation on the c-plane GaN obtained from this experiment suggests that the higher sticking coefficient is the dominant factor in determining the Al incorporation on the c-plane GaN.

In summary, AlGaN layers is found to have lower Al incorporation on the (11$\bar{2}$2) facet compared to that on the (0001) facet. The variation of the aluminum compositions was observed by micro-PL and SIMS. The reasons for these results have been analyzed.

4.3 AlGaN/GaN multiple quantum wells grown on FACELO GaN templates

Semiconductors from GaN family, such as $In_xGa_{1-x}N$ and $Al_xGa_{1-x}N$, are widely used for light emitting devices (LED) in the green and blue spectral range. [14, 15] They make use of multiple quantum wells (MQW) to trap electrons and holes for their efficient recombination. With FACELO GaN templates, we could grow the quantum wells structures on both the (11$\bar{2}$2) and (0001) facets. It gives us a very good opportunity to compare the optical property between the two different facets.

4.3.1 Experimental Process

For all samples discussed in this section, the preparation of the FACELO GaN templates is same. First, a 2.0 μm thick GaN layer was first deposited on a *c*-plane sapphire substrate by MOCVD. Trimethyl-metals and ammonia (NH_3) were respectively used as precursors for group III and N, and H_2 was used as carrier gas. A 100 nm thick SiO_2 mask was patterned into stripes oriented in the $<1\bar{1}00>$ direction of GaN, defining a 4 μm wide opening with a period of 13μm, as shown in Fig. 4.3. After 30 mins of regrowth on these templates, ELO GaN with $\{11\bar{2}2\}$ facets were selectively overgrown, as shown in Fig. 4.6. The growth temperature was 950 ºC and reactor pressure was 500 Torr. After the SiO_2 mask was removed by HF solution, 10 periods of AlGaN/GaN MQWs were grown on the whole surface. The target Al composition in the barriers was 10%, with the TMGa flow rate of 12 sccm and the TMAl flow rate 20 sccm. The growth temperature was about 1000 ºC, the reactor pressure was kept at 80 Torr and the growth time of well and barriers was 12 s and 90 s, respectively. All samples were grown using a constant total flow of H_2 and N_2 carrier gases and the ratio of H_2/N_2 was constant.

4.3.2 Structure and Composition of MQWs

The morphology of FACELO GaN has the shape of a prism with a triangular cross-section, as seen from the SEM image in Fig. 4.6. The triangular cross-sections are about 5 μm high and 5.8 μm wide and the spacing between them is about 7.2 μm. The roughness of the $(11\bar{2}2)$ surface seen in Fig 4.6 is due to the short growth time of ELO GaN. The dark rectangular shaped holes at the base of

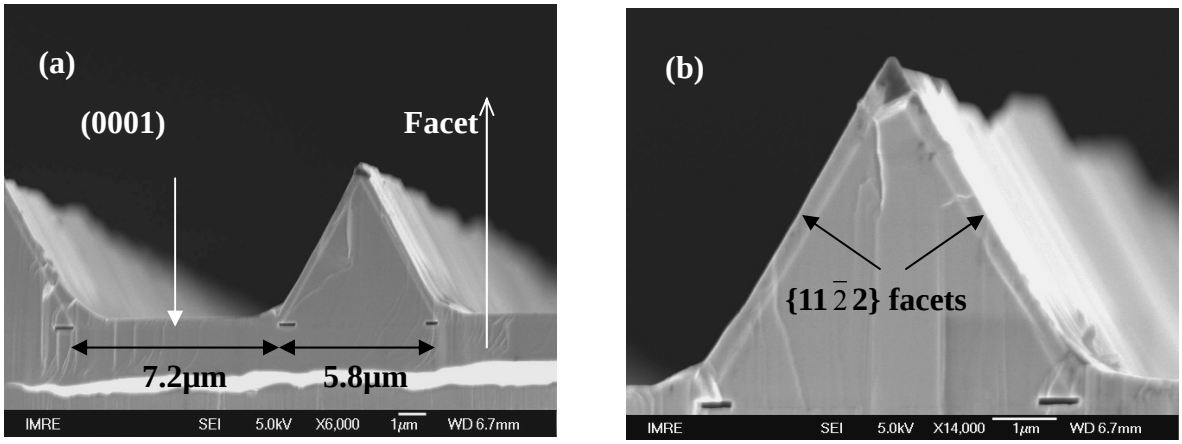

Fig. 4.6. Cross-sectional SEM of the AlGaN/GaN MQWs grown on FACELO GaN templates. $Al_{0.1}$GaN/GaN MQWs are SEM images from the same sample at different magnification (a) and (b).

the triangles of ELO GaN are the voids formed due to removal of SiO_2 mask. Fig. 4.7 shows the cross-sectional TEM images of the AlGaN/GaN MQWs grown simultaneously on the (11$\bar{2}$2) facets and on the *c*-planes. It is seen that the 10

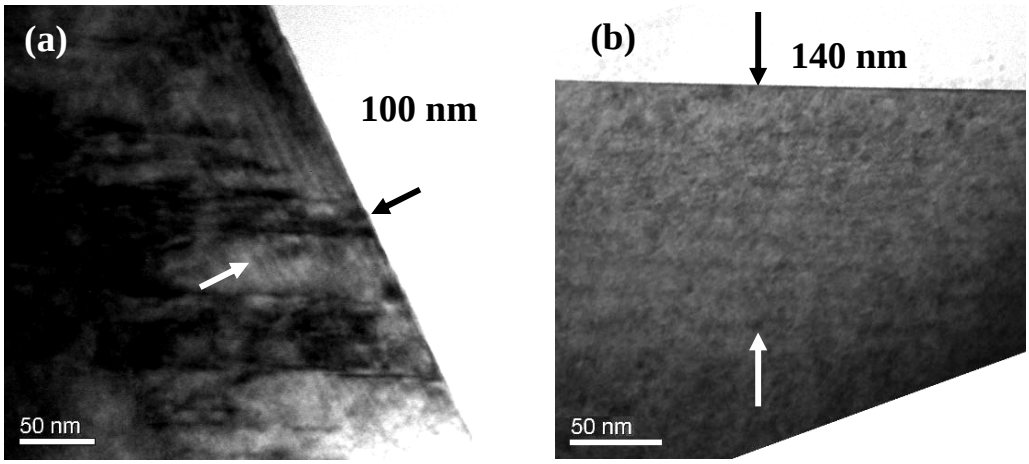

Fig. 4.7. The cross-sectional TEM images of the $Al_{0.1}$GaN/GaN MQWs (a) on the (11$\bar{2}$2) facet and (b) on the (0001) facets.

periods AlGaN/GaN MQWs are grown on the (11$\bar{2}$2) facet successfully with total thickness of approximately 100 nm. The *c*-plane or (0001)-oriented MQWs was also observed with total thickness 140 nm. The different growth rates of MQWs on these facets are evident from the structural analysis. The GaN growth rates are found higher along the *c*-direction than that along the (11$\bar{2}$2) facets. The high resolution-XRD was used to measure not only the thickness of MQWs well and barrier but also the aluminum content. The XRD profile of the AlGaN/GaN MQWs grown on the FACELO GaN templates (Fig. 4.8) was taken in the vicinity of the (0002) diffraction. Multiple satellite peaks were seen in Fig. 4.8, it indicate

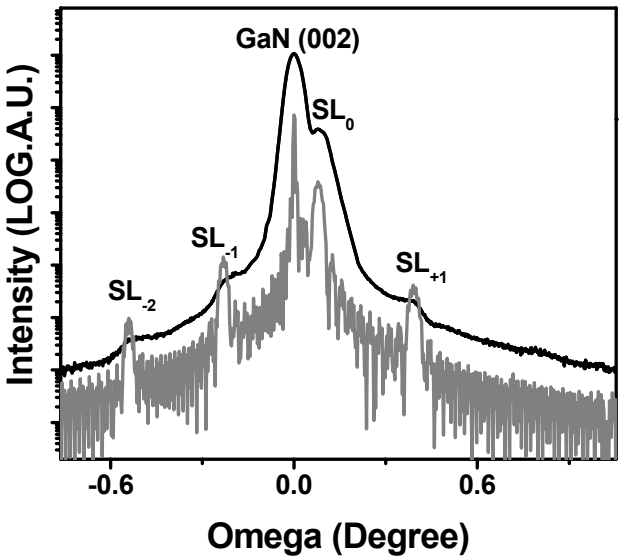

Fig. 4.8. High-resolution X-ray diffraction ω/2θ experimental (black line) and calculated (gray line) triple axis symmetrical scans near the (0002) GaN diffraction peak was taken on the AlGaN/GaN MQWs grown on the FACELO GaN templates.

that the presence of the MQWs growth on the FACELO GaN template. So we use these data to deduce both quantum well thickness and Al content of AlGaN/GaN MQWs on the *c*-plane. The Al content was found to be x=0.15, quantum well and barrier thickness were 6.3 nm and 8.5 nm, respectively. These results were

obtained by fitting the experimental spectra using the dynamical diffraction theory.

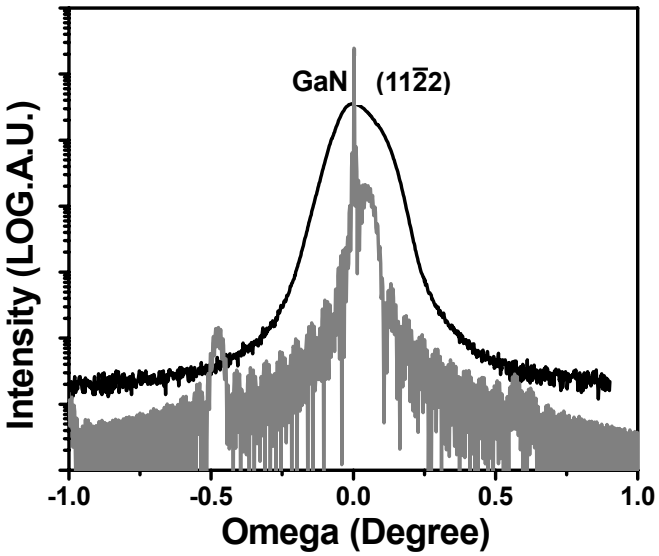

Fig. 4.9. High-resolution X-ray diffraction ω/2θ scans near the (11$\bar{2}$2) GaN diffraction peak was taken on the AlGaN/GaN MQWs grown on the FACELO GaN templates.

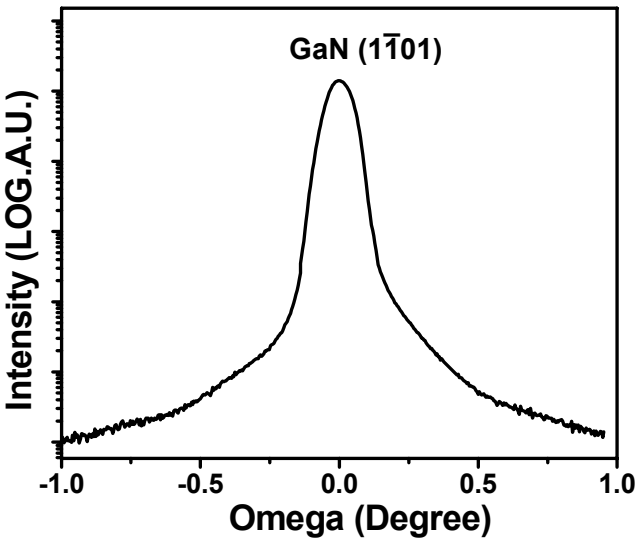

Fig. 4.10. High-resolution X-ray diffraction ω/2θ scans near the (1$\bar{1}$01) GaN diffraction peak was taken on $Al_{0.1}GaN$/GaN MQWs grown on the FACELO GaN templates.

The Al content deduced from the HR-XRD for $Al_{0.1}Ga_{0.9}N$/GaN MQWs compared to the SIMS results (Fig.4.11) indicate a higher Al content on the (0001) facet than on the (11$\bar{2}$2) facet. This result is consistent with the previous conclusion given in section 4.2 of the AlGaN layer grown on the FACELO GaN templates. The barrier and well thickness measured from XRD are consistant with the values obtained by TEM characterization. The HR-XRD was taken with the (1$\bar{1}$01) and (11$\bar{2}$2) diffraction as shown in Fig. 4.9 and Fig. 4.10, respectively. It is seen that for the XRD spectra at (11$\bar{2}$2) shows a presence of a shallow sholder indicating diffraction from MQWs.

If the ratio of the growth between AlGaN and GaN are the same for the (0001) and (11$\bar{2}$2) facets, then the thickness of the barrier and well can be deduced as listed in Table 4.1. Then we can just deduce the thickness of the barrier and well of the AlGaN/GaN MQWs on the both facets. The detailed numbers were list in the Table 4.1.

	$Al_{0.1}Ga_{0.9}N$ /GaN MQWs	
	well (nm)	barrier (nm)
(0001)	6.3	8.5
(11$\bar{2}$2)	4	6

Table 4.1. The thickness of the AlGaN/GaN MQWs well and barrier are obtained from simulation date by fitting the XRD curves.

The growth rate on the two facets is controlled by two competing factors. First: the (11$\bar{2}$2) surface has lower number of coordinated surface atom bonds than those on the (0001) surface [20]. For III-V semiconductors, surface atoms always prefer to attach at positions with the highest possible coordination number since they are positions of minimum energy. Thus, the sticking coefficient of Al and Ga adatoms on the (0001) surface is higher to result in a higher growth rate. Second: the (11$\bar{2}$2) facet morphology is different; it has more incorporation sites due to rougher surface related to presence of steps and kinks, which can increase the growth rate slightly. The results indicate that the dominant factor for the difference of the growth rates is the different coordination number of adatoms.

4.3.3 SIMS results for the AlGaN/GaN MQWs

To determine the Al composition in the AlGaN/GaN MQWs on the (11$\bar{2}$2) facets, SIMS depth profiling was carried out. During the acquisition of SIMS data, each secondary ion reaching the detector is stored in a raw data file. From this file, it is possible to reconstruct the mass spectra, depth profiles, or mass-resolved images (chemical maps) as shown in Fig. 4.11. The chemical maps show ions of particular

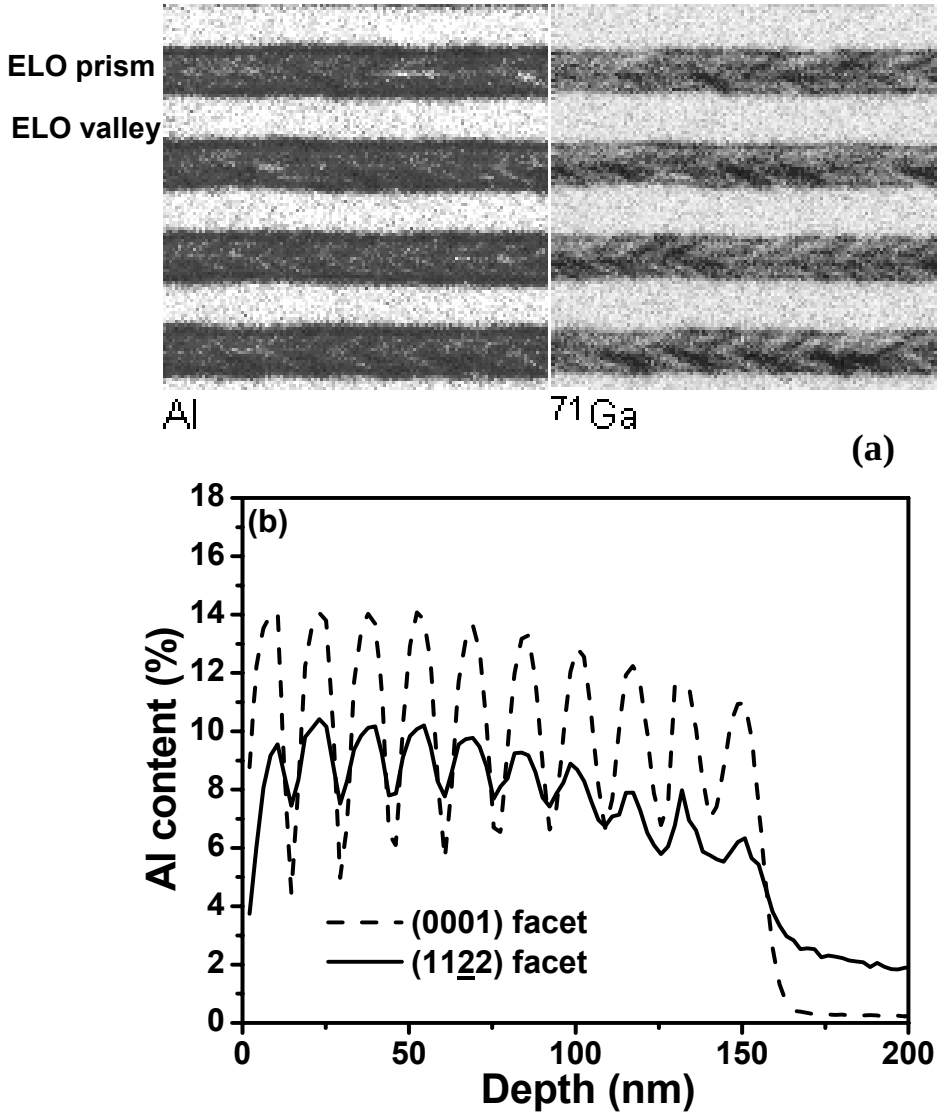

Fig. 4.11. SIMS results from $Al_{0.1}Ga_{0.9}N$ /GaN MQWs: (a) maps of Al and ^{71}Ga on four stripes, analysis area is 50 μm × 50 μm; (b) is depth profiles of Al concentration x=0.1 AlGaN/GaN MQWs of the two different facets.

mass originating from the scanned pixels, where white region corresponds to higher and dark region to lower intensity. On the maps of both Al and Ga, shown in Fig 4.11(a), the *c*-plane facets appear as bright and ELO prisms as dark. This is due to the decrease of sputtering yield at glancing angles and curvature of electric field accelerating secondary ions from the inclined surfaces. Typical chevron pattern on ELO is due to the roughness of $(11\bar{2}2)$ facets, which is also evident from Fig. 4.6. The depth profiles shown in Fig 4.11(b) was on selected areas of the scan corresponding to the *c*-plane (dashed line) and ELO regions (solid line) of the Al content of the AlGaN/GaN MQWs. Ten periods of the multiple quantum wells are seen on both areas. These results indicate that aluminium incorporation depends significantly on the surface orientation.

To convert the ratio of Al to SIMS intensities to the concentration of Al, a flat $Al_{0.1}Ga_{0.9}N$ layer on GaN/sapphire (0001) was used as a reference sample. As shown in Fig. 4.11 (b), the average content of Al is around 11% on both facets of the $Al_{0.1}Ga_{0.9}N$ /GaN MQWs, but the amplitude of the oscillations is different. On the flat *c*-plane MQWs, the contrast is determined by SIMS depth resolution, which is estimated to be around 3 nm. On the $(11\bar{2}2)$ facets, the contrast is lower due to the roughness of these facets, so that the rising and falling slopes of the chevrons are sputtered by Ar^+ beam with different rates. Thus, the oscillations decay faster than on *c*-plane and there is a tail of Al after MQWs. SIMS results confirm that Al incorporation occurs higher on the *c*-plane compard to the $(11\bar{2}2)$ facet and the incorporation is within 10% of accuracy.

4.3.4 Optical Properties of MQW

The optical properties of the AlGaN/GaN MQWs were investigated by micro-Raman scattering and cathodoluminescence (CL) spectroscopy. Raman scattering was used to examine the relaxation of compressive strain, which is due to the difference of thermal expansion and lattice constants of GaN and sapphire. Raman spectra of the samples recorded from different regions of the facets are

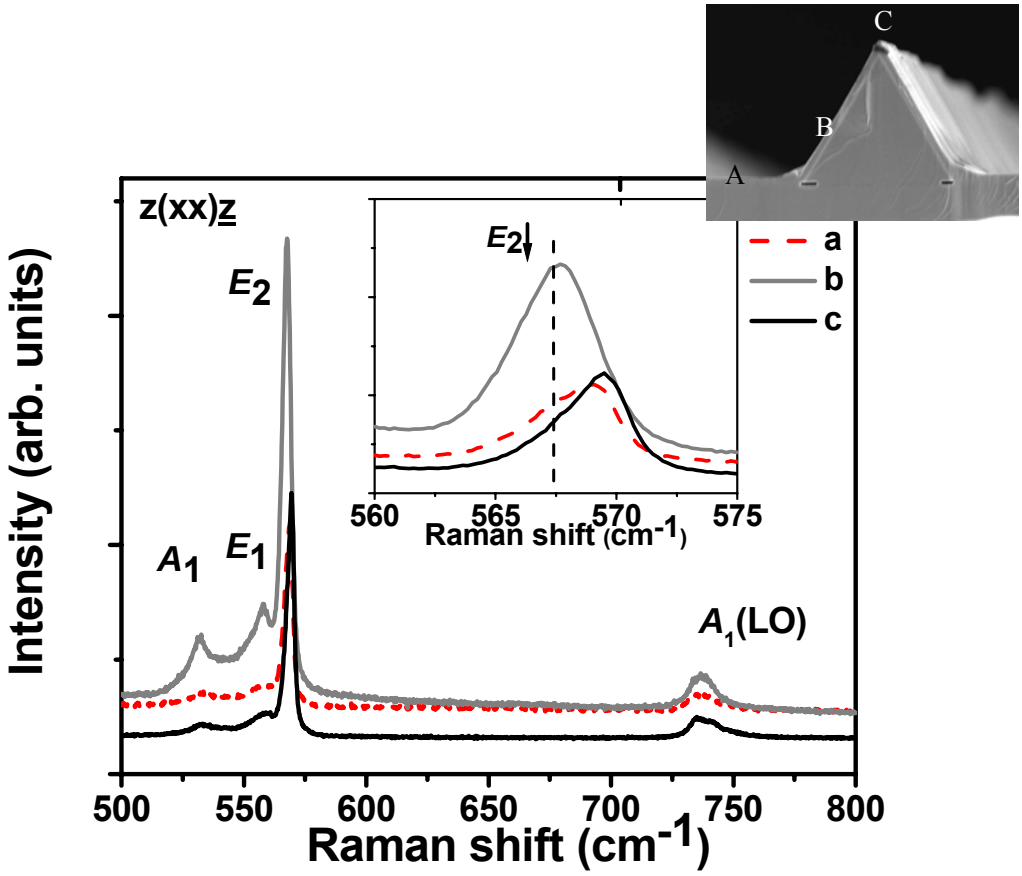

Fig. 4.12. Room temperature micro-Raman spectra recorded from the $Al_{0.1}Ga_{0.8}N$/GaN. The dashed line in the Fig 4.11 inset indicates the peak position recorded from the strain-free freestanding GaN.

shown in Fig 4.12. The shift of the the E_2-mode at different locations on the $(11\bar{2}2)$ facets indicate that the different amount of strain relaxation could be induced by the various location. The E_2-high mode in the Raman spectra was used to measure

the strain, because it has been proven particularly sensitive to the biaxial stress in GaN epitaxial layers [23]. Along the *c*-direction of the seed layer, the E_2-mode is shifted to higher frequencies with respect to the standard value of 567.5 cm^{-1} recorded from a 400 μm thick freestanding GaN substrate. The shift is about 2.0 ± 0.2 cm^{-1} on the seed layer GaN and only 0.4 ± 0.2 cm^{-1} on top of ELO GaN. Intermediate values were recorded along the (11 $\bar{2}$ 2) facets. Using the proportionality factor of 4.2 cm^{-1}/GPa for hexagonal GaN, [24] we obtain the values of residual stress 0.47 ± 0.05 GPa in the seed layer GaN and a stress variation of 0.09 to 0.17 GPa on the (11$\bar{2}$2) facet of the ELO GaN. Thus the average strain relaxation difference between the two facets is about 0.3 GPa.

In CL experiments, penetration depth of the excitation light depends on the electron energy used to activate the light emission. The Al composition, quantum well and barrier thicknesses, the strain relaxation, and the polar field were found different in these two MQWs structures on the (11$\bar{2}$2) and (0001) facet. The CL spectra were taken at 80K. In the CL image Fig 4.13, it is clearly shown that the emissions at 341 nm are coming from the AlGaN MQWs on the (11$\bar{2}$2) facet and that at 344 nm are coming from the AlGaN MQWs ont the (0001) facet. The CL spectra from the two different facets shown in Fig. 4.14, the peaks of the MQWs from both facets show a blue shift with respect to bulk GaN and the blue shift on the (11$\bar{2}$2) facet is 36 meV compare to that on the (0001) facets. Moreover, the MQWs peak intensity of the (11$\bar{2}$2) facet is significantly improved to the (0001) facets, which indicate that the better crystal propertry on the (11$\bar{2}$2) facet. The blue shift of these CL peaks can be caused by three factors.

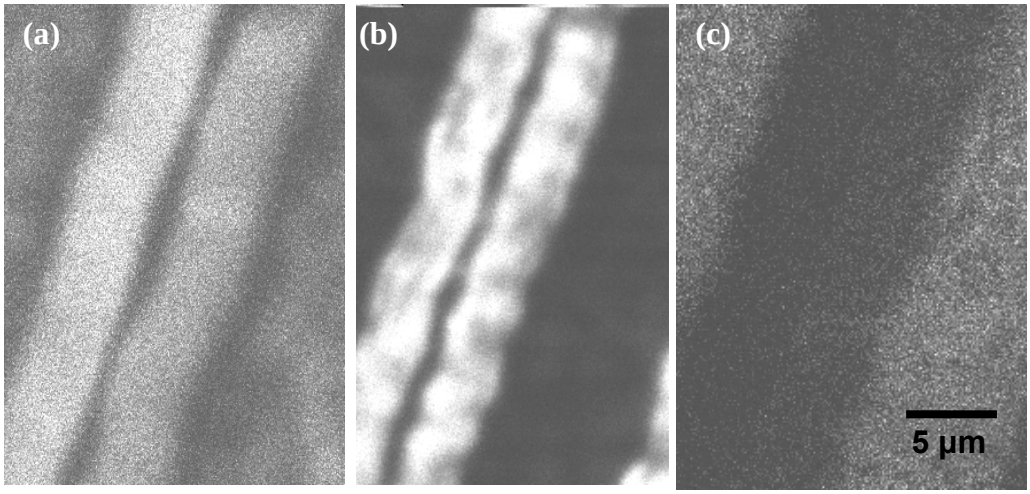

Fig. 4. 13. 80K CL images of (a) panchromatic CL (b) taken on 341nm and (c) taken on 344nm of the $Al_{0.1}Ga_{0.9}N$/GaN MQWs on the FACELO GaN templates.

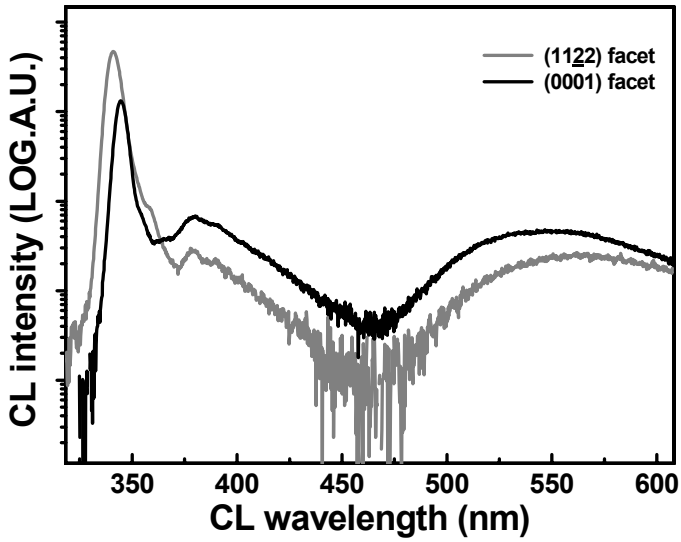

Fig. 4.14. 80K CL spectra recorded from the $Al_{0.1}Ga_{0.9}N$/GaN MQWs on FACELO GaN. The electron beam area is selectively focused on the (11$\bar{2}$2) and (0001) facet.

First, compressive stress shifts the peaks to higher energy. The value of 21 ± 3 meV/GPa was used as the factor of the CL peak shift in GaN induced by stress, [24] and we calculate that the stress component of the shift is about 3 – 4 meV for (11$\bar{2}$ 2) facet and 10 meV for (0001) plane GaN with respect to the bulk GaN.

However the peak from AlGaN/GaN MQW on $(11\bar{2}2)$ facet is actually on the higher energy side of that of (0001) facet, hence stress effect must be compensated by other stronger effects. If the strain is the only effect to induce the CL shift, then there should be red shift for the CL spectra peak on the $(11\bar{2}2)$ facet compared to the (0001) facet.

Second, quantum confinement of charge carriers in quantum wells must give blue shift, which is higher for thinner wells. The schematic band diagram of a quantum well without and with an internal electric field due to polarization effects is shown in figure 4.15 (a) and (b), respectively. For quantum well without any overall field, a blue shift is expected as compared to bulk GaN due to the quantum size effect. However, with an internal electric field, a red shift is expected. The different contributions to the transition energy are shown in figure 4.15(b) and the electric field effect will be discussed later with the polar induced electronic field. Using the energies indicated in figure 4.15, the optical band-to-band transition energy is given by:

$$E = E_{g,GaN} + E_{0,e} + E_{0,h} - e\vec{E}L_{QW} \qquad (4.2)$$

where $E_{g,GaN}$ is the GaN bandgap energy, and $E_{0,e}$ and $E_{0,h}$ are the quantized energies of the lowest electron and hole state in the triangular well, respectively, and the last term of Eq. (4.2) describes the energy drop within the GaN well layer of thickness L_{QW} due to the polarization field. Band bending due to free carriers and impurities is much less than polarization effects and is neglected. Excitonic transitions are not taken into account in Eq. (4.2); the effective excitonic Bohr radius is roughly four times smaller than the GaN well widths, implying that excitons would be ionized by the large electric field present there.

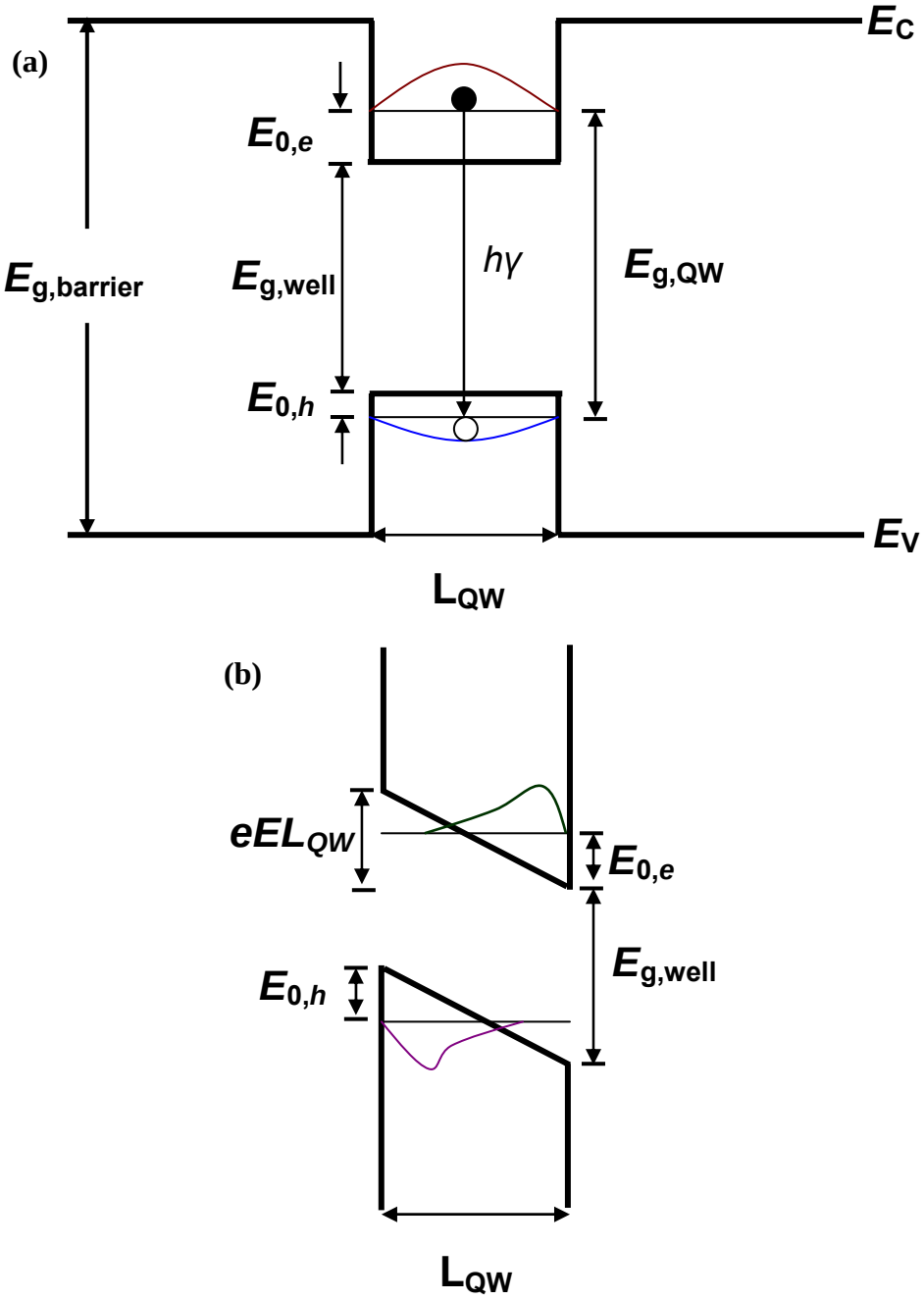

Fig. 4.15. Energy band diagram of $Al_xGa_{1-x}N/GaN$ single quantum well (a) without and (b) with internal polarization fields, the schematic show the different energies taken into account for the calculation of the optical transition energy.

As a rough estimation, we use electron effective mass as 0.2 m_0 to calculate the ground state energy in a deep well. To calculate the exciton energy in the quantum well, we consider the Hamiltonian

$$\left[-\frac{\hbar^2}{2m^*}\nabla^2 + V(z)\right]\psi = E\psi \tag{4.3}$$

where m^* is the effective electron mass, $|\psi|^2$ is the probability of finding the electron in the same unit cell. If we consider a deep well model, the quantum well thickness is *w* and make the potential *V(z)* is:

$$V(z) = \begin{cases} 0, & 0 < z < w \\ \infty, & z \le 0, or, z \ge w \end{cases} \tag{4.4}$$

Then the ground state energy of the quantum well can be roughly calculate with $h^2/8m^*a^2$, where *h* is the Plank constant, m^* is electron mass and *a* is the well width. Thus roughly we can obtain a shift of the AlGaN/GaN MQWs on $(11\bar{2}2)$ facet and that on (0001) facet compare to the GaN.

Third, GaN with wurtzite structure has a singular polar [0001] axis, and this creates an electrostatic field along the [0001] axis due to the spontaneous and piezoelectric polarization [25, 26]. According to the quantum-confined Stark effect, [27, 28] the CL peak energy of MQWs grown on the (0001)-faceted GaN will show a red shift compared to that grown on a non-polar surface. Then the polarization induced electronic field can be calculated in the AlGaN/GaN MQWs and the CL data was compared with our calculation results.

The analysis of the polar induced electricity field between the $(11\bar{2}2)$ and (0001) facets will be discussed in the following sections. (useful therotical exposition of effective-mass theory adapted to deal with piezoelectric field and spontaneous polar indced electronic field is given in Ref. 29-31, including usdful notation and basic formulas, and some applications.)

4.3.4.1 The static dielectric tensor — The calculation of the dielectric tensor is highly nontrivial, because it entails the determination of the electronic, as well as vibrational and elastic-piezoelectric, responses to an external electrostatic field. The elements of the dielectric tensor are:

$$\varepsilon_{ij}^{0} = \delta_{ij} + 4\pi \frac{dP_i}{dE_j} \tag{4.5}$$

where **E** is the screened macroscopic electrostatic field and **P** the polarization resulting from the response of the electronic and ionic degrees of freedom. In the *Born-Oppenheimer approximation* the polarization **P** in the presence of a generic strain or electrostatic perturbation can be conveniently expressed as $\mathbf{P} = \mathbf{P^0} + \mathbf{P^{lat}} + \mathbf{P^E}$, the sum of the spontaneous polarization $\mathbf{P^0}$ of the equilibrium structure in zero field, the polarization induced by lattice response, and the electronic screening polarization $\mathbf{P^E}$. In the linear regime and using Voigt notation, the two latter components can be expressed in terms of the lattice structure distortion and screened electric field as

$$P_i^{lat} = \sum_l e_{il}^0 \varepsilon_l + \frac{e}{V} \sum_{sj} Z_{ij}^{*s} u_j^s \tag{4.6}$$

$$P_i^E = \frac{1}{4\pi} \sum_j (e_{ij}^{\infty} - \delta_{ij}) E_j \tag{4.7}$$

where e_{ij}^{∞} is the electronic component of the dielectric tensor, V is the bulk cell volume, ε_l the strain field, u_j^s is the displacement of atom s from its equilibrium position, e_{il}^0 is the clamped-ion component of the piezoelectric tensor, and Z_{ij}^{*s} is the Born effective charge. Among the consequences of macroscopic polarization that we will demonstrate in this part, let us mention the following asssumptions:

(a) the electrical field caused by the fixed polarization charge, superimposed on the compositional confinement potential of the MQW, redshifts dramatically the transition energies and strongly suppresses interband transitions as the well thickness increases; (b) the effects of thermal carrier screening are negligible in typical MQW's, although not in massive samples; (c) a quasi-flat-band MQW

profile can be approximately recovered (i.e., polarization fields can be screened) only in the presence of very high free-carrier densities, appreciably larger than those typical of semiconductor laser structures; (d) even in the latter case, transition probabilities remain considerably smaller than the ideal flat-band values, and this reduces quantum efficiency. It is clear that a full understanding of these points will ultimately lead both to improvements in design and operation of real nitride devices, and to the direct measurement of polarization, and better knowledge thereof, in nitride material semiconductors.

4.3.4.2 Pizeoelctric fields in MQWs- Piezoelectricity is a well-known concept in semiconductor physics. Binary compounds of strategic technological importance as III-V arsenides and phosphides can be forced to exhibit piezoelectric polarization fields by imposing upon them a strain field.

Among others, applications of piezoelectric effects in semiconductor nanotechnology exist in the area of multi-quantum-well (MQW) devices. A thin semiconductor layer (well layer) is embedded in a semiconductor matrix (barrier layers) having a different lattice constant. If pseudomophic growth occurs, the active layer will be strained and therefore subjected to a piezoelectric polarization field. In a finite system, the existence of a polarization field implies the presence of electric fields. For the piezoelectric case, the magnitude of the latter depends on strain, piezoelectric constants, and on device geometry. The structure of a typical AlGaN/GaN MQW includes a number of a periods of GaN/AlGaN layers (GaN is well, AlGaN is barrier), where both the barrier layer and the well layer are in general strained to comply with the substrate in-plane lattice parameter. In such a structure, from the dielectric displacement conservation (Eqs.4.7) we can get the electric fields in the GaN and AlGaN layers

$$4\pi(P_{\mathrm{AlGaN}} - P_{\mathrm{GaN}}) = \varepsilon_{\mathrm{GaN}} E_{\mathrm{GaN}} - \varepsilon_{\mathrm{AlGaN}} E_{\mathrm{AlGaN}} \quad (4.8)$$

With periodicity implies $d_{\mathrm{GaN}} E_{\mathrm{GaN}} + d_{\mathrm{AlGaN}} E_{\mathrm{AlGaN}} = 0$ (4.9)

Solving for one of the field, we can obtain

$$E_{\mathrm{GaN}}^{PZ} = 4\pi d_{\mathrm{AlGaN}} (P_{\mathrm{AlGaN}}^{PZ} - P_{\mathrm{GaN}}^{PZ}) / (d_{\mathrm{AlGaN}} \varepsilon_{\mathrm{GaN}} + d_{\mathrm{GaN}} \varepsilon_{\mathrm{AlGaN}}) \quad (4.10)$$

$$E_{\mathrm{AlGaN}}^{PZ} = 4\pi d_{\mathrm{GaN}} (P_{\mathrm{GaN}}^{PZ} - P_{\mathrm{AlGaN}}^{PZ}) / (d_{\mathrm{AlGaN}} \varepsilon_{\mathrm{GaN}} + d_{\mathrm{GaN}} \varepsilon_{\mathrm{AlGaN}}) \quad (4.11)$$

where $\varepsilon_{\mathrm{AlGaN,GaN}}$ is dielctic constants and $d_{\mathrm{GaN,\ AlGaN}}$ is layer thickness of well and barrier. The piezoelectric polarization can be calculated with the piezoelectric coefficients e_{33} and e_{31} (Table 4.2) as

$$P^{PZ} = e_{33}\varepsilon_z + e_{31}(\varepsilon_x + \varepsilon_y) \quad (4.12)$$

If we make a_0 and c_0 the equilibrium values of the lattice parameters, $\varepsilon_z = (c\text{-}c_0)/c_0$ is the strain along the c-axis, and the in-plane strain $\varepsilon_x = \varepsilon_y = (a\text{-}a_0)/a_0$ is assumed to be isotropic. The third independent component of the piezoelectric tensor, e_{15}, is related to the polarization induced by shear strain, and will not be discussed. The relation between the lattice constants of the hexagonal GaN is given as

$$\frac{c - c_0}{c_0} = -2\frac{C_{13}}{C_{33}}\frac{a - a_0}{a_0} \quad (4.13)$$

where C_{13} and C_{33} are elastic constants (Table 4.2) Using Eqs. (4.12) and (4.13), the amount of the piezoelectric polarization in the direction of the c-axis can be determined by

$$P^{PZ} = 2\frac{a - a_0}{a_0}(e_{31} - e_{33}\frac{C_{13}}{C_{33}}) \quad (4.14)$$

Since $(e_{31} - e_{33}(C_{13}/C_{33})) < 0$ for AlGaN over the whole range of compositions, the piezoelectric polarization is negative for tensile and positive for compressive strained barriers, respectively.

4.3.4.3 Spontanous fields in MQWs- In the case of GaN, a basal surface should be either Ga- or N-faced. By Ga-face we mean Ga on the top position of the (0001) bilayer, corresponding to the [0001] polarity (the [0001] direction is given by a vector pointing from a Ga atom to a nearest-neighbor N atom). It is, however, important to note that the (0001) and (000$\bar{1}$) surfaces of GaN are nonequivalent and differ in their chemical and physical properties. These nonequivalents in GaN [0001] direction induce the spontaneous polar field. The spontaneous polarization for GaN and AlN was found to be negative, [32] meaning that for Ga(Al)-face heterostructures the spontaneous polarization is pointing towards the substrate. In the simplest case of a fully unstrained (substrate lattice-matched) MQW, the electric fields inside the layers are given, in analogy to Eq. (4.10 and 4.11), by

$$E_{\mathrm{GaN}}^{SP} = 4\pi d_{\mathrm{AlGaN}} (P_{\mathrm{AlGaN}}^{SP} - P_{\mathrm{GaN}}^{SP}) / (d_{\mathrm{GaN}} \varepsilon_{\mathrm{AlGaN}} + d_{\mathrm{AlGaN}} \varepsilon_{\mathrm{GaN}}) \qquad (4.15)$$

$$E_{\mathrm{AlGaN}}^{SP} = 4\pi d_{\mathrm{GaN}} (P_{\mathrm{GaN}}^{SP} - P_{\mathrm{AlGaN}}^{SP}) / (d_{\mathrm{GaN}} \varepsilon_{\mathrm{AlGaN}} + d_{\mathrm{AlGaN}} \varepsilon_{\mathrm{GaN}}) \qquad (4.16)$$

To calculate the amount of the polarization at the AlGaN/GaN MQWs in dependence of the Al-content x of the $Al_xGa_{1-x}N$ barrier, we use the following set of linear interpolations between the physical properties of GaN and AlN (Table 4.2)

lattice constant of $Al_xGa_{1-x}N$ layer:

$a(x) = (-0.077x+3.189)\times10^{-10}$ m, (4.17)

elastic constant of $Al_xGa_{1-x}N$ layer:

$C_{13}(x) = (5x+103)$ GPa, (4.18)

$C_{33}(x) = (-32x+405)$ GPa, (4.19)

piezoelectric constants of $Al_xGa_{1-x}N$ layer:

$e_{31}(x) = (-0.11x-0.49)$ C/m^2, (4.20)

$e_{33}(x) = (0.73x+0.73)$ C/m^2, (4.21)

spontaneous polarization of $Al_xGa_{1-x}N$ layer:

$P^{SP}(x) = (-0.052x\text{-}0.029)\ C/m^2$. (4.22)

4.3.4.4 Fields in the AlGaN/GaN MQWs- An ideal AlGaN Multiple Quantum Well (MQW) structure has n GaN QWs of width d_{GaN} and (n+1) barriers of width, d_{AlGaN}. Such a structure is schematically shown in Fig. 4.16. For simplicity we assume first that the structure is free-standing and nominally undoped, and that the Fermi level at the top of the structure lines up with the position in the GaN buffer layer. In that case the electric field in the MQWs caused by the polarisation fields can be approximated as follows:

$$E_{GaN}^{tot} = E_{GaN}^{SP} + E_{GaN}^{PZ} = d_{AlGaN}[(P_{AlGaN}^{SP} + P_{AlGaN}^{PZ}) - (P_{GaN}^{SP} + P_{GaN}^{PZ})]/(d_{GaN}\varepsilon_{AlGaN} + d_{AlGaN}\varepsilon_{GaN}) \quad (4.23)$$

And similarly

$$E_{AlGaN}^{tot} = E_{AlGaN}^{SP} + E_{AlGaN}^{PZ} = d_{GaN}[(P_{GaN}^{SP} + P_{GaN}^{PZ}) - (P_{AlGaN}^{SP} + P_{AlGaN}^{PZ})]/(d_{GaN}\varepsilon_{AlGaN} + d_{AlGaN}\varepsilon_{GaN}) \quad (4.24)$$

These expressions are obtained from the restriction that the displacement vector is along the *c*-axis. A common practical situation is that a multiple quantum well (MQW) structure is grown on top of a thick GaN buffer layer, which in turn is grown on sapphire. In this case the in-plane lattice parameter of the entire structure is adapted during growth with the GaN buffer layer. In our case, the AlGaN layers are in tension, while the GaN layers are less strained. So the spontaneous polar and pizeoelectic polar fields of AlGaN layer are along the $[000\bar{1}]$ direction. However, such an approximation is too simplistic and actually reproduces only qualitatively the field dependence of the energy shift. A full treatment of the data must go beyond the perturbation theory and requires a full solution of Schroedinger and Poisson equations, especially in the presence of injected carriers that screen the interal filed.

Table 4.2. Material parameters for GaN and AlN

		GaN	AlN
Band gap (eV)		3.4	6.2
Lattice Constant (Å)	a	3.189	3.112
	c	5.185	4.982
Piezoelectric Constant (C/m^2)	e_{31}	-0.49[32)]	-0.6[32)]
	e_{33}	0.73[32)]	1.46[32)]
Elastic Constant (GPa)	C_{13}	70[35)]	120[36)]
	C_{33}	379[35)]	395[36)]
Dielectric Constant	ε_{11}	9.5[33)]	9.0[34)]
	ε_{33}	10.4[33)]	10.7[34)]
Spontanous constant (C/m^2)		-0.029[32)]	-0.081[32)]

According to the previous theoretical study and T. Takeuchi *et.al.*s' work on the orientation dependence of piezoelectric effects in InGaN/GaN quantum wells [37], we can get a similar estimation of total polar electric fields in our AlGaN/GaN quantum wells on the (0001) facets and the (11$\bar{2}$2) facet. First, we consider the polarization fields in GaN well on the *c*-direction. In our case, about 2 μm GaN

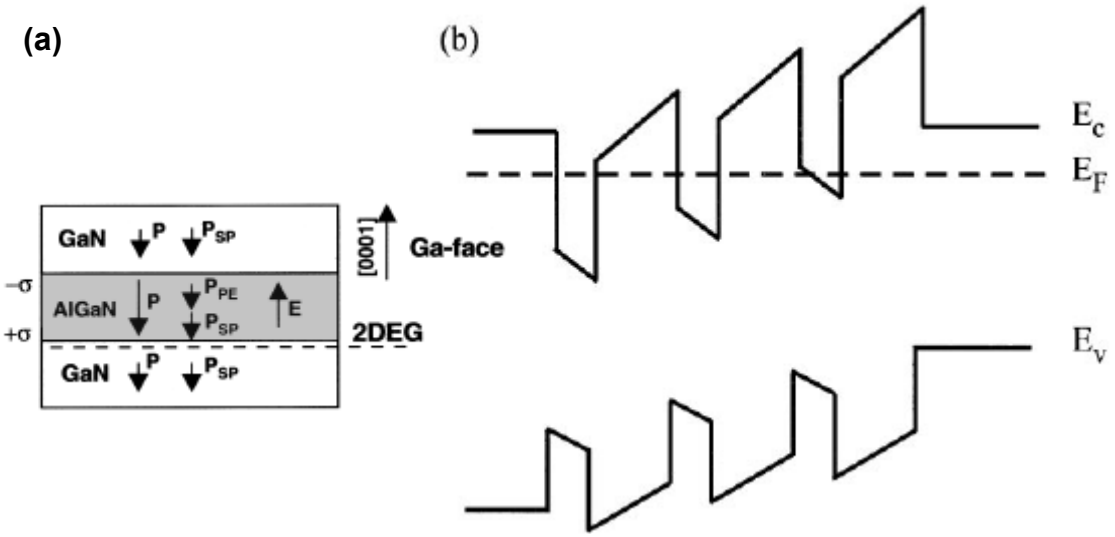

Fig. 4.16. (a) Schematic drawing of an AlGaN/GaN MQW structure and (b) schematic energy band diagram of the same structure.

layer was grown on the buffer GaN layer. The assumption that the GaN layer is totally strains relaxation can be made. So the piezoelectric polarization in GaN

well is 0 and only the spontaneous polarization field exists in it. Then for the AlGaN barrier layer, within the tensile strain, it induce the piezoelectric field along the [000$\bar{1}$] direction. That will be larger with the higher Al incorporation. And the spontaneous polarization is same direction with the piezoelectric polarization. With the data of the Al content, well and barrier thickness, we can calculate the polar induced electric field in the GaN well of the AlGaN/GaN MQWs. Along the [11$\bar{2}$2] direction, we can simply treat the spontaneous polarization as half of the [0001] direction, and because the difference of the lattice mismatch between the AlGaN and GaN is so small that we can neglect the orientation dependence of the strain. Thus, the detailed calculations of the $Al_{0.1}Ga_{0.9}N$/GaN MQWs are list in the Table 4.3.

Table 4.3. Estimated contributions toward the peak shift compared to the bulk GaN in CL spectra from the AlGaN/GaN MQWs on two facets.

Al Content	Facet	Well width (nm)	Contributions (meV)			Peak shift (meV)	
			Thermal strain	Quantum confinement	Stark effect	Calculated	Measured
$Al_{0.1}GaN$ /GaN	(0001)	5.5	10	62	–37	35	36
	(11$\bar{2}$2)	4	4	117	–27	94	72

So the Stark effect also contributes to the blue shift between the AlGaN/GaN MQWs on semipolar (11$\bar{2}$2) facet with respect to (0001) facet. Assuming that the 3 contributions of CL peak shift can be added, we can estimate the overall shifts, as shown in Table 4.3. In the calculation of quantum confinement of charge carriers in quantum wells, we are not including the difference of the barrier

heights between both facets. Thus we can explain why there is a large difference in CL shift exists between the theoretical and experiment values for the (11$\bar{2}$2) and (0001) facet in table 4.3. Hence in our case the main contribution toward the blue shift of CL from (11$\bar{2}$2) facets is the quantum confinement effect in MQWs.

The FWHM of the CL peak from AlGaN/GaN MQW on the (11$\bar{2}$2) facets is larger than that from (0001) faceted MQWs. Because the main factor for CL peak shift is quantum confinement of electrons, the peak broadening must be attributed first of all to random variations of quantum well width, which is more significant for rougher substrate and thinner wells. We attribute the broadening to the well-size fluctuation due to the non-unifromed triangular ELO GaN templates.

The CL peak intensity of the (11$\bar{2}$2) faceted is higher than that of the intensity recorded from the (0001) plane of AlGaN/GaN MQWs. And the lower yellow band intensity was also observed on the (11$\bar{2}$2) faceted than that on the (0001) facet. There are three main mechanisms contributing to the higher luminous intensity. First, the internal emission efficiency is significantly improved by the reduction of piezoelectric and spontaneous polarization fields. Secondly, the lower threading dislocation density was decreased on the (11$\bar{2}$2) faceted by using the FACELO method. At last, the roughened surface of the (11$\bar{2}$2) faceted induce higher light extraction related to multiple scattering events of emitted photons. These results show significantly enhanced optical properties of AlGaN/GaN MQWs grown on the (11$\bar{2}$2) facet compared to that grown on the (0001) facets. Such structures show the promising feasibility for realizing stronger oscillator strength for the UV/blue color lighting emitting diodes (LEDs) owing to the suppression of polar fields grown on FACELO GaN/sapphire templates.

4.4 InGaN/GaN multiple quantum wells grown on FACELO GaN templates

In this part, InGaN/GaN MQWs were grown on the FACELO GaN/Sapphire templates. The morphology and structure of the InGaN MQWs were characterized by SEM and TEM. The concentration of indium was measured by using HR-XRD. The optical properties of the InGaN MQWs on the $(11\bar{2}2)$ and the (0001) facets were studied using micro-Raman scattering and low temperature cathodoluminescence (CL) spectroscopy. Since the observation of multi-wavelengths light emission, this type of structure has potential as light-emitting devices for the purpose of generation of white light.

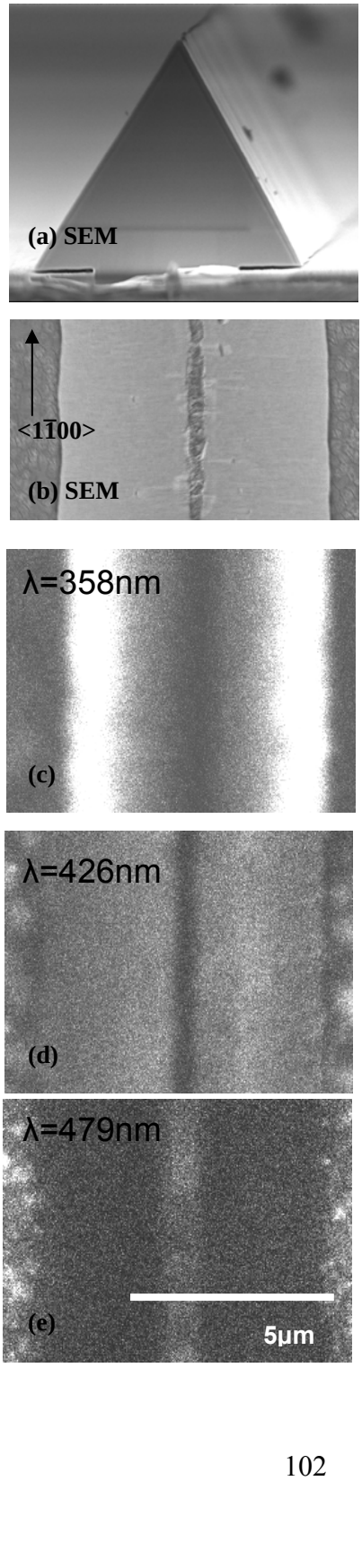

Fig. 4.17. The morphology and CL spatial distribution of the InGaN/GaN MQWs on the FACELO GaN/sapphire template, (a) cross-sectional and (b) top view SEM and CL image taken on (c) 358nm; (d) 426nm and (e) 479nm at temperature 80K.

4.4.1 Experimental

A 2.0 μm thick GaN layer was first deposited on the *c*-plane sapphire substrate by MOVPE. Trimethyl-metals and ammonia (NH_3) were respectively used as precursors for group III and N, and H_2 was used as carrier gas. A 100 nm thick SiO_2 mask was etched into stripes line pattern oriented in the $<1\bar{1}00>$ direction of GaN, defining a 4 μm wide opening

with a period of 12 μm. Then FACELO GaN templates with the $(11\bar{2}2)$ facets were selectively overgrown in 30 mins. The growth temperature was 950 ºC and reactor pressure was 500 Torr. After the SiO_2 mask was removed by HF solution, 5 periods of InGaN/GaN MQWs layers were grown on the whole surface. The target indium composition in the wells was 20%. The growth temperature was about 760 ºC, the reactor pressure was kept at 80 Torr, the growth time of well and barriers was 0.4 mins and 1.2 mins, respectively.

The morphology of the layers and cross-sections were studied with a JEOL 6700 field emission SEM. The internal structure of the InGaN MQWs was studied by Philips CM300 TEM. HR-XRD was also performed on the c-plane reference MQWs sample using a high resolution Philips XRD system. The extent of stress relaxation in the faceted GaN stripes and flat GaN was evaluated by micro-Raman scattering spectroscopy with a 514.5 nm excitation line from an Ar ion laser. Lateral resolution of Raman measurements was about 2 μm. The CL spectra were taken at 80K with accelerating voltage of 6kV (Quanta 200FEG).

4.4.2 Structure and Composition of InGaN MQWs grown on FACELO GaN templates

The morphology of InGaN/GaN MQWs grown on the FACELO GaN templates has the shape of a prism with a triangle in the cross-section, as shown in the SEM image (Fig. 4.17a). The triangle is 7 μm high and 8 μm wide. The dark rectangular shaped holes at the base of the triangles of ELO GaN are the voids formed due to the removal of the SiO_2 mask. Figure 4.18 shows the cross-sectional TEM images of the InGaN MQWs grown simultaneously on the (11$\bar{2}$ 2) facets and on the *c*-planes. In Fig. 4.18(a), it is clearly seen that the 5 periods of InGaN/GaN MQWs layers are grown on the (11$\bar{2}$2) facet successfully with total thickness of

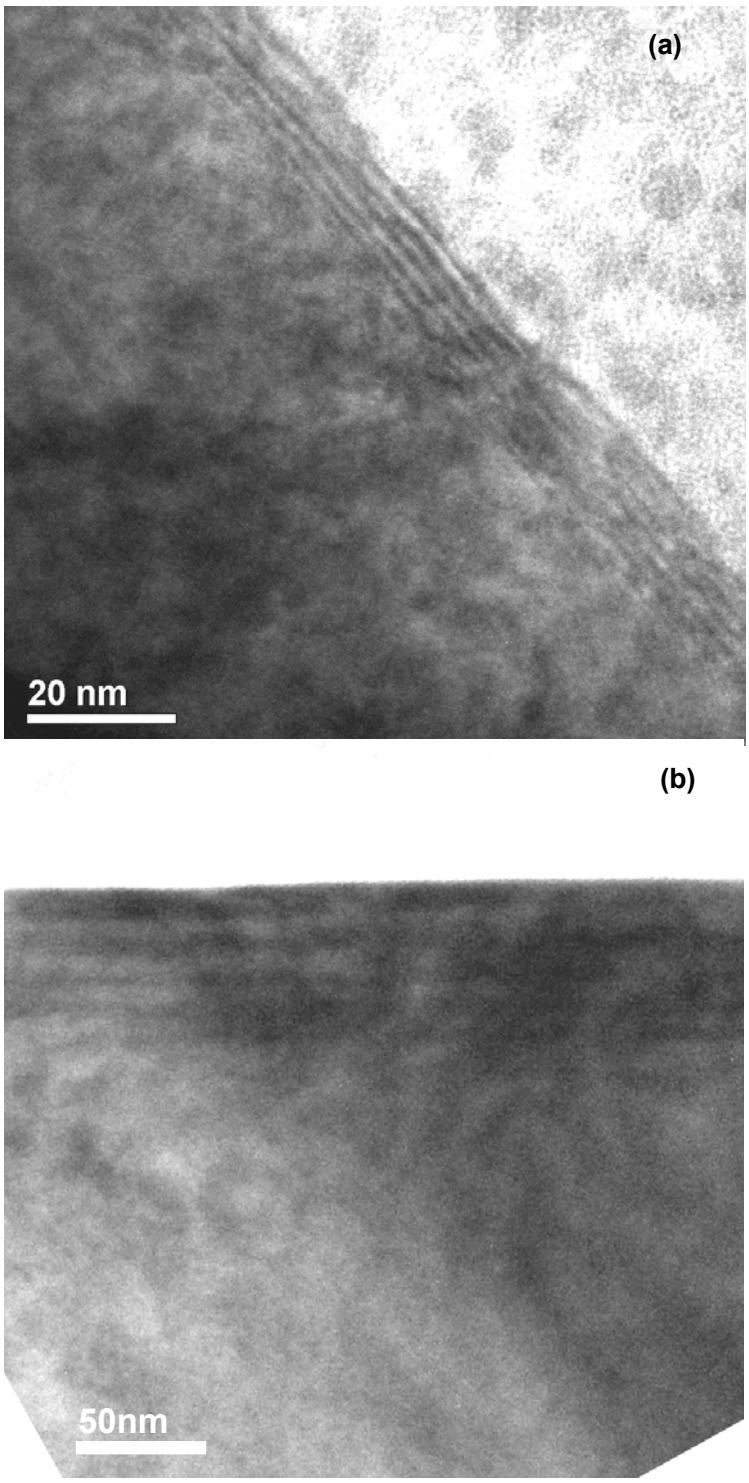

Fig. 4.18. The cross-sectional TEM images of the ELO InGaN/GaN MQWs, (a) taken along the (11 $\bar{2}$ 2) faceted MQWs; (b) taken along the *c*-plane MQWs.

about 11 nm. In Fig. 4.18(b), we observe *c*-plane or (0001)-oriented InGaN MQWs with a total thickness of 43 nm. There are evidently different growth rates of MQWs on these facets. As the GaN growth rates are found to be 4 times higher along the *c*-direction than those on the $(11\bar{2}2)$ facets, the well and barrier width in these planes are larger. The well and barrier thickness are approximately 1.1 nm

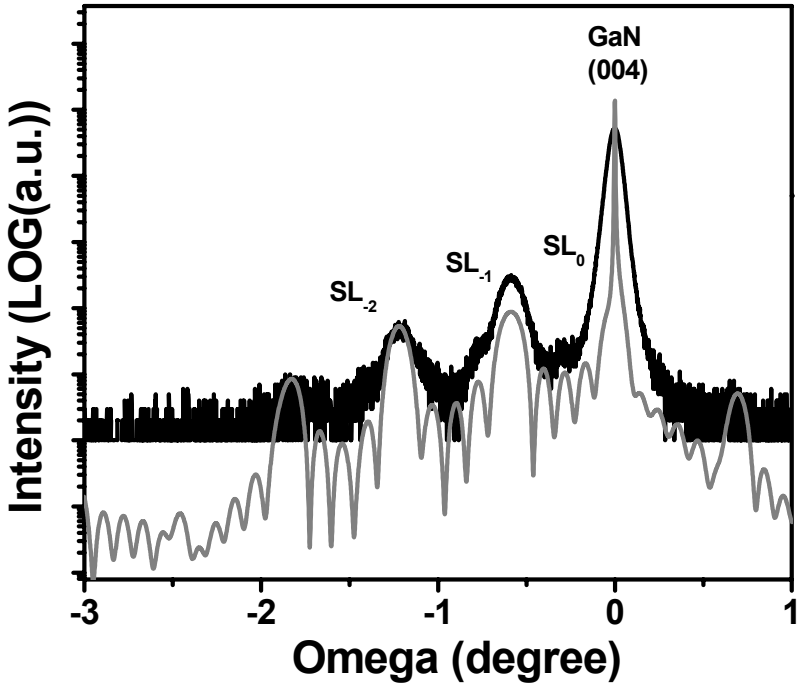

Fig. 4.19. High-resolution X-ray diffraction ω/2θ experimental (gray line) and calculated (black line) triple axis symmetrical scans near the (0004) GaN diffraction peak was taken on the reference c-plane InGaN/GaN MQWs.

and 1 nm respectively on the $(11\bar{2}2)$ facets and about 4.3 nm and 4 nm respectively on the c-plane. The growth rate on the two facets is controlled by the growth temperature and pressure. At a given growth pressure, a lower growth temperature led to a higher c-direction growth rate and lower lateral growth rate, similar observations were reported in Ref. [16].

To determine the indium composition in the InGaN/GaN MQWs, the XRD profile of the *c*-plane InGaN/GaN MQWs was taken in the vicinity of the (0004) diffraction, as shown in Fig.4.19. Satellite peaks were clearly seen, and the indium composition, well and barrier thicknesses were estimated to be 17%, 4.3 nm, and

4.3 nm respectively, by a fit using the dynamical diffraction theory. The error is reasonable because a 1% difference in the indium composition caused a discernible difference between the simulated and the experimentally obtained XRD profiles.

4.4.3 Optical Properties of InGaN MQW grown on FACELO GaN templates

The optical properties of the InGaN/GaN MQWs were investigated by micro-Raman scattering and low temperature cathodoluminescence spectroscopy. Raman scattering was used to examine the relaxation of compressive strain, which is due to the differences in the thermal expansion and lattice constants between GaN and sapphire. Raman spectra of the samples were recorded from different regions of

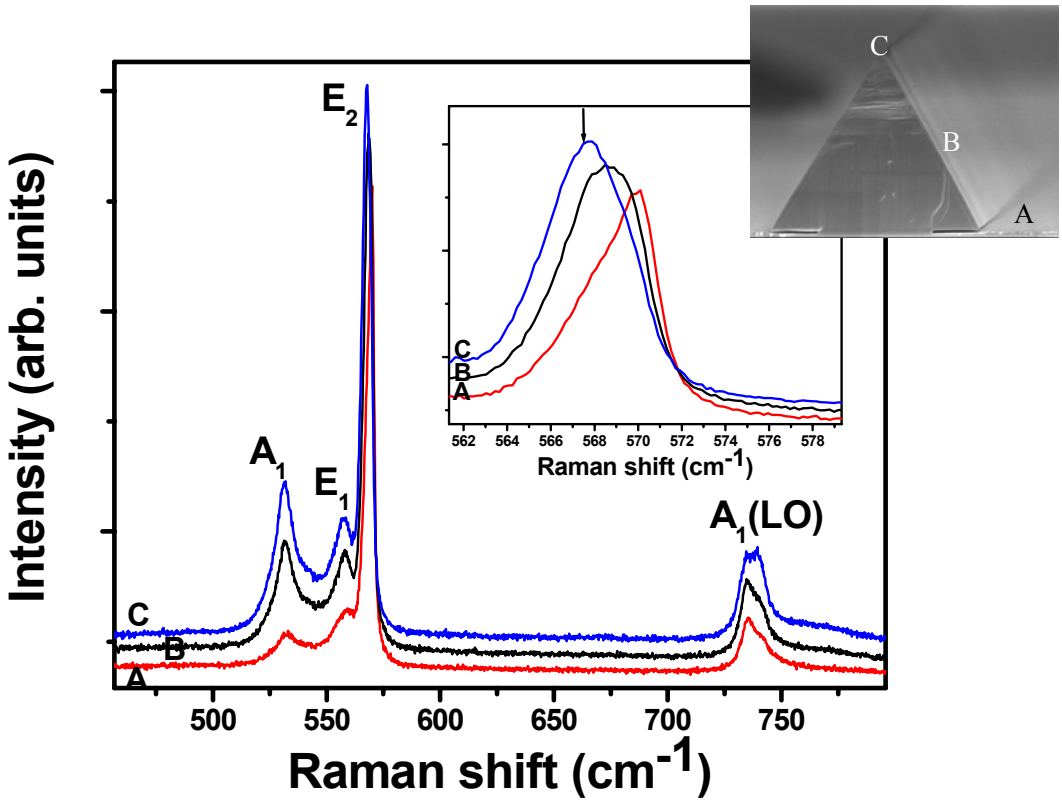

Fig. 4.20. Room temperature micro-Raman spectra recorded from the InGaN MQWs on FACELO GaN at different positions are marked in the inset of SEM image. The short arrow in the inset indicates the peak position recorded from the strain-free freestanding GaN.

the facets and are shown in Fig 4. 20. The E_2-high mode in the Raman spectra was used to measure the strain, because it has been proven particularly sensitive to the biaxial stress in GaN epitaxial layers. [21] Along the *c*-direction of the seed layer, the E_2-mode is shifted to higher frequencies with respect to the standard value of 567.5 cm^{-1} recorded from a 400 μm thick freestanding GaN substrate. The shift is about 2.0 ± 0.2 cm^{-1} on the GaN seed layer and only 0.4 ± 0.2 cm^{-1} on top of FACELO GaN templates. Intermediate values were recorded along the $(11\bar{2}2)$ facets. Using the proportionality factor of 4.2 cm^{-1}/GPa for hexagonal GaN, [23] we obtain the values of residual stress 0.47 ± 0.05 GPa in the GaN seed layer and a stress variation of 0.09 to 0.17 GPa on the $(11\bar{2}2)$ facet of the FACELO GaN. Thus the average strain relaxation difference between the two facets is about 0.3 GPa.

A top view SEM image of the sample surface is shown in Fig. 4.17(b). Figures 4.17(c)–(e) show monochromatic CL images obtained in the same region with different emission wavelengths. Corresponding to each emission wavelength, narrow stripe regions parallel to the $<1\bar{1}00>$ stripe can be clearly observed as the source of that luminescence. It showed that the shortest wavelength emission arises from the lower portion of the stripe, and longer wavelength emissions occur at the top of the triangular stripe. The nature of the luminescence in each narrow band in Fig. 4.17 can be best understood using luminescence spectra obtained by focusing the electron beam onto the two different facets. As shown in Fig. 4.21, the CL spectra of the $(11\bar{2}2)$ faceted InGaN MQWs show multiple luminescence peaks. Comparing with the CL images Fig.4.17(c)-(e), it can be deduced that the center of the peak shifts to progressively longer wavelengths as we move along the facet from substrate to apex. This clearly shows that the many peaks light

emission come from the individual stripe regions. In addition, only one peak can be seen from the CL spectra of the (0001) faceted InGaN MQWs. This indicates that the indium composition and well thickness is uniform on this (0001) surface. No GaN peak below InGaN MQWs is observed on the spectra of the (0001) facets. This is because of the thicker InGaN MQWs width of the (0001) facets than the $(11\bar{2}2)$ facets.

This wide spectra of the $(11\bar{2}2)$ faceted InGaN MQWs in Fig. 4.21 represent polychromatic emission. Thus, the $(11\bar{2}2)$ faceted InGaN MQWs effectively behave as several different quantum wells together, each giving a different

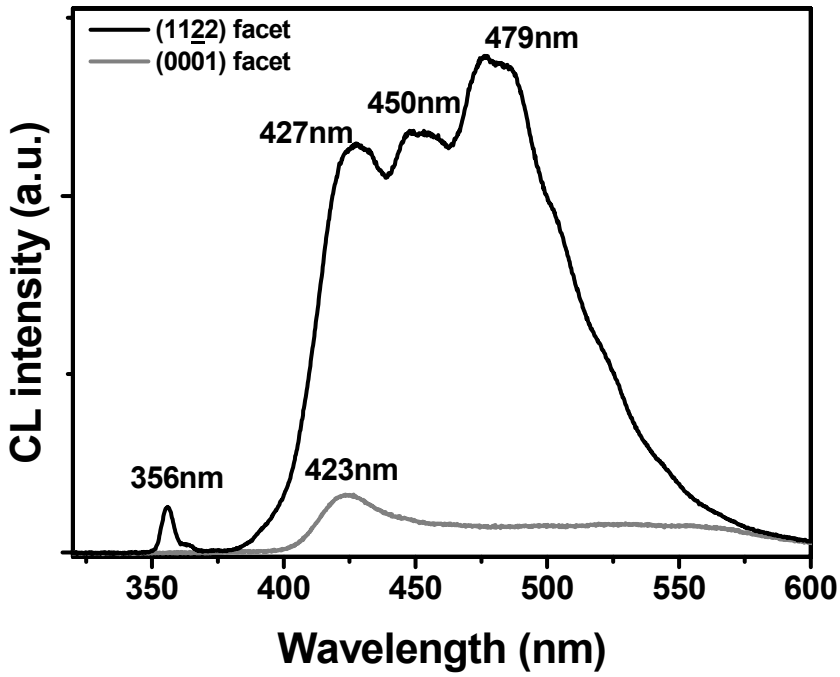

Fig. 4.21. CL spectra recorded at 80K with electron energy 6kV from the $(11\bar{2}2)$ and (0001) facets InGaN/GaN MQWs grown on FACELO GaN templates.

emission wavelength (423 nm, 450 nm, 479 nm), with their net addition resulting in polychromatic light. The range of wavelength can be tuned by varying the growth conditions. While a polychromatic emission was observed for the samples studied, under certain conditions, a white light spectrum could be obtained.

Based on the TEM and HR-XRD results, we are able to measure width of the quantum well region and indium composition of the InGaN MQWs on the *c*-plane. Using a simple model of retangular quantum well of width 3.6 nm with indium composition x=0.17 yields emission light energy about 2.6 eV. This is in good agreement with the range of wavelengths obtained from CL spectra of the (0001) faceted InGaN MQWs (Fig.4.21). But for the (11$\bar{2}$2) faceted InGaN MQWs, the spatial variation in the emission wavelength can be a result of both indium composition and/or quantum well width. However, we can not get a very clear TEM of the whole InGaN MQWs structures along the (11$\bar{2}$2) facet, so we can only estimate that the CL peak will have red shift from the base to the apex. Fortunately, our result is quite similar to the single InGaN quantum well grown on the ELO GaN templates reported by S. Srinivasan *et.al* [12], and their quantum well width changes from 1 nm to 4 nm along the (11$\bar{2}$2) facet from base to the top. So this wide spectra of the (11$\bar{2}$2) faceted InGaN MQWs could be induced by the variation of both the indium content and the quantum well width.

The measured CL peak intensity of the (11$\bar{2}$2) faceted InGaN MQWs is about 10 times of the intensity recorded from the (0001) InGaN MQWs, as shown in Fig. 4.21. These indicate that internal emission efficiency is significantly improved by the reduction of piezoelectric and spontaneous polarization fields. GaN with wurtzite structure has a singular polar [0001] axis, and this creates an electrostatic field along the [0001] axis due to the spontaneous and piezoelectric polarization. [32, 33] According to a theoretical study of the orientation dependence of piezoelectric effects in InGaN/GaN quantum wells, [27] the polar electric field along (11$\bar{2}$2) facet was estimated to be half of the value along (0001) facet. These results indicate impressive optical properties of InGaN MQWs grown on the (11$\bar{2}$

2) facets by FACELO method.

4.5 Chapter Summary

In this chapter, three different structures were grown on the <1$\bar{1}$00> direction patterned SiO_2 FACELO GaN/Sapphire templates. First the AlGaN layers were grown on the FACELO GaN templtes. The variation of the aluminum compositions was observed by SIMS, micro-PL. The reasons for these results have been analyzed. Secondly, Successful growth of AlGaN/GaN MQWs was achieved on the FACELO GaN/Sapphire templates. Periodic AlGaN/GaN MQWs structure was confirmed by TEM and SIMS. TEM showed that the average growth rate on the (11$\bar{2}$2) facet is lower than on (0001) plane. SIMS and HR-XED showed that the concentration of Al is higher on the (0001) facets than that on the (11$\bar{2}$2) facets. Micro Raman scattering revealed that there is a relaxation of compressive stress in FACELO GaN to when compared to the case of (0001) plane. Low temperature CL spectra showed a blue shift from (11$\bar{2}$2) facet with respect to the c-plane. This is in agreement with quantum confinement of electrons. Significantly improvement of the optical properties of AlGaN/GaN MQWs were observed on the (11$\bar{2}$2) facet compare to the (0001) plane. At last, InGaN MQWs structures were grown on the (11$\bar{2}$2) and (0001) facets by using the FACELO GaN/Sapphire templates. Periodic InGaN MQWs structures were confirmed by TEM and HR-XRD. TEM showed that the average growth rate on the (11$\bar{2}$2) facet is lower than on the (0001) plane by a factor of 0.25. Low temperature CL spectra had investigated that our InGaN MQWs structures on the (11$\bar{2}$2) facets provide wide range wavelength output light, which is suitable for the white color luminescence display devices. These properties make us believe that our structures

of the InGaN/GaN MQWs grown on the FACELO GaN templates are promising for light-emitting devices that require sophisticated syntheses of colors such as pastels and white.

Beside the nitride materials, ZnO grown on the FACELO GaN templates will be discussed in the following chapter because of the very lower lattice mismatch between the ZnO and GaN, there are also many interesting characteristics of such combined structures.

Reference:

[1] J. Park, P.A. Grudowski, C.J. Eiting, and R.D. Dupuis, "Selective-area and lateral epitaxial overgrowth of III–N materials by metal organic chemical vapor deposition" Appl. Phys. Lett. **73**, 333 (1998).

[2] O.-H. Nam, T.S. Zheleva, M.D. Bremser, and R.F. Davis, "Lateral epitaxial overgrowth of GaN films on SiO_2 areas via metalorganic vapor phase epitaxy" J. Electron. Mater. **27**, 233 (1998).

[3] K. Hiramatsu, K. Nishiyama, A. Motogaito, H. Miyake, Y. Iyechika, and T. Maeda, "Recent Progress in Selective Area Growth and Epitaxial Lateral Overgrowth of III-Nitrides: Effects of Reactor Pressure in MOVPE Growth" phys. stat. sol. (a) **176**, 535 (1999).

[4] F. Bernardini, V. Fiorentini, and D. Vanderbilt, "Spontaneous polarization and piezoelectric constants of III-V nitrides" Phys. Rev. B **56** R10024- R10027 (1997).

[5] R. Langer, J. Simon, V. Ortiz, N. T. Pelekanos, A. Barski, R. André, and M. Godlewski "Giant electric fields in unstrained GaN single quantum wells" Appl. Phys. Lett. **74** 3827-3829 (1999).

[6] T.Deguchi, K. Sekiguchi, A. Nakamura, T. Sota, R. Matsuo, S. Chichibu, S. Nakamura "Quantum-Confined Stark Effect in an AlGaN/GaN/AlGaN Single Quantum Well Structure" Jpn J. Appl. Phys. Par .2 **38**, L914-L916 (1999).

[7] T. Nishida and N. Kobayashi, Compound Semicond. **5**, 12-15 (1999).

[8] T. Takeuchi, H. Amano, and I. Akasaki, "Theoretical Study of Orientation Dependence of Piezoelectric Effects in Wurtzite Strained GaInN/GaN Heterostructures and Quantum Wells" Jpn. J. Appl. Phys., Part 1 **39** 413-416 (2000).

[9] H. M. Ng, "Molecular-beam epitaxy of GaN/$Al_xGa_{1-x}N$ multiple quantum wells on *R*-plane (10$\bar{1}$2) sapphire substrates" *Appl. Phys. Lett.* **80**, 4369-4371 (2002).

[10] M. D. Craven, S. H. Lim, F. Wu, J. S. Speck, and S. P. DenBaars, "Threading dislocation reduction via laterally overgrown nonpolar (11$\bar{2}$0) *a*-plane GaN" Appl. Phys. Lett. **81** 1201-1203 (2002).

[11] K. Nishizuka, M. Funato, Y. Kawakami, S. Fujita, Y. Narukawa, and T. Mukai, "Efficient radiative recombination from <11$\bar{2}$2> -oriented $In_xGa_{1-x}N$ multiple quantum wells fabricated by the regrowth technique" Appl. Phys. Lett. **85**, 3122 (2004).

[12] S. Srinivasan, M. Stevens, F. A. Ponce and T. Mukai, "Polychromatic light emission from single InGaN quantum wells grown on pyramidal GaN facets" Appl. Phys. Lett., **87,** 131911 (2005).

[13] B. Neubert, P. Brückner, F. Habel, F. Scholz, T. Riemann, J. Christen, M. Beer and J. Zweck, "GaInN quantum wells grown on facets of selectively grown GaN stripes" Appl. Phys. Lett., **87,** 182111 (2005).

[14] B. Monemar, "Fundamental energy gap of GaN from photoluminescence excitation spectra" Phys. Rev. B **10,** 676-681 (1974).

[15] S. Nakamura, M. Senoh, S. Nagahama, N. Iwasa, T. Yamada, T. Matsushita, H. Kiyoku,Y. Sugimoto, T. Kozaki, H. Umemoto, M. Sano, and K Chocho, "InGaN/GaN/AlGaN-based laser diodes with modulation-doped strained-layer superlattices grown on an epitaxially laterally overgrown GaN substrate" Appl. Phys. Lett., **72** 211-213 (1998).

[16] H.Miyake, A.Motogaito, K.Hiramatsu "Effects of Reactor Pressure on Epitaxial Lateral Overgrowth of GaN via Low-Pressure Metalorganic Vapor Phase

Epitaxy" Jpn. J. Appl. Phys. **38,** L1000 (1999).

[17] D. Brunner, H. Angerer, E. Bustarret, R. Hopler, R. Dimitrov, O. Ambacher, and M. Stutzmann, "Optical constants of epitaxial AlGaN films and their temperature dependence" J. Appl. Phys., **82,** 5090 (1997).

[18] R. A. Logan, S. N. G. Chu, M. Geva, N. T. Ha, and C. D. Thurmond, "Zinc incorporation into InP grown by atmospheric pressure metalorganic vapor phase epitaxy" J. Appl. Phys., **79**, 1371 (1996).

[19] G. S. Huang, X. H. Tang, B. L. Zhang, and S. C. Tjin, "Arsenic incorporation into InGaAsP grown by low-pressure metalorganic vapor phase epitaxy using tertiarybutylarsine and tertiarybutylphosphine in N ambient" J. Appl. Phys., **94**, 4890 (2003).

[20] P.Ruterana, M.Albercht, J.Neugebauer Nitride semiconductors: handbook on materials and devices Wiley-VCH, P310 (2003)

[21] G. S. Huang, H. H. Yao, T. C. Lu, H. C. Kuo, and S. C. Wang, "Aluminum incorporation into AlGaN grown by low-pressure metal organic vapor phase epitaxy" J. Appl. Phys., **99,** 104901 (2006).

[22] C. Touzi, F. Omne` s, B. El Jani, P. Gibart, "LP MOVPE growth and characterization of high Al content $Al_xGa_{1-x}N$ epilayers" J. Crys. Growth., **279**, 31 (2000).

[23] H. Harima, "Properties of GaN and related compounds studied by means of Raman scattering" J. Phys.: Condens. Matter, **14** R967-R993 (2002).

[24] C. Kisielowski, J. Kruger, S. Ruvimov, T. Suski, J. W. Ager, E. Jones, Z. Liliental, M. Rubin, and E. R. Weber, "Strain-related phenomena in GaN thin films" Phys. Rev. B **54** 17745-11753 (1996).

[25] V. Fiorentini, F. Bernardini, F. Della Sala, A. Di Carlo, and P. Lugli "Effects

of macroscopic polarization in III-V nitride multiple quantum wells" Phys. Rev. B **60,** 8849-8858 (1999).

[26] A. D. Bykhovski, B. L. Gelmont, and M. S. Shur "Elastic strain relaxation and piezoeffect in GaN-AlN, GaN-AlGaN and GaN-InGaN superlattices" J. Appl. Phys. **81** 6332-6338 (1997).

[27] E. E. Mendez, G. Bastard, L. L. Chang, L. Esaki, H. Morkoc, and R. Fischer, "Effect of an electric field on the luminescence of GaAs quantum wells" Phys.Rev.B **26** 7101-7104 (1982).

[28] G. Bastard, E. E. Mendez, L. L. Chang, and L. Esaki, "Variational calculations on a quantum well in an electric field" Phys. Rev.B **28** 3241-3245 (1983).

[29] S.-H. Park and S.-L. Chuang, "Crystal-orientation effects on the piezoelectric field and electronic properties of strained wurtzite semiconductors" Phys. Rev. B, **59**, 4725 (1999).

[30] F. Bernardini, V. Fiorentini, and D. Vanderbilt, "Polarization-Based Calculation of the Dielectric Tensor of Polar Crystals" Phys. Rev. Lett., **79**, 3958 (1997).

[31] F. Bernardini and V. Fiorentini, "Electronic dielectric constants of insulators calculated by the polarization method" Phys. Rev. B, **58**, 15292 (1998).

[32] F. Bernardini, V. Fiorentini, and D. Vanderbilt, "Spontaneous polarization and piezoelectric constants of III-V nitrides" Phys. Rev. B, **56**, 10024 (1997).

[33] A. S. Barker Jr. and M. Ilegems, "Infrared Lattice Vibrations and Free-Electron Dispersion in GaN" Phys. Rev. B, **7**, 743 (1973).

[34] K. Tsubouchi, N. Miskoshiba, "Zero-Temperature-Coefficient SAW Devices on AlN Epitaxial Films" IEEE Trans. Sonics Ultrason., **SU-32**, 634 (1985).

[35] Y. Takagi, M. Ahart, T. Azuhato, T. Sota, K. Suzuki, and S. Nakamura, "Brillouin scattering study in the GaN epitaxial layer" Physica B, **219&220**, 547 (1996).

[36] K.Tsubouchi, K.Sugai, and N. Mikoshiba, "Photoacoustic and Photoluminescence Measurements of Defects in Semiconductors" IEEE Ultrason., **Symp. 1**, 375 (1981).

[37] T. Takeuchi, H. Amano and I. Akasaki, "Theoretical Study of Orientation Dependence of Piezoelectric Effects in Wurtzite Strained GaInN/GaN Heterostructures and Quantum Wells " Jpn. J. Appl. Phys. Part 1, **39,** 413 (2000).

Chapter 5

Chapter 5 Morphology controllable growth of ZnO on the FACELO GaN templates and RBS characterization

5.1 Introduction

ZnO with a band gap of 3.37 eV is of great interest for applications in opto- and nanoelectronics. It has been reported that the blue-UV emission can be generated from ZnO thin-films, [1] ZnO whiskers, [2] p-type ZnO films, [3] and thin-film diode structures [4] at room temperature. Thin layers of ZnO have been grown by various methods, including chemical vapor deposition (CVD), [5, 6] pulsed laser deposition (PLD), [7, 8] molecular beam epitaxy (MBE), [9, 10] and dc- or rf- magnetron sputtering. [11, 12]

In the previous works, sapphire has been used as the substrate to produce epitaxial ZnO films [13-15]. Recently, several groups reported the fabrication of n-ZnO/p-GaN electroluminescent devices and demonstrated the potential to realize photonic and electronic devices [16, 17]. The ZnO film quality can be significantly improved because of the lower lattices mismatch between the GaN and ZnO (~1.9%). However, because of the high dislocation density (around 10^9-10^{10} cm^{-2})

in the GaN grown on c-sapphire, the as-grown ZnO films on *c*-GaN are well known to contain higher defect densities, which are mainly threading dislocations. A technique, which can help to overcome this problem, is FACELO [18-20]. It is realized by starting the epitaxial growth on (0001) plane and tuning the growth conditions to develop other facets, e.g. $(1\bar{1}01)$ and $(11\bar{2}2)$, on ELO stripes. D. Andeen *et al.* also reported the reduced dislocation of the ELO ZnO which was grown on $MgAl_2O_4$ (111) substrate by hydrothermal process [21]. Recently, K. Nishizuka *et al.* [22], F. A. Ponce *et al.* [23] and Barbara Neubert *et al.* [24] grew InGaN/GaN, AlGaN/GaN quantum wells structures on the FACELO GaN templates, which led to higher internal quantum efficiency than those of traditional *c*-plane due to the decrease of polarization. Narukawa *et.al* also proved that the higher quantum efficiency of the QWs was found on the $(11\bar{2}2)$ semi-polar facets than the (0001) polar surface [25]. However, the ZnO material was not attracted enough attention about this kind of combination. The ZnO films grown on the FACELO GaN templates will not only realize high crystal property but also achieve a reduced polarization field on the ZnO/GaN hetero-interface.

5.2 Morphology controllable ZnO growth

In the preparation of ELO GaN, a 2 μm GaN film was first deposited by the MOCVD system on a c-plane sapphire substrate with low temperature GaN as a buffer layer. Trimethyl-metals and ammonia (NH_3) were used as sources of Ga and N, respectively, with H_2 as carrier gas. A 100 nm SiO_2 mask was patterned into stripes oriented in the GaN $<1\bar{1}00>$ direction, defining a 5 μm wide opening with a period of 13 μm. FACELO GaN layers were grown via controlling the growth temperature and the reactor pressure by FACELO. The growth temperature

and reactor pressure were 1000ºC and 200 Torr, respectively. The FACELO GaN/sapphire substrates were then put into a tube furnace to grow the ZnO films by thermal vaporization and condensation of Zn (99.99% purity) in the presence of oxygen. The alumina boat with Zn powder was placed at the center of a quartz tube and purged with Helium (99.999% purity) at a flow rate of 100 sccm. The furnace temperature was increased to growth temperature, and an oxygen (99.99% purity) flow was introduced into the reactor. The mixed O_2 and He gas was maintained throughout the whole reaction process, which normally takes 30 minutes. The ZnO/GaN/sapphire layers were studied with SEM (JEOL JSM-6700F, 5 kV), TEM (Philips CM300, 300 kV), high-resolution XRD (Philips MRD system), RBS (Set up by Center for Ion Beam Application at the National University of Singapore with 3.5 MeV singletron accelerator). Channeling contrast microscopy (CCM) was used to image the micron sized overgrown regions of FACELO ZnO, using a 2-MeV alpha particle beam with a sub-micron spot-size. [35] Channeling RBS spectra were recorded with 300 mm^2 PIPS detector with 22 KeV energy resolution at a scattering angle of 145º, and micro PL system (Renishaw, the PL spectra were recorded using a 325 nm excitation line with a lateral resolution of 2.0 μm).

Between the GaN triangular ridges, as shown in Fig.5.1, SiO_2 is chosen as the masking material to prevent nucleation of ZnO on it and the epitaxial growth takes place on the unmasked regions, forming a pattern of parallel strips on the substrate surface. With the increase in the growth temperature, the growth morphology of ZnO changes from long, needle-shaped nanorods to rectangular stripes with (0001) top facets and nonpolar $(11\bar{2}0)$ sidewalls, finally to triangular stripes with $(11\bar{2}2)$ sidewalls, as seen in Fig.5.2. This results show that the ZnO growth facets can be

controlled by the growth parameters and the overgrown region can achieve a reduced dislocation density in the entire epitaxial film. The X-ray diffraction (XRD), Rutherford Backscattering (RBS), high resolution transmission electron microscopy (HRTEM) and room temperature photoluminescence (PL) were used to characterize the ZnO films. This method can be used to fabricate ZnO/GaN heterostructures with low dislocation densities, which may find important applications in future electronics and the fabrication of hybrid n-ZnO/p-GaN optoelectronic devices on sapphire.

5.2.1 SEM results characterization

The original cross section view of FACELO GaN stripe with <1$\bar{1}$00> direction has a height of 5 μm and a base width of 6 μm (Fig. 5.1a). A SiO_2 layer with a thickness of 100 nm is located at the regions between stripes, serving as shadow

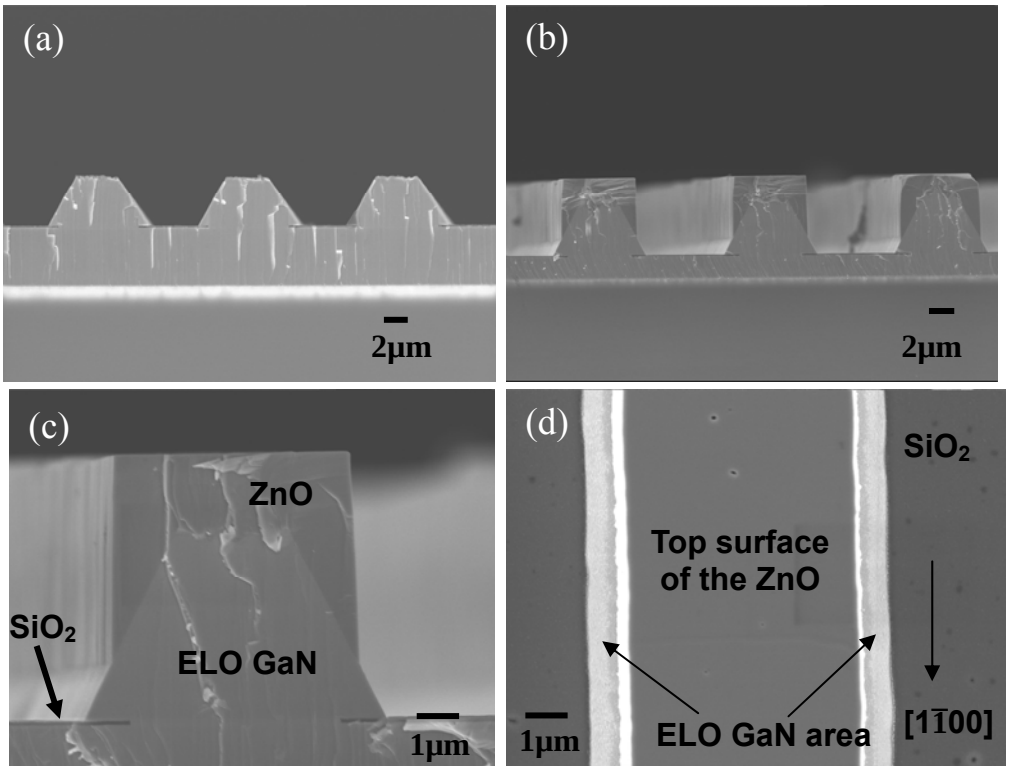

Fig. 5.1.a) Typical SEM of as-grown ELO GaN on sapphire substrate. b) Cross-sectional scanning electron microscopy (SEM) of ZnO grown on the ELO GaN template; (b) and (c) are from the same sample at different magnification. d) Top view of the sample.

masks during growth. The cross-sectional SEM of a typical ZnO film grows on the FACELO GaN/sapphire substrate (Figs. 5.1b and c). The sample was grown by using the temperature of 800ºC ± 5 ºC and oxygen flow rate of 10 sccm. The selective growth showed good repeatability under the conditions above. The ZnO film is grown on the facet controlled-ELO GaN stripe templates and has laterally overgrown a portion of the SiO_2 mask layers. The smooth morphology of the partially overgrown ZnO film is observed in a top-view SEM image (Fig. 5.1d), indicating the reduction of the threading dislocations.

5.2.2 ZnO morphological variation with growth parameter

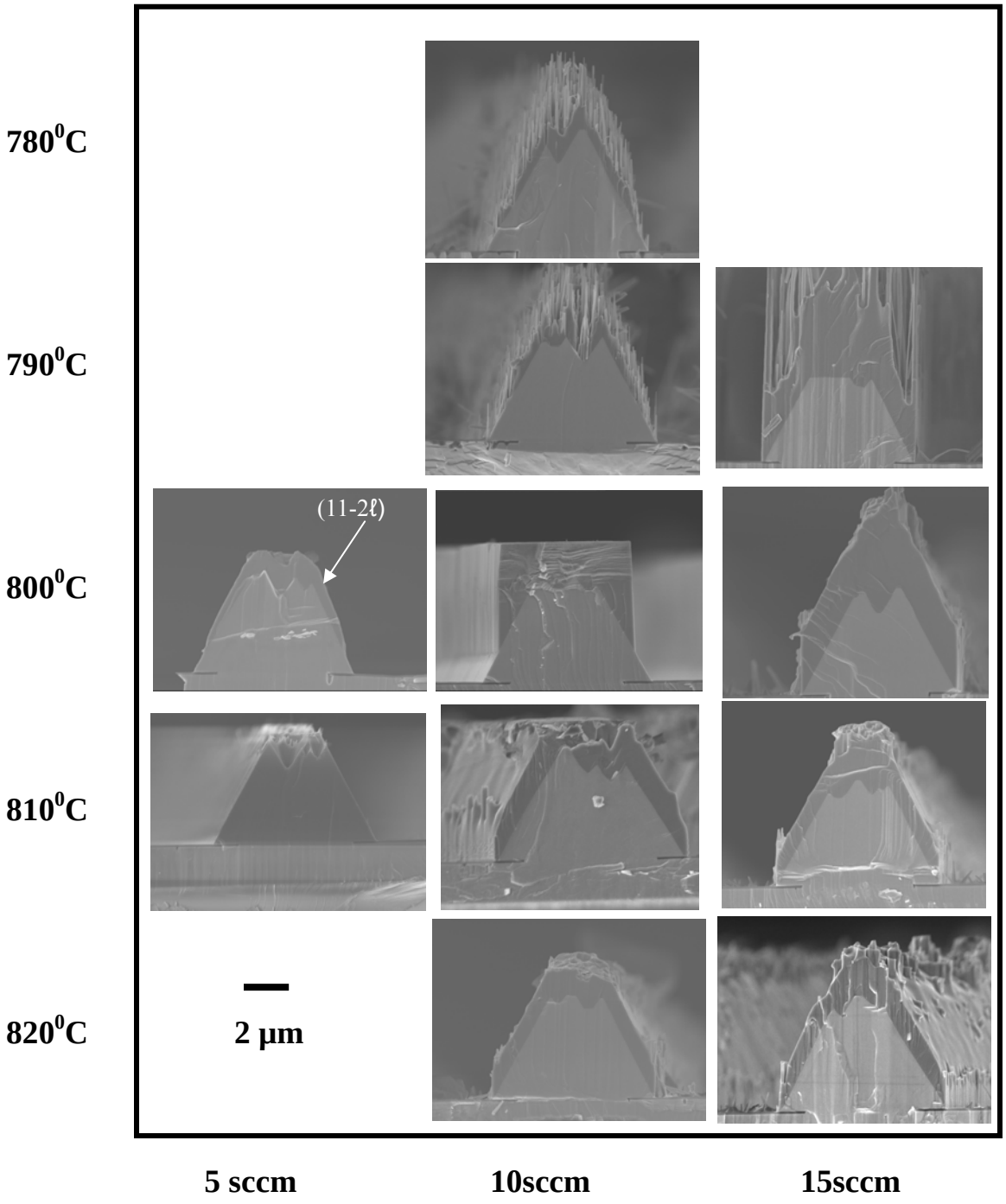

Fig. 5.2 Morphological changes in ELO ZnO for different growth temperature and oxygen flow rate. Growth time was 0.5 h.

Growth of ZnO is believed to be dominated by the vapor–solid (VS) process in the thermal evaporation method. Much work has been done both experimentally and theoretically on the kinetics of the whiskers growth [26-28]. The two dimensional (2D) nucleation probability on the surface of a whisker was established to be

$$N_p = B\exp(-\frac{\pi\sigma^2}{k^2T^2\ln S}) \quad (5.1)$$

where N_p is the nucleation probability, B is a constant, σ is the surface energy, k is the Boltzmann constant, T is the absolute temperature, and S is the gas-phase supersaturation ratio determined by $S=p/p_0$, where p is the actual vapor pressure and p_0 is the equilibrium vapor pressure corresponding to temperature T. The experiment parameters that could determine the morphology of the ZnO growth include the gas-phase supersaturation, the surface energy of the growth facets, the growth temperature, temperature gradient in the chamber, the heating rate, the gas flow rate and the distance between the source materials and the substrate.

We kept all the other experiment parameters constant, and the dependence of the ZnO morphology on the growth temperature and oxygen flow rate was systematically studied. Figure 5.2 displays the morphological structures of ZnO dependence on the growth temperature and oxygen flow rate. We would like to firstly explain the morphology dependence on the growth temperation. According to the different growth temperatures of the ZnO growth, it can be divided into three regions. In region I (T < 800ºC), the as-grown ZnO forms long needle-shaped nanorods with a typical diameter of around 100 nm and 7 μm height on the GaN template due to the very high growth rate in the *c*-direction and the poor

surface migration of Zn atoms on the (0001) surface at low temperatures (Fig. 5.3). In region Π, with the increase in the growth temperature, the side walls change from vertical non-polar (11$\bar{2}$0) facets to inclined (11$\bar{2}$2) facets. The uniform and rectangular shape ZnO structures were observed in this region. However, only a small growth temperature vs flow rate region can achieve the smooth (0001) surface. The morphology changes with growth temperature from 800 ºC to 810 ºC,

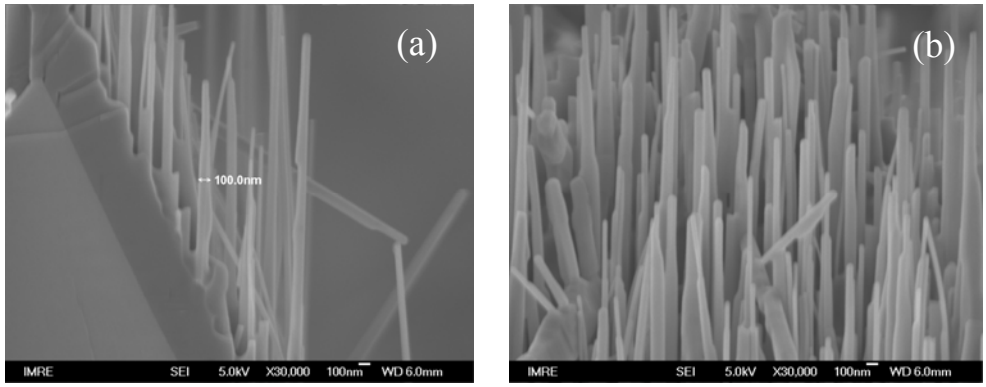

Fig. 5.3. High resolution scanning electron microscopy (SEM) cross-sectional view (a) and side view (b) image of grown at 780ºC nanorods ZnO grown on the ELO GaN template.

here are some intermediate growth regimes whereby both the (11$\bar{2}$0) and the (11$\bar{2}$2) facets are formed as shown in Figure 5.4. It was noted that the (11$\bar{2}$2) surface area keep increasing while the (11$\bar{2}$0) surface is disappearing with the higher growth temperature. In region ΙΙΙ, at higher temperatures, the inclined (11 $\bar{2}$ 2) surface becomes rough due to the increase in the evaporation rate of absorbed source molecules on that surface. The variations of the 2D nucleation probability on the different facets were studied to investigate the mechanism

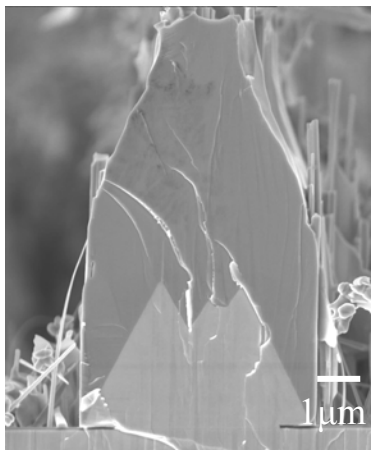

Fig. 5.4. SEM cross-sectional image of grown at 805ºC ZnO grown on the FACELO GaN template, with both (11$\bar{2}$0) and (11$\bar{2}$2) facets.

behind these observations. According to Equation 5.1, the higher temperature increases the gas-phase pressure of ZnO [28], which means higher supersaturation. Therefore, the higher temperature introduces the higher 2D nucleation probability. On the other hand, the surface energy is related to the crystal plane, a low-miller index crystal surface is of lower surface energy. [28] The lower surface energy leads the larger 2D probability of nucleation. Meanwhile, an atom absorbed on a low-energy surface has low binding energy and a high probability of desorption. [29] Competition between the supersaturation and surface energy is responsible for the temperature dependence of the ZnO morphology. At lower temperature, the probability of desorption is lower and lower millier index plane achieve larger 2D probability of nucleation, it will leads to the wire like ZnO structures. As a result, the growth rate on [0001] direction is relatively higher and suppress the other facets growth rate like $\{11\bar{2}2\}$ and $\{11\bar{2}0\}$, so the ZnO nanorods structures with lower volume ZnO was grown on the GaN. When the temperature increases, the volume of ZnO grown on the GaN is larger corresponding to the increased supersaturation. However, the higher temperature will also induce larger desorption probability of the adatoms on the (0001) surface, it results the lower growth rate on the *c*-plane. At the same time, the temperature dependence of the growth rate on the $\{11\bar{2}2\}$ and $\{11\bar{2}0\}$ facets are hard to investigate. The competitive capturing of the adatoms is more serve among these three different facets. When the crystal has several fast growth directions, for example, the {0001} and $\{11\bar{2}2\}$ is the fast growth surface of the ZnO crystal. [30] According to the research work of the different facets growth rate about the FACELO GaN, [11] because of the same crystal structures like the GaN, we could assume that the ZnO $\{11\bar{2}0\}$ growth rate will increase when the temperature is higher. In particularly, at

the region II the increasing temperature cause higher growth rate on the $\{11\bar{2}0\}$ facets, at the same time, the growth rate on the $\{11\bar{2}0\}$ surface is also competing with the $\{11\bar{2}2\}$ facets. Then at 800 ºC, the $\{11\bar{2}0\}$ facets appears as the competing results. When the temperature goes higher (>800 ºC), the $\{11\bar{2}0\}$ growth rate will be keep increasing. At last, the $\{11\bar{2}2\}$ facets will finally dominate over the $\{11\bar{2}0\}$ facets. Furthermore, the differences in the stability of each surface also contribute to the growth rate, and such surface stability depends on the surface energy. Therefore, the ZnO $(11\bar{2}2)$ facets is energetically more stable than the $\{11\bar{2}0\}$ facets. The final morphology of the ZnO is the results of the competition among these facets growth rate.

Secondly, when we keep the growth temperature constant and change the oxygen flow rate, different growth rates on the $(11\bar{2}2)$ and (0001) facets were observed with various oxygen flow rates, as shown in Figure 5.2. At the low oxygen flow rate (5 sccm) region, the very low supersaturation was obsevered due to the quite small oxygen flow rate, the volume of the growth ZnO on ELO GaN is quite small. As the oxygen flow rate increasing, the supersaturation will be increased. Therefore, the increasing oxygen flow rate introduces the higher supersaturation corresponding to the larger volume of the growth ZnO, as shown in Fig.5.2. At a constant temperature, the desorption probability of adsorb atoms will not change. So the (0001) surface with lower surface energy will lead to the higher growth rate with higher oxygen flow rate, which further verifies by the morphology changes observed in Figure 5.2. Therefore, the increasing oxygen flow rate has an opposite effect on the [0001] growth rate which could compensate the decrease induced by the higher growth temperature.

Based on the previous discussions, the surface energy and the

supersaturaion are two dominant growth factors in controlling the morphology of the ZnO in the VS growth process.

5.2.3 TEM characterization

The microstructure of the top layer and the nature of the epitaxial growth of ZnO films grown at 800ºC with an oxygen flow rate of 10sccm were further investigated by HRTEM. Figure 5.5 shows a typical HRTEM image of the

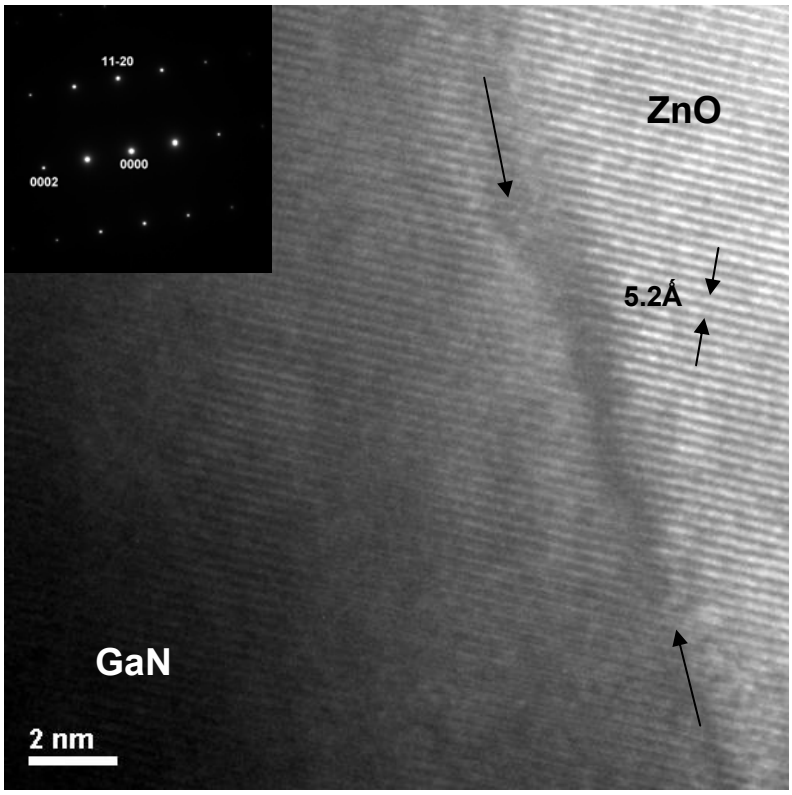

Fig. 5.5 HRTEM image and the corresponding SAED pattern of ZnO/ ELO GaN interface grown at 800ºC with the oxygen flow rate 10sccm.

ZnO/FACELO GaN interface. The lattice fringes of ZnO are perfectly aligned with those of the FACELO GaN and the interface is sharp on the atomic level. The selected area electron diffraction (SAED) pattern (inset in Fig. 5.5) indicates near lattice matching between ZnO and GaN hexagonal structures, which allow the

perfect epitaxial growth of ZnO on GaN resulting in high crystal quality.

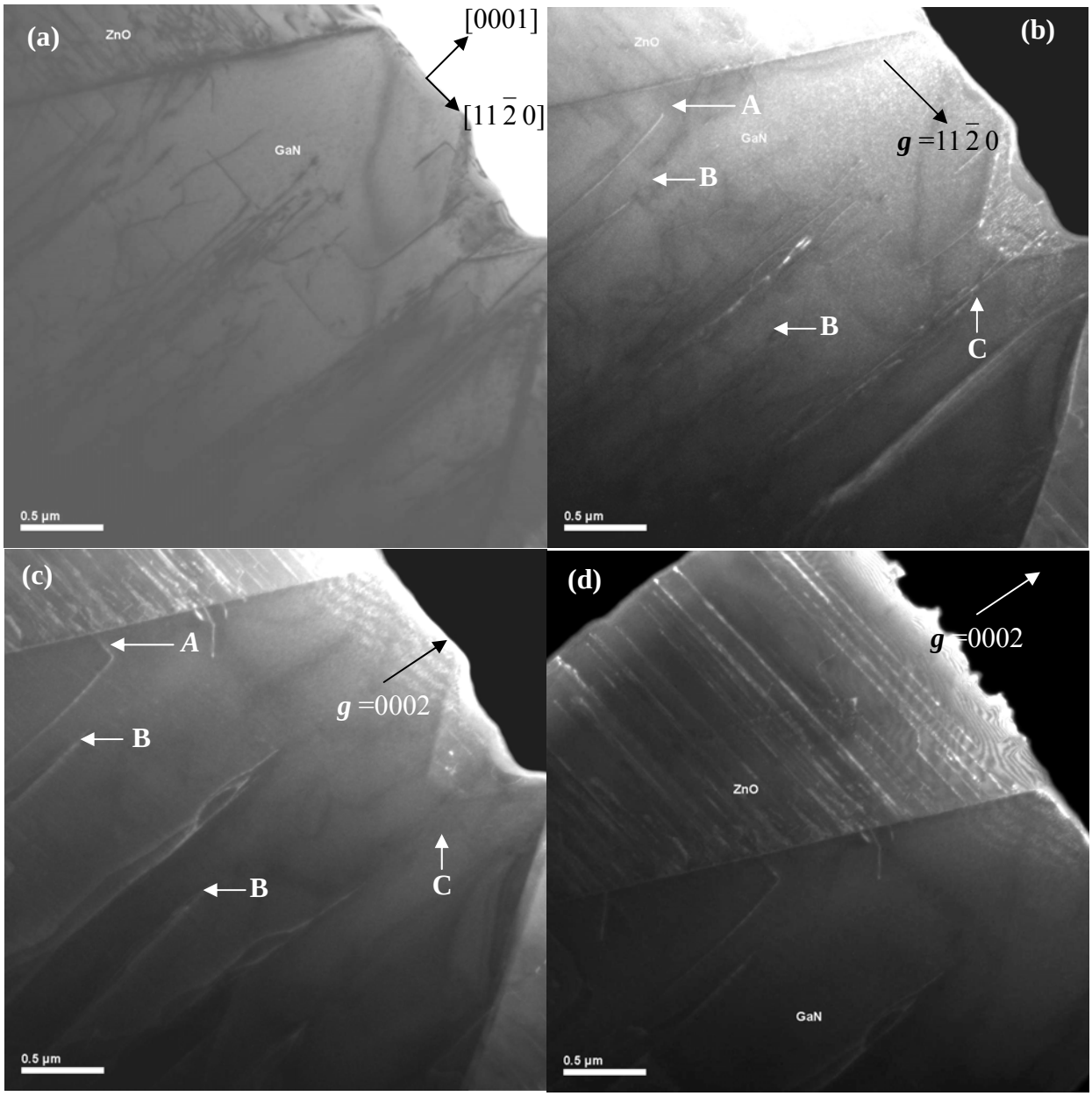

Fig. 5.6. Cross-sectional TEM (a) Bright-field image and (b) dark-field images with **g**=11$\bar{2}$0 and (c) **g**= 0002, (d) near the ZnO/ELO GaN, TDs shows two different bend directions.

A cross-sectional TEM image with lower magnification is presented in Fig.5.6. The ELO GaN dislocations have been studied by several groups [31-33] and the formation of the horizontal dislocations (HDs) is very important due to the fact

that HDs can dramatically decrease the threading dislocations (TDs) density in the regrown GaN regions.

Because ZnO is the wurtzite crystal structure, we investigated the Burgers vectors of the dislocations. In general, TDs with Burgers vectors **b**= [0001] (screw ***c*** -type dislocation), **b**=1/3 [11$\bar{2}$0] (edge ***a*** -type dislocation), and **b** =1/3[11$\bar{2}$3] (mixed ***a*** + ***c*** -type dislocation) were observed in wurtzite epitaxial GaN layers [34]. Then we also determined the Burgers vector of ZnO layers by a classical two beam analysis same as GaN. If one supposes that no, or at least few, partial dislocations are present in the GaN layer, a set of two beam images (**g**= 0002 and **g**= 11$\bar{2}$0) are sufficient to estimate the different types of Burgers vectors present in the layer (Fig. 5.6). For the **g**= 0002 condition, both screw- and mixed-type dislocations can be seen, whereas for the **g**= 11$\bar{2}$0 only the edge- and mixed-type dislocations are observed, based on the out of contrast extinction criterion **g·b**=0. Figure 5.6(a) is the bright-field image near the interface of the ZnO/ELO GaN with **g**= 11$\bar{2}$0. Figures 5.6(b) and 5.6(c) are the dark-field images at the same position as the bright-field image (Fig. 5.6a) with diffraction spots of [11$\bar{2}$0] and [0002], respectively. The dislocations bent toward the mask areas [11$\bar{2}$0] direction are visible in Fig. 5.6(c) (location A) but are not visible in Fig. 5.6(b). On the other hand, the dislocations with **b**= [0001] are also out of contrast in Fig. 5.6(b) (location B) but they are clearly visible in Fig. 5.6(c). Similar results were observed in MOVPE and HVPE-grown GaN by Sakai *et.al* group and Honda *et.al* groups [35, 36]. From this invisibility, we found that in the regrown ZnO layers the mixed dislocations ***a*** + ***c*** which split into pure edge dislocations as they bent toward the [11$\bar{2}$0] direction. In addition, dislocations with Burgers vector of ***a*** remain go parallel to c direction and stop at ELO GaN top surface (location C),

but no such kind of dislocation in the ZnO lateral overgrown areas was observed (Fig 5.6(d)). Half of the overgrown ZnO region is shown in Figure 5.6(d), which is also a dark-field image at [0002] diffraction spots. No vertical dislocations go through the ZnO overgrowth layers to the surface were observed in this large area. With these dislocations bending effect, the dislocation density of the ZnO layers will confirm decreasing and high crystal quality ZnO will achieved by this growth method. The mechanism of dislocation bending can be understood by considering the energy of dislocation lines emerging from a free surface of a crystal [27] [34]. From the point of view of dislocation line tension, any dislocation would tend to become perpendicular to a free surface to diminish its energy. As a result, dislocations would gradually change their line directions towards the normal direction of the current facet plane. There is also another explaination for the bending of the dislocations, when the GaN overgrowth on the oxide layer, the GaN/SiO_2 interface tension will lead to dislocation bending. [37] No vertical dislocation was produced from the ZnO/FACELO GaN interface. The high quality wing regions have been realized and it suggests that high quality ZnO films can be pesudomorphically grown on the ELO GaN. Using these growth conditions, high quality ZnO epilayers were fabricated on ELO GaN as shown in Fig. 5.1. Here, the HRTEM studies further confirm the suitability of ELO GaN layer for ZnO growth.

5.3 Optical properties and surface morphology

The optical properties of the ZnO layers on FACELO GaN were investigated by room temperature micro-PL spectroscopy. All these ZnO samples were grown with the same oxygen flow rate of 10sccm but at the growth temperature 780 ºC , 800 ºC and 820 ºC. For our PL system, the wavelength of He-Cd laser used is 325

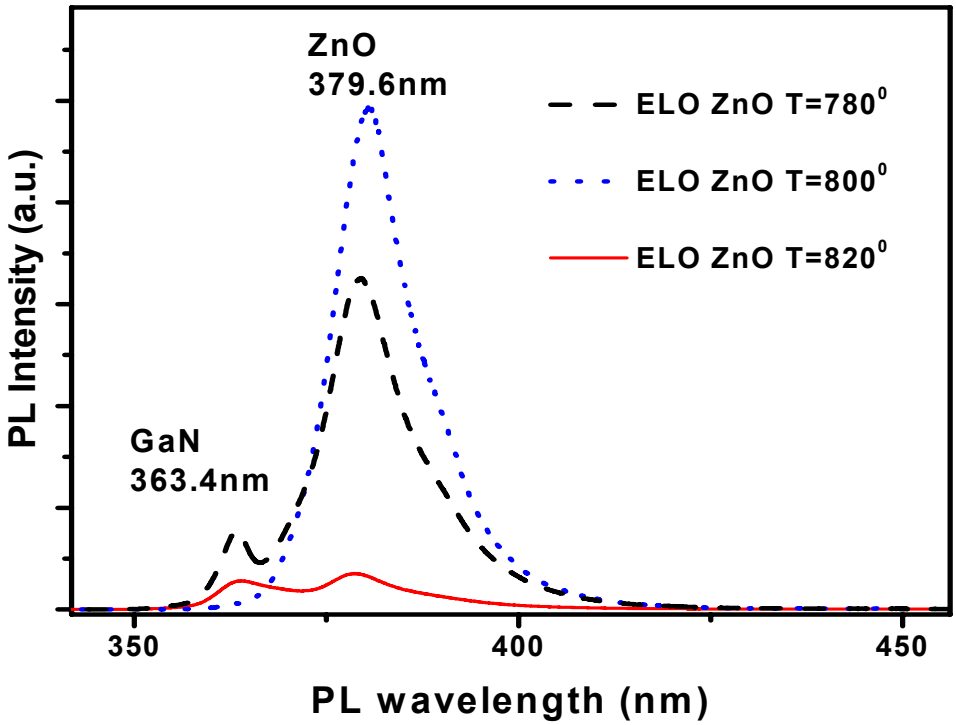

Fig. 5.7. The micro-PL spectra were taken from three different ZnO/ELO GaN samples grown at different temperature with the same oxygen flow rate of 10sccm, excitation by 325nm laser with a power of 1mW.

nm. The absorption coefficient α of ZnO films can be determined from transmittance measurements, [38] which is around 3.3×10^{-3} nm^{-1} at room temperature. This means that within the 300 nm ZnO layer the intensity of the PL excitation laser will be reduced by e^{-1}, so most of incident energy should be absorbed by ZnO. Obviously from Figure 5.7, the ratio of GaN peak intensity to that of ZnO is seen to vary with the growth temperature, indicating different thickness or/and crystal properties of ZnO layers.

In the PL spectra (Fig. 5.7), the peaks from GaN and ZnO can be seen at around 363 nm and 380 nm, respectively. From the spectra of 780ºC ZnO/GaN sample, the GaN/ZnO intensity ratio is larger than one suggesting the as grown ZnO is the nano rods, as observed from the SEM images (Fig.5.2). The strongest PL intensity

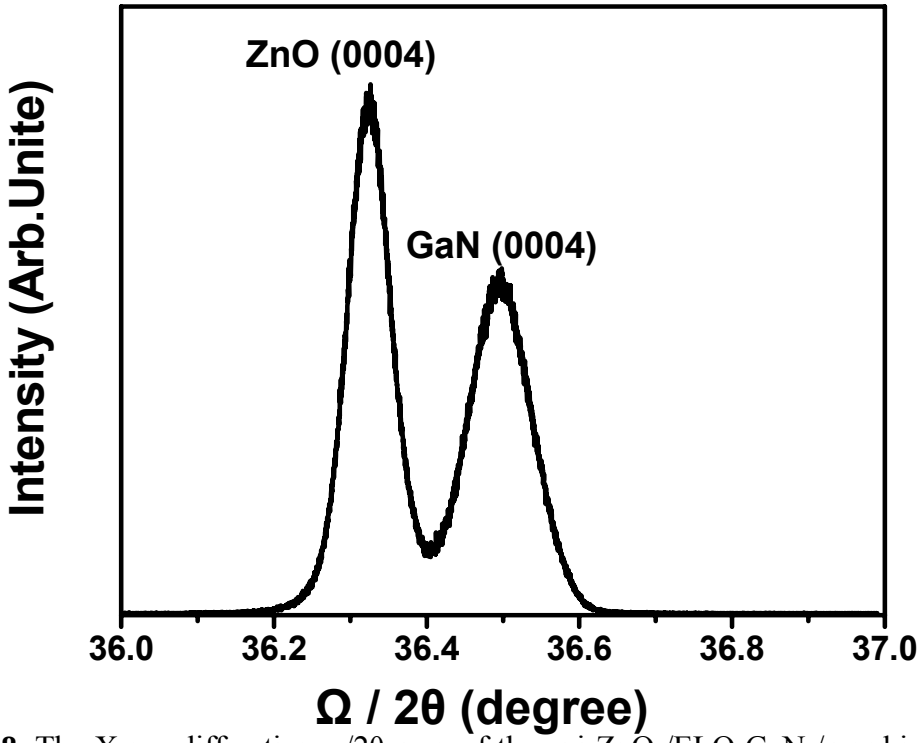

Fig. 5.8. The X-ray diffraction ω/2θ scan of the epi-ZnO /ELO GaN /sapphire (0001) heterostructure grown at 800ºC.

of the ZnO is observed from the 800ºC grown ZnO/FACELO GaN with the full width at half maximum (FWHM) of the PL ZnO peak of about 12 nm. This is the narrowest FWHM of three ZnO samples grown at different temperatures. This implies a higher epitaxial crystalline quality of ZnO films grown at 800ºC. The spectra of 820ºC ZnO/FACELO GaN shows a broder sprectra with FWHM of about 23 nm. The PL spectra show that the best ZnO quality is achieved at a grown temperature 800ºC with the oxygen flow rate of 10sccm.

The XRD ω/2θ scan profile of the ZnO film on the FACELO GaN /sapphire (0001) grown at 800ºC with the oxygen flow rate of 10sccm is shown in Figure 5.8. Only (000ℓ) family of planes of ZnO and GaN is observed, indicating that the ZnO/GaN heterostructure is strongly c-axis oriented normal to the sapphire (0001) plane. The XRD rocking curve full width at half maximum (FWHM) for the ZnO and GaN films was found to be 3 arcmin and 5 arcmin, respectively.

The surface morphology of the overgrowth ZnO sample grown at 800ºC with the oxygen flow rate of 10sccm was characterized by atomic force microscopy (AFM) and compared with a control sample grown on c-GaN under the same growth conditions In Fig. 5.9. The surface roughness (RMS) of the epi-ZnO on FACELO GaN and control sample are 0.40 nm and 3.67 nm, respectively. Atomic steps and terraces were clearly observed from the ELO ZnO sample. Only few step terminations in AFM observations can be detected, which indicates the high quality of the overgrown sample once more. The surface pit density of the overgrown GaN sample is reduced by more than 100 times, compared with the control sample. All these observations support that the ZnO growth method on $(11\bar{2}2)$ facets has an obvious beneficial effect on the dislocation behavior in the ZnO layer.

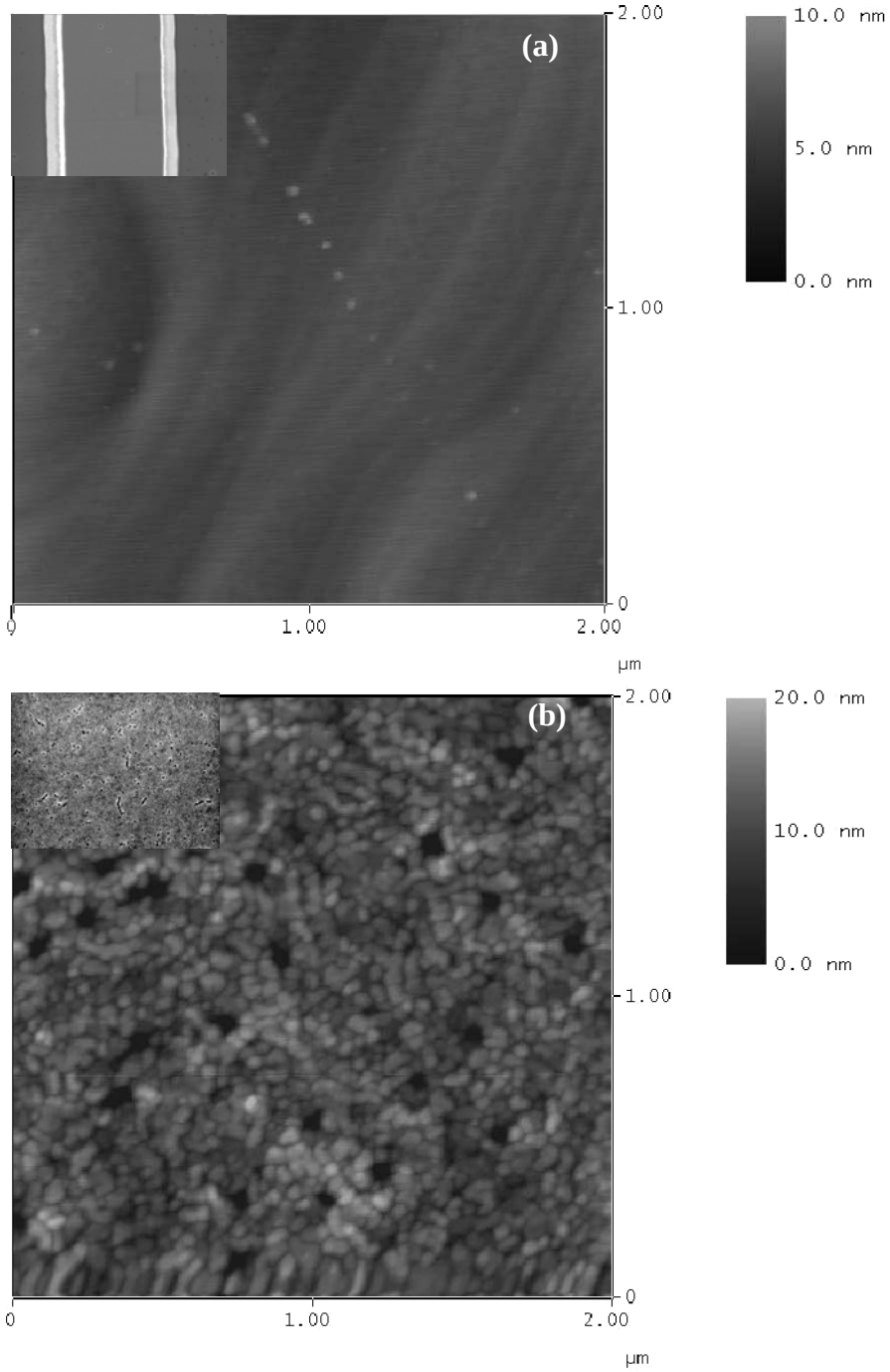

Fig. 5.9. (a) The surface morphology of the 800ºC ELO ZnO sample, which was characterized by atomic force microscopy (AFM) with (b) a control sample grown on c-GaN at the same growth conditions for comparison.

5.4 RBS characterization of ZnO growth on FACELO GaN templates

As shown in Figure 5.10, bands of high and low scattering intensity with a periodicity of 13 μm are found in the RBS channeling contrast microscopy (CCM) maps. In this technique a focused 2MeV H^+ beam is used to obtain laterally resolved channeling yield data. The bands correspond to different regions of the ZnO, and they are designated as band 1 (ZnO region) and band 2 (voids between the ZnO region) as shown in Figure 5.10. All data were collected in list-mode, therefore, it is possible to extract separate spectra from band 1 and band 2 (as defined in Fig. 5.10). Laterally resolved channeling data have been extracted from the RBS spectra in near-surface regions. Figure 5.11 shows random and channeled spectra of the band 1 part of the ZnO grown at 800ºC with the oxygen flow rate of 10sccm, for channeling and random alignment of the beam. The minimum ratio of the intensity of channeling spectra to random, χ_{min} of 5% is obtained for axial [0001] channeling of the ZnO grown at 800ºC. The full lines represent XRUMP [39] fits of the random spectra, they were generated by averaging the simulated RBS spectra of the structures, as deduced from the SEM data. Clearly, the lowest χ_{min} is obtained from the 800ºC growth samples. This indicates that the ZnO grown at

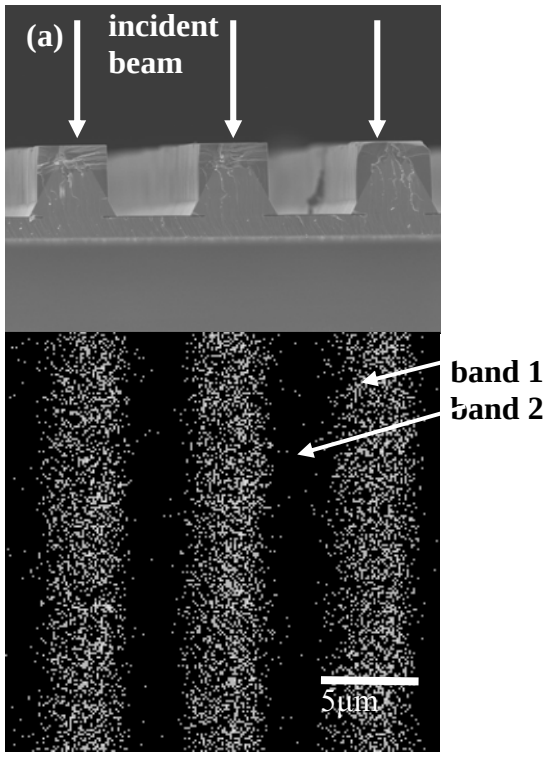

Fig. 5.10. Origin of the contrast pattern observed in the Channeling Contrast Microscopy maps

800ºC with an oxygen flow rate of 10 sccm has excellent crystal quality, much better than the sample grown at 820 ºC. Fig. 5.11 (d), (e) and (f) show random and channeled spectra of the band 2 part of the 780 ºC , 800 ºC and 820 ºC ZnO, the 2 μm GaN buffer layer is clearly seen with the random spectra.

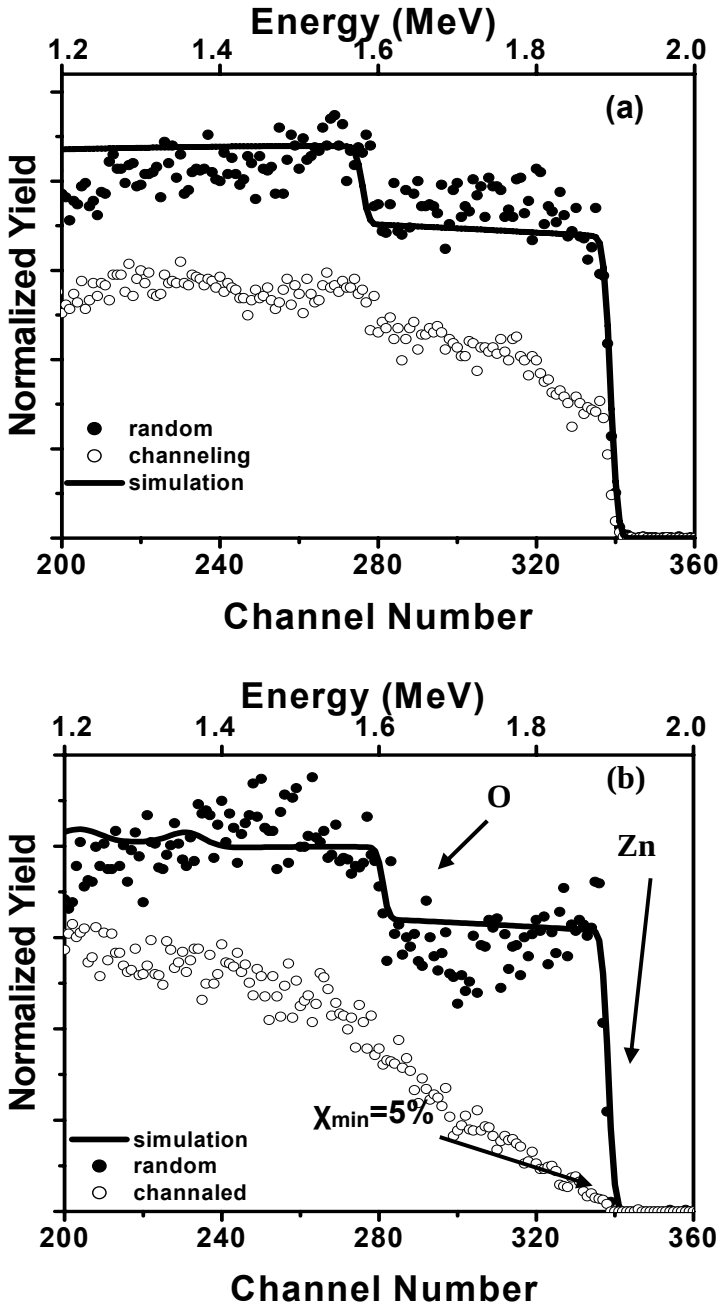

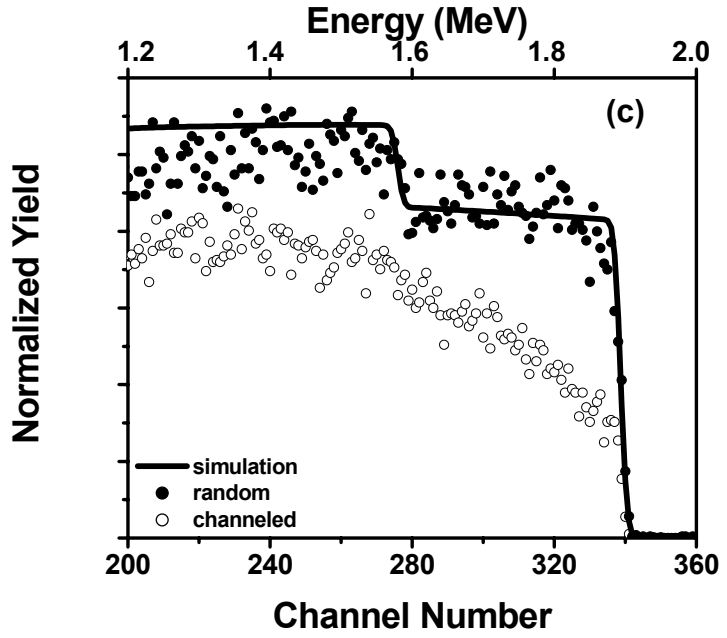
Energy (MeV)
1.2
1.4
1.6
1.8
2.0
(c)
Normalized Yield
simulation
random
channeled
200
240
280
320
360
Channel Number

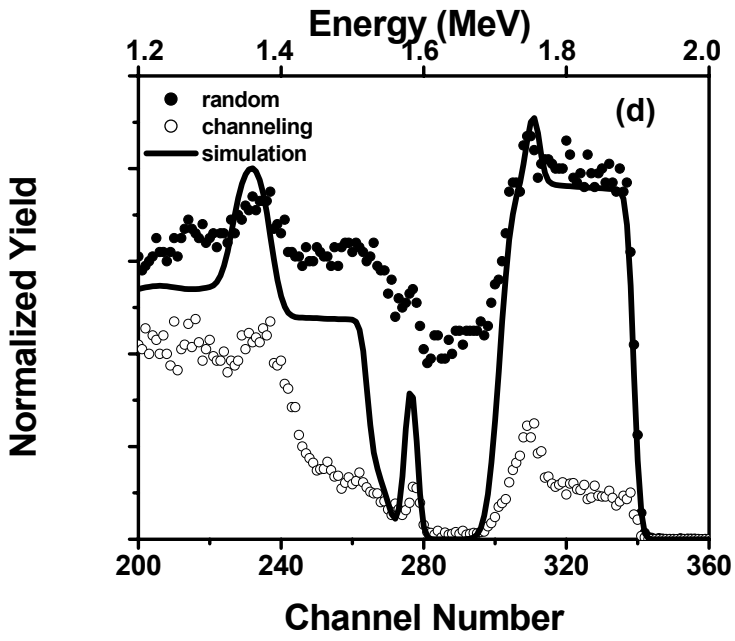
Energy (MeV)
1.2
1.4
1.6
1.8
2.0
random
channeling
simulation
(d)
Normalized Yield
200
240
280
320
360
Channel Number

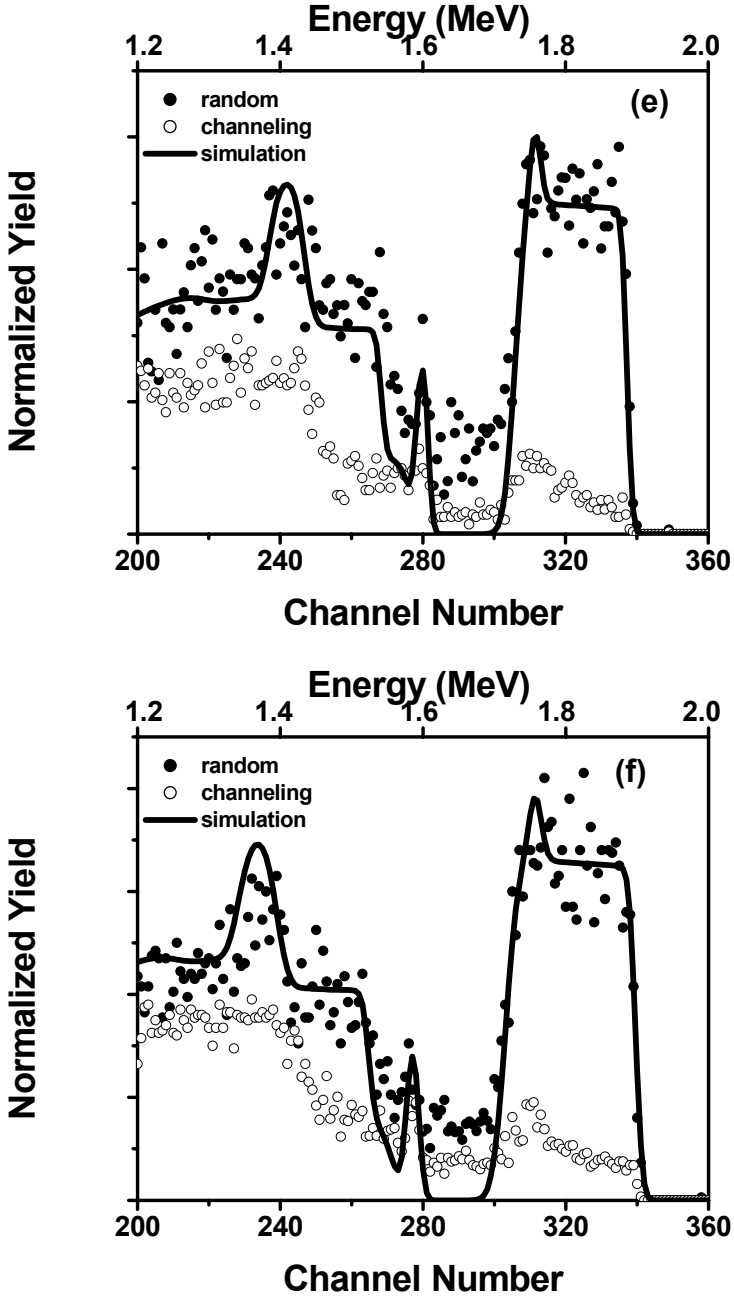

Fig. 5.11. (a), (b) and (c) are RBS spectra of band 1 region random and [0001] channeled ZnO/ ELO GaN grown at 780ºC, 800ºC and 820ºC, respectively, with the oxygen flow rate 10sccm;(d), (e) and (f) are RBS spectra of band 2 area random and [0001] channeled ZnO/ ELO GaN grown at 780ºC, 800ºC and 820ºC, respectively, with the oxygen flow rate 10sccm.

5.5 Chapter Summary

In a conclusion, high quality epitaxial ZnO/FACELO GaN heterostructures has been grown on sapphire substrates. These heterostructures showed a substantial improvement in the crystalline quality with a lower defect density and excellent photoluminescence emission. Different facet growth rates can be controlled by the variation of growth conditions, such as the temperature and oxygen flow rate. In addition, the lattice matching between the ZnO and GaN, thermal and optical properties, and the perfect interfaces of these ZnO/FACELO GaN heterostructures will provide new opportunities for the fabrication of hybrid ZnO/FACELO GaN optoelectronic devices on sapphire.

In next chapter, the conclusion of this thesis will be presented with suggestions for future work.

Reference:

[1] S. Cho, Y. Kim, Y. Sun, George K.L. "Photoluminescence and ultraviolet lasing of polycrystalline ZnO thin films prepared by the oxidation of the metallic Zn" Appl. Phys. Lett.**, 75**, 2761 (1999).

[2] M. H. Huang, S. Mao, H. Feick, H. Yan, Y. Wu, H. Kind, E. Weber, R. Russo, P. Yang, "Room-Temperature Ultraviolet Nanowire Nanolasers" Science.**, 292**, 1897 (2001).

[3] K. Minegishi, Y. Koiwai, Y. Kikuchi, K. Yano, S. Kasuga, A. Shimizu "Growth of p-type Zinc Oxide Films by Chemical Vapor Deposition" Jpn. J. Appl. Phys., **36**, L1453 (1997).

[4] S. J. Jiao, Z. Z. Zhang, Y. M. Lu, D. Z. Shen, B. Yao, J. Y. Zhang, B. H. Li, D. X. Zhao, X. W. Fan, and Z.K.Tang "ZnO p-n junction light-emitting diodes fabricated on sapphire substrates" Appl. Phys. Lett.**, 88** , 031911 (2006).

[5] C. R. Gorla, N. W. Emanetoglu, S. Liang, W. E. Mayo, Y. Lu, M. Wraback, H. Shen "Structural, optical, and surface acoustic wave properties of epitaxial ZnO films grown on (012) sapphire by metalorganic chemical vapor deposition" J. Appl. Phys.**, 85,** 2595 (1999).

[6] B. S. Li, Y. C. Liu, Z. Z. Zhi, "Growth of high quality ZnO thin films at low temperature on Si(100) substrates by plasma enhanced chemical vapor deposition" J. Vac. Sci. Technol. A, **217**, 131 (2002).

[7] P. M. Verghese, D. R. Clarke, "Surface textured zinc oxide films" J. Mater. Res., **14,** 1039 (1999).

[8] H. Saeki, H. Tabata, T. Kawai, "Magnetic and electric properties of vanadium doped ZnO films" Solid State Commun., **120**, 439 (2001).

[9] H. Z. Wu, K. M. He, D. J. Qiu, D. M. Huang, "Low-temperature epitaxy of ZnO films on Si(0 0 1) and silica by reactive e-beam evaporation" J. Crystal Growth, **217**, 131 (2000).

[10] T. Ohgaki, N. Ohashi, H. Kakemoto, "Growth condition dependence of morphology and electric properties of ZnO films on sapphire substrates prepared by molecular beam epitaxy" J. Appl. Phys., **93**, 1961 (2003).

[11] M. Chen, Z. L. Pei, C.Sun, "Surface characterization of transparent conductive oxide Al-doped ZnO films" J. Crystal Growth, **220,** 254 (2000).

[12] K.Tominaga, T.Murayama, I. Mori, "Effect of insertion of thin ZnO layer in transparent conductive ZnO:Al film" Thin Sloid Films, **386**, 267(2001).

[13] M. Kawasaki, A. Ohtomo, H. Koinuma, Y. Sakurai, Y. Yoshida, Z. K. Tang, P. Yu, G. K. L. Wang, and Y. Segawa, "Excitonic ultraviolet laser emission at room temperature from naturally made cavity in ZnO nanocrytal thin films" Mater. Sci. Forum, **264**, 1459 (1998).

[14] D. M. Bagnall, Y. F. Chen, Z. Zhu, T. Yao, S. Koyama, M. Y. Shen, and T. Goto, "Optically pumped lasing of ZnO at room temperature" Appl. Phys. Lett.**, 70,** 2230 (1997).

[15] V. Srikant, V. Sergo, and D. R. Clarke, "Epitaxial thin films of Al-doped ZnO were grown on sapphire substrates by pulsed laser ablation." J. Am. Ceram. Soc., **78,** 1931 (1995).

[16] R. D. Vispute, V. Talyansky, S. Choopun, R. P. Sharma, T. Venkatesan, M. He, X. Tang, J. B. Halpern, M. G. Spencer, Y, X. Li, L. G. Salamanca-Riba, A. A. Iliadis and K. A. Jones, "Heteroepitaxy of ZnO on GaN and its implications for fabrication of hybrid optoelectronic devices" Appl. Phys. Lett., **73,** 348 (1998); Y. I. Alivov, J. E. Van Nostrand, D. C. Look, M. V. Chukichev, and D. M. Ataev,

"Observation of 430 nm electroluminescence from ZnO/GaN heterojunction light-emitting diodes" Appl. Phys. Lett., **83,** 2943 (2003).

[17] D. J. Rogers, F. Hosseini Teherani, A. Yasan, K. Minder, P. Kung, and M. Razeghi, "Electroluminescence at 375 nm from a ZnO/GaN:Mg/*c*-Al_2O_3 heterojunction light emitting diode" Appl. Phys. Lett, **88,** 141918 (2006).

[18] H. Miyake, A. Motogaito, and K. Hiramatsu, "Effects of Reactor Pressure on Epitaxial Lateral Overgrowth of GaN via Low-Pressure Metalorganic Vapor Phase Epitaxy" Jpn. J. Appl. Phys., **38,** L1000 (1999).

[19] K. Hiramatsu, K. Nishiyama, M. Onishi, H. Mizutani, M. Narukawa, A. Motogaito, H. Miyake, Y. Iyechika, T. Maeda, "Fabrication and characterization of low defect density GaN using facet-controlled epitaxial lateral overgrowth (FACELO)" J. Cryst. Growth, **221**, 316 (2000).

[20] H, Miyake, M. Narukawa, K. Hiramatsu, H. Naoi, Y. Iyechika, T. Maeda, "Fabrication and Optical Characterization of Facet-Controlled ELO (FACELO) GaN by LP-MOVPE" Phys. Stat. Sol. (a), **188**, 725 (2001).

[21] D. Andeen, J. H. Kim, F. F. Lange, G. K. L. Goh, and S. Tripathy, "Lateral Epitaxial Overgrowth of ZnO in Water at 90°C " Adv. Funct. Mater., **16**, 799 (2006).

[22] K. Nishizuka, M. Funato, Y. Kawakami, S. Fujita, Y. Narukawa, and T. Mukai, "Efficient radiative recombination from <11 $\bar{2}$ 2>-oriented $In_xGa_{1-x}N$ multiple quantum wells fabricated by the regrowth technique" Appl. Phys. Lett.**,** **85,** 3122 (2004).

[23] S. Srinivasan, M. Stevens, F. A. Ponce and T. Mukai, "Polychromatic light emission from single InGaN quantum wells grown on pyramidal GaN facets" Appl. Phys. Lett., **87,** 131911 (2005).

[24] B. Neubert, P. Brückner, F. Habel, F. Scholz, T. Riemann, J. Christen, M. Beer and J. Zweck, "GaInN quantum wells grown on facets of selectively grown GaN stripes" Appl. Phys. Lett., **87,** 182111 (2005).

[25] S. Nakamura, M. Senoh, S. Nagahama, N. Iwasa, T. Yamada, T. Matsushita, H. Kiyoku,Y. Sugimoto, T. Kozaki, H. Umemoto, M. Sano, and K Chocho, "InGaN/GaN/AlGaN-based laser diodes with modulation-doped strained-layer superlattices grown on an epitaxially laterally overgrown GaN substrate" Appl. Phys. Lett., **72** 211-213 (1998).

[26] W. K. Burton,; N. Cabrera,; F. C. Frank, "Role of Dislocations in Crystal Growth" Nature, **163**, 398- 399 (1949). (b) W. K. Burton, N. Cabrera, F. C. Frank, "The growth of crystals and the equilibrilium structure oftheir surfaces" Philos. Trans. R. Soc. London, Ser. A, **243**, 299-358 (1951).

[27] G. W. Sears, "A growth mechanism for mercury whiskers" Acta Metall. 1955, **3**, 361-366. (b) G. W. Sears, "A mechanism of whisker growth" Acta Metall., **3**, 367-369 (1955).

[28] R.D. Zu, Zheng, W.; Wang, Z.L.; "Novel nanostructures of functional oxides synthesized by thermal evaporation." Adv. Funct. Mater.**, 13**, 9-24 (2003). (b) R. V. Coleman, G. W. Sears, "Growth of zinc whiskers" Acta Metall., **5**, 131-136 (1957). (c) C. Sinistri, "Transport numbers in pure salts" J. Chem. Phys., **37**, 1600-1605 (1962). (d) Ye, C.; Fang, X.; Hao, Y.; T, X.; Zhang, L.; "Zinc Oxide Nanostructures: Morphology Derivation and Evolution" J. Phys. Chem. B, **109**, 19758-19765 (2005)

[29] B. Lews, in *Crystal Growth* (Ed:B.R.Pamplin), Pergamon, Oxford 1980, pp.23-63.

[30] H. T. Ng, J. Li, M. K. Smith, P. Nguyen, A.Gassell, J. Han, M. Meyyappan,

"Growth of Epitaxial Nanowires at the Junctions of Nanowalls" Science, **300**, 1249-1249 (2003).

[31] T. S. Zheleva, O. H. Nam, M. D. Bremser, and R. F. Davis, "Dislocation density reduction via lateral epitaxy in selectively grown GaN structures" Appl. Phys.Lett., **71,** 2472 (1997).

[32] N. Kuwano, K. Horibuchi, K. Kagawa, S. Nishimoto and M. Sueyoshi, "Electron microscopy analyses of microstructures in ELO-GaN" J. Cryst. Growth, **237-239**, 1047 (2002).

[33] M. Ishida, M. Ogawa, K. Orita, O. Imafuji, M. Yuri, T. Sugino, K. Itoh, "Drastic reduction of threading dislocation in GaN regrown on grooved stripe structure" J. Cryst. Growth**, 221**, 345 (2000).

[34] S. Amelinck, in: F.R.N. Nabarro (Ed.), Dislocations in Solids, vol. 6, Elsevier, Amsterdam, (1982), pp. 67–460.

[35] A. Sakai, H. Sunakawa and A. Usui. "Transmission electron microscopy of defects in GaN films formed by epitaxial lateral overgrowth" Appl. Phys. Lett., **73**, 481 (1998).

[36] Y. Honda, Y. Iyechika, T. Maeda, H. Miyake and K. Hiramatsu. "Transmission Electron Microscopy Investigation of Dislocations in GaN Layer Grown by Facet-Controlled Epitaxial Lateral Overgrowth" Jpn. J. Appl. Phys. Part 2, **40,** L309 (2001).

[37] J. P. Hirth and J. Lothe, Theory of Dislocations, 2nd ed. Wiley, New York, 1982.

[38] C. GÜMÜ, O. M. Ozkendir, H. Kavak and Y. Ufuktepe. "Structural and optical properties of zinc oxide thin films prepared by spray pyrolysis method" Journal of Optoelectronics and Advanced Materials, 8, 299 (2006).

[39] Doolittle, L.R. Conference proceedings, Heavy Ions, MRS. (1990); E. J. Teo, T. Osipowicz, A. A. Bettiol, F. Watt, Hao MS and Chua S.J., "Channeling contrast microscopy on lateral epitaxial overgrown GaN" Nucl. Instrum. Meth. Phys. Res. B, **181**, 231 (2001).

Chapter 6

Conclusions and Future Work

6.1 Conclusion

In this study, various characterization techniques were used as tools in exploring the structural, optical and electronic properties of the AlGaN/GaN and InGaN/GaN quantum well structures grown on the FACELO GaN templates. The ZnO/GaN heterostructures grown on the FACELO GaN templates was also discussed.

Serial ELO GaN growth experiments provided the data to predict the complex growth velocity on different growth front orientation. The level-set equations, together with the surface velocity description, were also can be used to simulate the GaAs and InP materials systems. The excellent correspondence between simulations and experiments of the growth front instablity and the merging behavior of the microsize island epitaxial lateral growth not only shows the efficacy of the simulation procedure but also shows that the deduced velocity profile (V-plot) is essentially correct.

Successful growth of AlGaN/GaN MQWs was achieved on the $(11\bar{2}2)$ facets of FACELO GaN. Periodic MQWs structure was confirmed by HR-XRD, TEM and SIMS. TEM showed that the average growth rate on $(11\bar{2}2)$ facet is lower than on (0001) plane by a factor of 0.7 due to the smaller number of coordinated surface

atom bonds than that on the (0001) surface. SIMS showed that the concentration of Al is the higher on c-plane compared to the $(11\bar{2}2)$ surface. Micro Raman scattering revealed that there is a relaxation of compressive stress in FACELO GaN compared to the case of (0001) plane. CL spectra peak showed a blue shift on the $(11\bar{2}2)$ facet with respect to the c-plane. This is in agreement with quantum confinement of electrons. High optical quality of MQWs on the $(11\bar{2}2)$ facet is domnstrated by the comparable CL properties on both facets.

The structural and optical properties of InGaN/GaN MQWs structures grown on FACELO GaN templates have been studied. Successful growth of InGaN MQWs was achieved on the $(11\,\bar{2}\,2)$ and (0001) facets grown on the FACELO GaN/Sapphire templates. Periodic InGaN MQWs structures were confirmed by TEM and HR-XRD. TEM showed that the average growth rate on the $(11\bar{2}2)$ facet is lower than on the (0001) plane by a factor of 0.25. Low temperature CL spectra showed that our InGaN MQWs structures provide wide range wavelength output light, which is suitable for the white color luminescence display devices. These properties make us believe that our proposed structure is promising for light-emitting devices that require sophisticated syntheses of colors such as pastels and white.

High quality epitaxial ZnO/ELO GaN heterostructures has been grown on sapphire substrates. These heterostructures showed a substantial improvement in the crystalline quality with a lower defect density and excellent photoluminescence emission. Different facet growth rates were controlled by the variation of growth conditions, such as the temperature and oxygen flow rate. The perfect interfaces of these ELO ZnO/GaN heterostructures provide new opportunities for the fabrication of hybrid ZnO/GaN optoelectronic devices on

sapphire.

6.2 Future work

The work of this thesis is quite a new area and there also need more effort for the further development, including film growth, interface characterization, and theoretical calculations.

1. The approach described above, using experimental input to deduce a V-plot, makes numerical simulation of complex growth geometries possible, such as for the case of patterned ELO growth of GaN or in other systems (e.g. the interesting ELO of GaAs or InP). Such simulations will be an important quantitative tool to design complex ELO structures for novel optoelectronic applications requiring pointed or ridged features, the presence of particular surface orientations or in optimizing novel growth strategies.

2. There are still challenges in the application for the LEDs device based on the FACELO GaN templates, e.g. quantifying the growth rates for different crystallographic facets, in-dept analysis of mass transfer on each facet, indium composition distribution on various surface, p-type doping and metal contact.

3. For the case of ZnO light emitters based on quantum confinement effect, a big challenge is the difficulty of p-type doping in ZnO which has impeded the fabrication of ZnO homojunction devices. The doping efficiency of the $(11\bar{2}2)$ facets may not as same as the (0001) surface due to the higher coordination. Therefore, further studies to explore the role of incorporation of magnesium in the ZnO grown on the FACELO GaN would also be an interesting topic.